Bluetooth Direction Finding

Lichen Yao

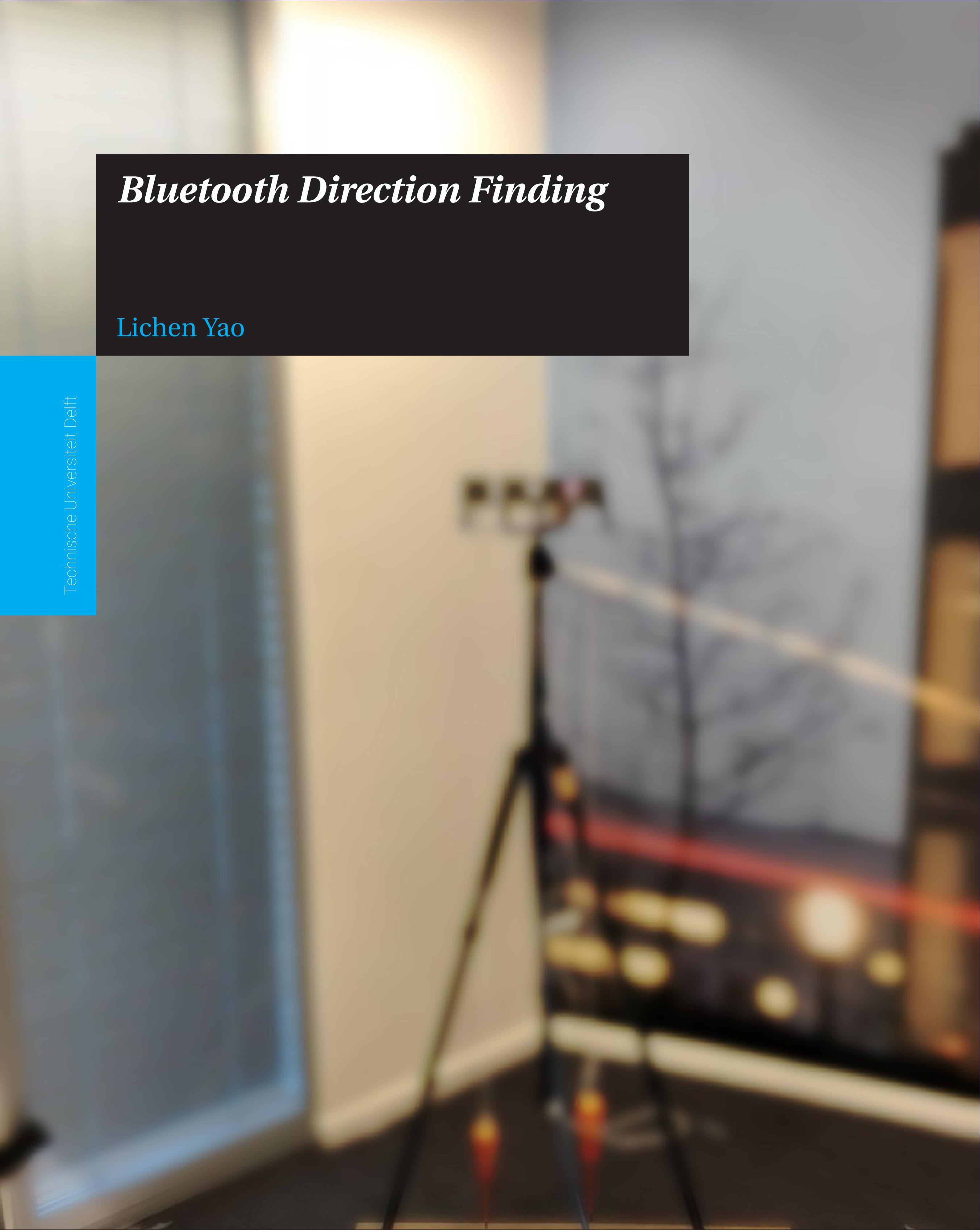

Delft University of Technology

Challenge the future

Bluetooth Direction Finding

by

Lichen Yao

to obtain the degree of Master of Science
at the Delft University of Technology,
to be defended publicly on Thursday September 13, 2018 at 10:00 AM.

Student number:	4607406	
Project duration:	January 7, 2018 – September 13, 2018	
Thesis committee:	Prof. dr. ir. A.J. van der Veen,	TU Delft, supervisor
	Dr. ir. G. Janssen,	TU Delft
	Prof. dr. ir. G. Dolmans,	IMEC-Holst Center/TUe, supervisor
	Dr. ir. J. Romme,	IMEC-Holst Center/TU Delft, supervisor

This thesis is confidential and cannot be made public until September 13, 2020.

Abstract

Indoor positioning using Bluetooth is attractive because of the broad range adoption of Bluetooth on mobile phones, laptops, and portable wireless-enabled devices. The low cost, low power consumption, and small size of Bluetooth devices enable embedded solutions for precise location and proximity-based applications such as indoor navigation, smart city, smart building and Internet of things. In the next generation of Bluetooth standard, the Bluetooth SIG wants to incorporate multiple antenna systems into the Bluetooth Low Energy specification to enable direction-finding features. The features are aimed to improve the accuracy of off-the-shelf Asset Tracking Profile (ATP) and Indoor Positioning Service (IPS) including two modes - Angle-of-Arrival (AoA) mode and Angle-of-Departure (AoD) mode. In this thesis, we only focus on the AoA mode.

The new standard raises several challenges. First, the direction finding algorithm shall be derived since the standard gives only the framework. The algorithm shall cope with dense multipath effects in indoor environments and identify the angle of Line-of-Sight (LOS) component. Second, the new standard specifies the usage of an RF switch such that a single receiver can access multiple antennas. This mechanism reduces the device cost and complexity but poses difficulties to the array processing. There are inevitably information loss during antenna switching. It also raises requirements of channel stationarity and efficient compensation of CFO. Third, towards the system implementation, practical considerations that deviate the ideal data model shall be taken into account. These considerations include the effect of mutual coupling (MC), and the phase imbalance of the RF switch. During this project, these effects have been studied to obtain insight on the influence on algorithm performance and compensation techniques.

In this thesis, we formulated the data model for a single receiver using a uniform linear multiple antenna system with an RF switch. The importance of CFO compensation, channel stationarity, and the color of noise are addressed. A maximum likelihood (ML) based CFO estimation algorithm is proposed. Furthermore, we modeled the effect of mutual coupling and imbalance of switch. Next, we analyzed why the delay estimation is not feasible within the context of Bluetooth LE. We proposed two Line-of-Sight direction identification (LOS-Id) algorithms based on the power signature in the data covariance matrix, which are referred to as MUSIC LOS-Id and CLEAN-MUSIC LOS-Id. Further performance improvements are achieved by making use of the frequency hopping feature of Bluetooth. By aggregating more than one packets at different frequencies, the performance can be improved substantially. This technique is called the multi-tone technique, or packet aggregation (PA).

For evaluating the effectiveness of the proposed methods and models, a Bluetooth LE simulator is built. The performance verification is divided into two phases that differentiate themselves by the channel model. In the first phase, a simulated channel model, which is obtained by applying the ray tracer in an empty rectangular room, is used. The mutual coupling effect is simulated using the Antenna Toolbox in Matlab. The switch characteristics are verified by measurements using a Vector Network Analyzer (VNA). In the second phase, the real channel is measured with the VNA. Three campaigns of measurements are carried out with a 1×4, 1×8, and 2×4 antenna array respectively. Performance is evaluated by applying both channel models.

The simulations reveal that the multipath effect is the dominant influencing factor of the performance in our indoor scenario, while the mutual coupling and the switch imbalance have little influence. The results also show that both proposed LOS-Id algorithms yield satisfying accuracy. However, we paid less attention to the CLEAN-MUSIC algorithm because of its complexity even though it indeed performs better than MUSIC LOS-Id in our simulated scenario. Finally, the usage of multi-tone technique improves the LOS-Id performance substantially. With an 8-element ULA and aggregating 8 tones, the MUSIC LOS-Id algorithm can achieve 10° of RMSE for 90% of transmission positions with measured channels, and 3° of RMSE for 50% of transmission positions.

Acknowledgements

I hereby want to express my gratitude with honor to people who guided and encouraged me during the period of the thesis work.

First, I would like to give my thanks to my supervisor Prof. Alle-Jan van der Veen. He supported me all the way from the beginning and was responsive whenever I need. His in-depth mind and sagacious talks are always inspiring.

Next, I would like to thank my daily supervisor Dr. Jac Romme. Jac's profound knowledge, professional attitude and patient guidance tided me through both technical and mental difficulties. I would also like to thank Prof. Guido Dolmans. It's him who gave me the opportunity to this wonderful journey in IMEC-Holst Center. I also want to give special thanks to my colleagues Rainer, Hannu, and Johan in IMEC. Their professional skills and supports made my work so much easier.

Finally, thanks to the accompany from my parents and my friends, I enjoyed great time studying in TU Delft. Their presence left me tons of joyful memories that can still be thought back cheerfully in the rest of my life.

Lichen Yao
Delft, September 2018

Contents

1

Introduction

Indoor positioning service (IPS) has been a complement to Global Navigation Satellite Systems (GNSS) such as Global Positioning System (GPS) and cellular-based localization technologies [8][48]. It provides coverage and increased accuracy in indoor areas where GNSS and cellular systems may experience pitfalls due to penetration attenuation and multipath loss.

Over the last decades, the researches for indoor positioning techniques have drawn massive interest. The explosive growth of mobile phones and portable wireless communication enabled devices gave birth to wide-range of location-based applications such as navigation, smart city, smart building and Internet-of-Things (IoT). As a result, wireless technologies such as WLAN, RFID, Ultra Wide Band (UWB), Bluetooth and Zigbee are innovated and adapted to offer localization service as accurately and energy-efficiently as possible.

Among these technologies, Bluetooth is a popular carrier of IPS because of its broad adoption on modern wireless devices, low cost, low power, and small size [48]. Particularly, Bluetooth Low Energy (BLE) [4] has been a significant Physical Layer (PHY) that pushes Bluetooth to be the critical enabler in the era of IoT. Among 48 billion devices that will be connected to the Internet, as anticipated by ABI research, 30 percent of those will carry Bluetooth technology [46].

1.1. Motivation

In 2015, the Direction Finding Work Group (DFWG) of Bluetooth Special Interest Group (SIG) announced the support of localization service on Bluetooth in their Indoor Positioning Service (IPS) document [6]. It defined the behaviors and data that a localization enabled Bluetooth device has to comply with and support, such as the global longitude and latitude coordinate, local north and east definition, floor number and altitude of the beacons, etc. It is necessarily an architecture and foundation which localization applications can make use of.

Recently, the Bluetooth SIG initiated the drafting of the next generation Bluetooth specification known as Madrid version. In this specification and the next version of IPS, Direction Finding (DF) feature based on PHY of BLE will be added to the indoor positioning portfolio. In Madrid version, BLE devices may equip antenna arrays in combination with RF Switches to reduce receiver complexity. The DF feature can be accomplished together with a new link layer packet field Constant Tone Extension (CTE), a new antenna switching mechanism, new IQ sampling procedures, and local antenna array geometry and response information.

As the draft approaching publication, a few problems have to be resolved to implement the new standard on future BLE devices. The first one is looking for the direction finding algorithm in the indoor multipath environment based on the antenna switching mechanism. The standard provides simple example algorithms, but to achieve the accuracy for localization, efficient and high-resolution algorithms have to be found. Besides, the antenna switching mechanism makes the Bluetooth direction finding unique to the usual antenna array processing which accesses the antennas simultaneously. Thus we need to formulate the usual array processing problem to adapt the new antenna switching feature.

Moreover, among all components, only the Line-of-Sight (LOS) component tells the bearing of the transmitting device. Thus we also need to distinguish the LOS component out of the others. The third problem is hardware imperfection. Super-resolution DF algorithms like MUSIC are sensitive to array mis-modeling, which mostly comes from hardware imperfection. Imbalanced cables and switches that connect antennas to the receiver introduce unwanted phase shift on the received signals. Mutual coupling (MC) is another physical phenomenon that causes phase distortion. Studies need to be done to model these phenomena and find out their effects on the DF performance. If necessary, we shall aso compensate them.

This project focuses only on direction finding feature. As for how to make use of the angular information to derive device position, it is out of the scope of this thesis.

1.2. Research Objectives

This thesis project focuses on exploring possibilities about how to implement Direction Finding feature that will be incorporated into the next generation of Bluetooth standard. The objectives of the project are to:

- Explore the relevant chapters in the standard and spot limitations and advantages to indoor direction finding.
- Develop a super-resolution algorithm based on MUSIC, to be able to compensate for performance degradation due to multipath effect and recognize LOS direction.
- Find appropriate techniques for modeling the antenna array mis-model factors and research their effects on direction finding.
- Find out the performance of the algorithm in simulation using a ray tracer channel model.
- Carry out experiments to characterize a realistic indoor channel, which is used for evaluation of the algorithm.

1.3. Structure

The structure of this thesis is introduced as follows: Chapter 2 will give an introduction to the DF related contexts in the next generation Bluetooth specification. In this chapter, there will also be an analysis of the practical limitations and advantages that are introduced by the specification.

Chapter 3 introduces the general antenna array data model for a direction finding systems. The formulation of the data model with the antenna switching mechanism is done. Moreover, array model modifications are proposed by taking into account the practical consideration including mutual coupling, switch leakage, and imbalance.

Chapter 4 is about direction finding techniques. The super-resolution algorithm MUSIC is introduced first as a basis of our proposed method. Then, the modeling techniques of MC and switch are analyzed. Ultimately, two algorithms are proposed to identify the AoA of the LOS component.

Chapter 5 and 6 are algorithm performance evaluations. Chapter 5 evaluate the proposed algorithms by constructing a BLE simulator first. The channel model is simulated with Matlab according to the ray tracer model. Chapter 6 contained details of the measurement when the realistic channel data was collected. Three different array geometries are used, to verify which one is the most efficient and practically feasible. Similar evaluations are done as in chapter 5.

The final Chapter 7 is the conclusion of the thesis. Besides, we also proposed future works such that the work in the thesis can be refined.

2

Bluetooth LE Features

Madrid version specifies changes to incorporate direction-finding features on BLE devices. It allows a device to equip more than one antenna with the combination of an RF switch. The devices can enable the direction finding features by transmitting special link layer packets. Depending on the use case, BLE systems can operate in either Angle-of-Arrival (AoA) or Angle-of-Departure (AoD) mode.

2.1. Bluetooth Low Energy

Bluetooth Low Energy (BLE) is a wireless personal area network technology designed and promoted by Bluetooth Special Interest Group (Bluetooth SIG). Compared to classic Bluetooth - Basic Rate (BR) and Enhanced Data Rate (EDR), BLE maintains considerable data rate and similar communication range while providing reduced power consumption and cost.

The BLE system operates in the 2.4 GHz ISM band at 2.4-2.4835 GHz, which is the same as classic Bluetooth. Unlike classic Bluetooth's 79 1-Mhz wide channels, BLE uses 40 channels with center frequencies $2402 + k \times 2MHz$ (for $k = 0, ..., 39$) which are separated by 2 MHz. In each channel, data are modulated by Gaussian Frequency Shift Keying (GFSK). The output power of a BLE device is limited within the range between -20 dBm and +20 dBm (the maximum output power in Bluetooth 4.0 is +10 dBm).

Three physical layers (PHY) are supported in BLE systems whose names reflect differences of modulation, coding that may be applied and resulting data rate. Two uncoded physical layers are distinguished by the supported bit rate of 1 Mb/s and 2 Mb/s respectively, namely LE 1M/2M PHY. Only LE 1M PHY is mandatory. LE Coded PHY supports 1 MB/s symbol rate only. While supporting coding schemes with different amount of redundancy, providing the bit rate of 500 kb/s and 125 kb/s.

A BLE radio employs adaptive frequency hopping to create robustness against narrowband frequency selective fading and interference. BLE radios hop to a different channel (frequency) every 625 microseconds (1600 hops/s), which is longer than a link layer packet. Thus it is sometimes termed as slow hopping.

The discovery and pairing procedure of BLE devices are based on advertisement broadcasting. The advertising device sends an advertising packet on at least one of three advertising PHY channels in dedicated time intervals called advertising events. Any receiver can initiate a connection request if the advertising packet is connectable.

A summary and details about the BLE PHY are listed in table 2.1.

2.2. Direction Finding Modes

Localization using wireless signals are typically accomplished by using many beacons that are located in predefined fixed locations. The devices whose locations are of interest are referred to as mobile sites in this thesis. Madrid version specifies that a BLE compatible device may equip an antenna array that consists of two or more antennas, which can be used to extract phase difference out of IQ samples of received signals. Antennas are controlled by an RF switch, which accesses antennas sequentially. Then the bearings of received signals can be derived using the phase difference information. Devices that are equipped with antenna arrays are typically used as beacons, because of the bigger antenna aperture.

Characteristic	**Specification**	**Details**
Frequency Band	2.4 GHz ISM	2400 to 2483.5 MHz
Modulation	• GFSK at 1 Msymbol/s • BT = 0.5 • Modulation index: 0.45 to 0.55 (0.5 nominal)	Minimum frequency deviation shall never be smaller than 115 kHz(BR/EDR) and 185 kHz(LE)
Frequency Hopping	Standard hop rate: 1600 hops/s	Hopping rate depends on the device mode. For instance, the hopping rate is 3200 hops/s in PAGE mode, where the paging message is a very short packet.
PHY	• LE 1M PHY – Mandatory – Symbol rate 1 Msymbol/s, bit rate 1 Mb/s • LE Coded PHY – Optional – Support error correction coding on 1 Msymbol/s – Coding schemes: S = 2/8 (S symbols represent 1 bit, such that bit rate 500 kb/s or 125 kb/s) • LE 2M PHY – Optional – Symbol rate 2 Msymbol/s, bit rate 1 Mb/s – Support *uncoded data* only	• LE 1M and LE 2M are collectively referred to as LE Uncoded PHY • Direction Finding is *only supported over LE Uncoded PHYs.*
Output Power	0.01 mW(-20 dBm) to 100 mW(+20 dBm)	

Table 2.1: Bluetooth Low Energy radio characteristics

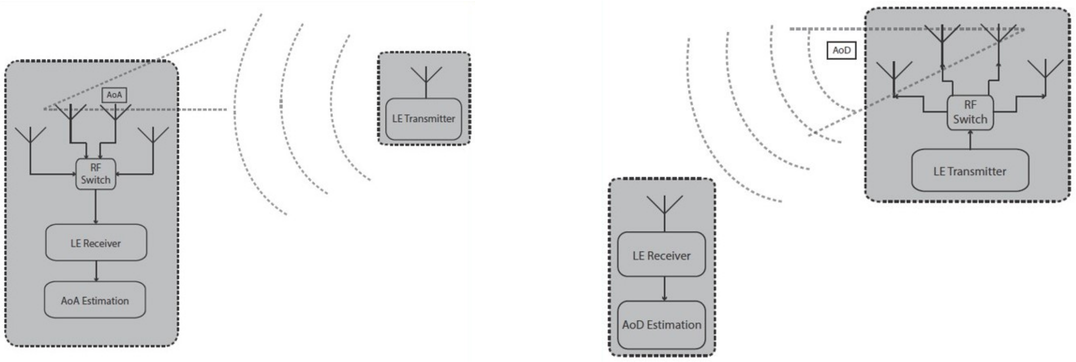

(a) Connection-Oriented AoA Mode

(b) Connectionless AoD Mode

Figure 2.1: BLE Direction Finding Modes

Direction finding in Bluetooth Indoor Positioning portfolio is classified into two modes depending on the application scenario. The first one is the Angle-of-Arrival (AoA) mode, where the beacons try to calculate the bearing of the received signal to track the mobile device. In this mode, the mobile device transmits special link layer packets while the beacon receives them. When receiving, the device carries out antenna switching at a pre-defined pattern.

The second direction finding mode is the Angle-of-Departure (AoD) mode. In contrast to the AoA mode, the beacon performs as the transmitter, while the switching operation is also carried out at a similar pattern as the AoA mode, such that a phase difference information can also be created even though the receiver has only a single antenna. In this mode, the mobile device tries to obtain its relative angular position with respect to the beacon, whose location and antenna orientation can be known to the mobile device through profile-level communication procedures.

In fact, AoA and AoD mode are similar to each other despite some minor differences. They are both based on the phase difference information that is created by multiple spatially separated antennas. They both apply the antenna switching mechanism to access antennas. Thus, the direction finding algorithm can be shared among two modes without significant modification. There are also notable differences. The role of beacons with multiple antennas are different. In AoA mode, the beacon operates as the receiver, while in AoD mode, the beacon operates as the transmitter. Another difference comes to time synchronization. In the AoA mode, the antenna switching and receiving happens within the same device, such that there is no sampling/switching time ambiguity. While in AoD mode, the switching in beacon and sampling in the mobile device may not be perfectly synchronized, which potentially corrupts sample values. In this thesis, we focus on the AoA mode.

2.3. Link Layer Supplement

2.3.1. Link Layer Packet Format for LE Uncoded PHYs

Madrid version specifies a Link Layer supplemental packet structure as a part of incorporating AoA/AoD features. The DF feature is only supported on LE Uncoded PHYs, so we start by introducing the Link Layer packet format for LE Uncoded PHYs.

LE Uncoded PHYs use the same packet structure on all physical channels. The format is shown in figure 2.2. Every packet starts from a preamble of 1 or 2 octets, corresponding to LE 1M PHY or LE 2M PHY respectively. The preamble is followed by the Access Address, Protocol Data Unit (PDU), CRC and an optional Constant Tone Extension (CTE). The entire packet is transmitted at the same symbol rate and takes between 44 and 2120 μs to transmit. The duration of Constant Tone Extension ranges from 16 to 160 μs, when Constant Tone Extension is present.

A Link Layer packet always contains a preamble which is composed of alternating 1s and 0s as the beginning of the packet. It is used for frequency synchronization, symbol time estimation, and automatic gain control (AGC) control in the receiver. The first bit of a preamble shall be the same as the first bit of Access Address.

Access Address is also a mandatory field for all LE packets. It is used to differentiate communication types

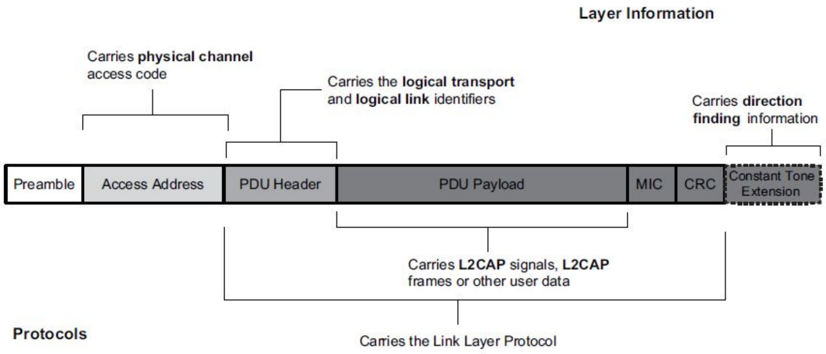

Figure 2.2: Link Layer packet format for LE Uncoded PHYs [3]

on physical channels. Access Address specifies whether the packet is sent on a physical advertising channel that is used for non-periodic advertising, a periodic physical channel that is used for periodic advertising, or to a piconet physical channel (supports an LE active physical link, that is a point-to-point link between the master and slave when they are in connection). The LE advertising physical channel uses a fixed Access Address. The LE periodic physical channel and LE piconet physical channels use a randomly generated 32-bit sequence as their Access Address.

A Link Layer packet always has a PDU header containing the type of advertisement broadcast or logical link carried on the current physical channel. For Data Channel PDUs, the PDU header contains a CTEInfo Present (CP) field, and an optional CTEInfo field, specifying the information of the CTE that is carried in this packet. A Message Integrity Check (MIC) is optional. A 24-bit Cyclic Redundancy Check (CRC) follows PDU. CRC shall be calculated over the PDU. The calculations of MIC and CRC do not include CTE.

2.3.2. Constant Tone Extension

Constant Tone Extension is an optional field in a Link Layer packet. CTE can be carried by both advertising channel and data channel packets. BLE uses this field to determine the relative bearing of peer devices.

CTE contains constant and un-whitened 1s, which means it is a single tone sine wave with a positive frequency deviation. It has a variable duration ranging from 16 to 160 μs. The first 4 μs is the Guard Period, which is used to avoid Inter-Symbol Interference (ISI) with the previous field. The next 8 μs is termed as the Reference Period. The rest of a CTE is split into two types of alternating time slots of the same length. The duration of the time slots can either be 1 μs or 2 μs as specified by the Host device. These time slots are termed as switch slot and sample slot (or Tx slot in AoD mode). The 2 μs slot is mandatory to support, while the other is optional. The format of a CTE is shown in figure 2.3.

2.3.3. Antenna Switching

BLE employs a switch-then-sample mechanism to access antenna array. Instead of sampling antenna elements at the same time, this mechanism reduces the required number of receivers to one. In each switch slot, the antenna switching is performed, while in the next sample slot the receiver takes only one IQ sample.

The Constant Tone Extension can be of two types: AoA and AoD. In AoA mode, the single-antenna mobile device continuously transmits CTE. On the receiver, the antennas are sequentially switched on in switch slots. The sequence of switching can be user-defined. Examples can be Round Robin ([1,2,...M,1,2...]), Return to First ([1,2,1,3,...1,M]), or Mirror ([1,2,...,M,M-1,...2,1]). Each switch slot is followed by a sample slot, where one IQ sample is taken. In AoD mode, the transmitter becomes the beacons. In this case, sample slot becomes Tx slot, within which the beacons transmit CTE continuously. The mobile receiver samples the received signal during sample slots.

Despite the advantage of reduced device complexity, this sequential sampling mechanism discards part of spatial and temporal information since at a time only one antenna is activated. Numerous studies were done to try to recover this portion of lost information.

Sub-array sequential sampling over an array whose number of elements is larger than the receiver is studied successively by Sheinvald and Wax in [36], Fishler and Messer in [9], Tabrikan and Faizakov in [39]. The whole array is recovered from the sub-arrays using a time-varying pre-processing transformation matrix. Maximum likelihood (ML) estimator is approximated based on the sequential sampling model in these pieces of literature. An approximation spectrum of super-resolution algorithm MUSIC is also derived with less receivers than antennas in [47]. Studies based on specific types of signals in automotive radar applications are also interested in using a reduced number of receivers, see, for instance, [23].

Within the context of BLE direction finding, though, we have a bit of head start. We can avoid using preprocessing techniques introduced in the last paragraph because of the unique structure of CTE. Because the CTE is constant, after demodulation in the receiver side, the baseband complex envelope from an antenna is constant both in amplitude and phase. Thus even though we discard information of other antennas at a sampling time instance, the information can be recovered if we look at the signals sometime later that sampling time as long as the noise is temporally white and the channel is stationary during the antenna subsequent switching period. More detailed analysis can be found in the section 3.3.

2.3.4. IQ Sampling

The receiver takes IQ samples when receiving a valid packet that contains a CTE field, and may also perform sampling even though the packet contains an incorrect CRC.

In either direction finding mode, the receiver samples per 1 μs during the reference period. Thus, a total number of samples that are available in a CTE field is 9 to 45 with 2 μs (8 reference samples, 1 to 37 samples in sample slots), and 10 to 82 with 1 μs (2 to 74 samples in sample slots). To ensure a decent quality of samples, the sampling has to take place outside two small guard periods. The guard periods are first and last 0.125 μs of a 1 μs sample slot. As for the 2 μs sample slot, sampling shall be done in the second microsecond (see figure 2.4).

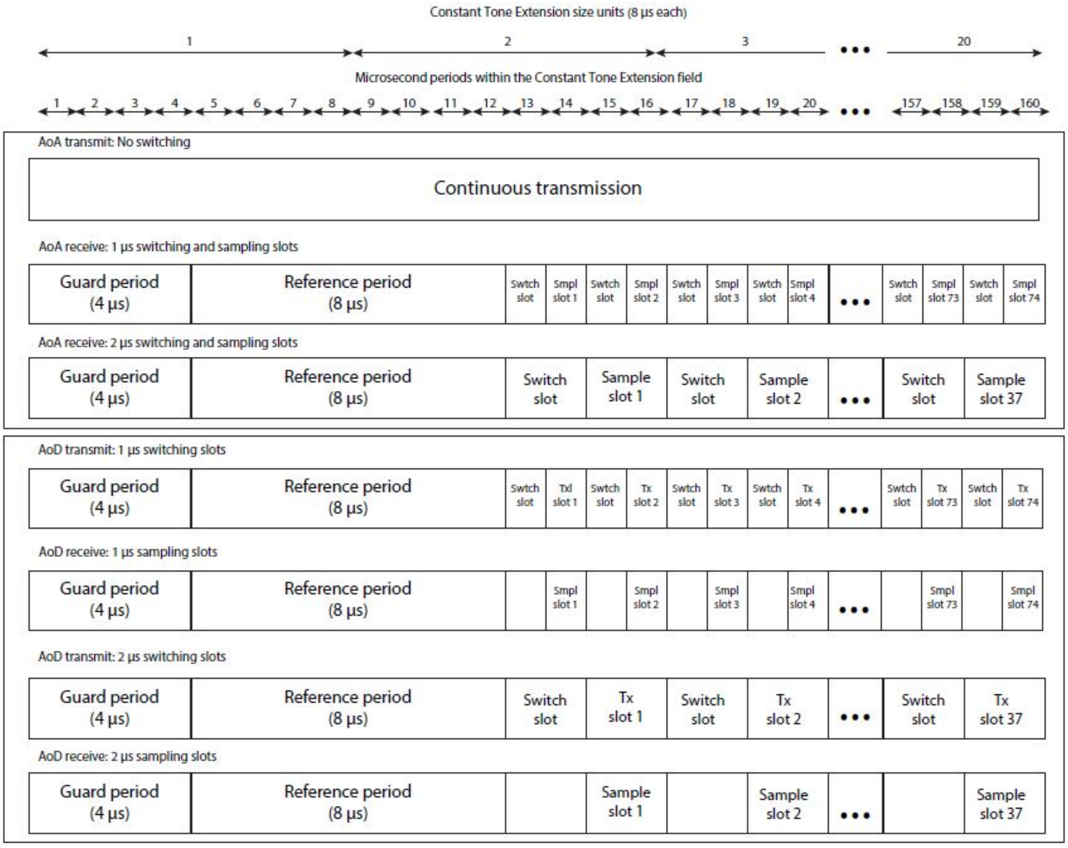

Figure 2.3: Constant Tone Extension Format

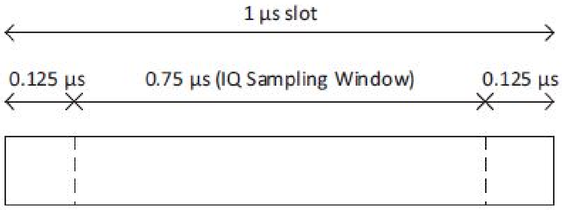

(a) 1 μs time slot

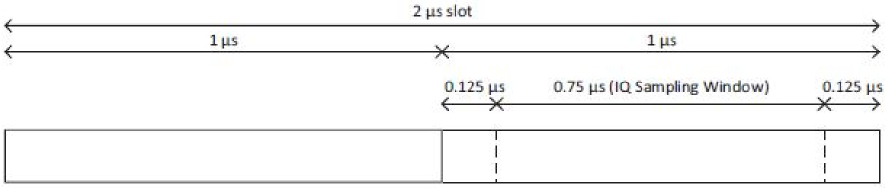

(b) 2 μs time slot

Figure 2.4: Sample Window [3]

3

Problem Formulation and Data Model

Wireless direction finding has a long history that can be traced back to the era when wireless communication initially came across people's eyes in the end of the $19th$ century. One of the first attempts on direction finding can be found in a patent owned by Scheller in 1906. This system was based on the directional property of antennas that was found by Heinrich Hertz. One year later, Bellini and Tosi discovered a DF principle that is named after them. They made use of two crossed directional antennas (e.g., loop antennas or dipole antennas) and rotated them accordingly such that antennas' principle radiating direction can be brought to the direction of received electromagnetic waves. Then a moving-coil goniometer was used to determine the angle. [21] Not long after the pioneers, the idea of using antenna arrays was come up with by Adcock and Keen in 1919 and 1938 respectively. [41]

Array processing has been an essential part of wireless direction finding especially after the advances in RF technologies and digital processing technologies in $20th$ century. It has a wide range of adoption in radar, radio astronomy, sonar, communications, direction finding, medical diagnosis, and treatment. [40] We start with formulating the direction finding problem using an antenna array.

Throughout the rest of the thesis, we denote scalars, vectors, and matrices by lower-case letters (e.g., s), lower-case letters with an arrow on the top (e.g., $\vec{x}$), and capital letters (e.g., X), respectively.

3.1. Fundamental Data Model

Consider a single emitter that is transmitting a wireless bandpass signal $u(t)$. The real bandpass signal $u(t)$ can be expressed in the complex format [29]:

$$u(t) = Re\{s(t)e^{j2\pi f_c t}\} = x(t)cos(2\pi f_c t) - y(t)sin(2\pi f_c t) \tag{3.1}$$

where $Re\{\}$ is the operation of taking real part of the signal inside the curly brace, $s(t) = x(t) + jy(t)$ is called the *baseband complex envelope* of signal $u(t)$, f_c is carrier frequency of signal $u(t)$. Such a signal $u(t)$ travels in the air then arrives at an antenna after a time τ, then the delayed arriving signal can be written as:

$$u_\tau(t) = Re\{s(t-\tau)e^{j2\pi f_c t}e^{-j2\pi f_c \tau}\} \tag{3.2}$$

The baseband complex envelope of this signal is then $s_\tau(t) = s(t-\tau)e^{-j2\pi f_c \tau}$. Suppose the bandpass signal is narrow-band, which is a valid assumption in the thesis since CTE is a single-tone sinusoid. As a result, the delayed version of the baseband envelope can be reformulated by the following analysis. Let $S(f)$ be the Fourier transform of $s(t)$, then the following relation holds:

$$\begin{aligned} s(t) &\Longleftrightarrow S(f) \\ s(t-\tau) &\Longleftrightarrow S(f)e^{-j2\pi f\tau} \end{aligned} \tag{3.3}$$

where $\Longleftrightarrow$ stands for Fourier transform. Let the bandwidth of $s(t)$ be BW. If BW is small enough such that $2\pi f\tau \approx 0$ for all $|f| \leq \frac{BW}{2}$, then $e^{-j2\pi f\tau}$ is approximated to be 1. As a result, Observing 3.3 gives the following relations:

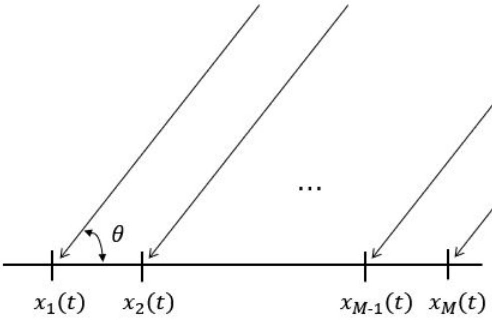

Figure 3.1: A Uniform Linear Array structure, with a signal source from far-field

$$s(t) \approx s(t-\tau) \tag{3.4}$$

$$s_\tau(t) \approx s(t)e^{-j2\pi f_c \tau} \tag{3.5}$$

With equation 3.5, the delay in time is translated into a shift in phase for a narrowband complex envelope. This narrowband approximation is the foundation of direction finding phased antenna arrays.

Consider a linear array consisting of M antennas with an uniform inter-element separation in space. Such an array is termed as Uniform Linear Array (ULA), which is the basic type of array that we use in the project. See figure 3.1. We chose ULA as the array geometry not only because of its simple structure but also because we want to make use of its shift-invariant property to tackle the coherent source problem using spatial smoothing in chapter 4. The inter-element separation is d meters.The wavelength of a narrowband signal with center frequency f_c has a wavelength given by $\lambda = c/f_c$, where c is the propagation speed of EM waves.

We consider the single user case first. Suppose an emitter that is located in the far-field of the array transmits a narrowband signal with complex envelope $s_0(t)$. The impinging direction of the signal to the array baseline is θ. The distance between the emitter and the reference antenna in the ULA, which is normally chosen to be the first antenna, is r. The corresponding time delay is then $\tau = r/c$. Then the received baseband signal at the reference antenna is

$$x_1(t) = a(\theta)\alpha s_0(t)e^{-j2\pi f_c \tau} \tag{3.6}$$

$$s(t) = s_0(t)e^{-j2\pi f_c \tau} \tag{3.7}$$

where α is the amplitude attenuation due to path loss, $a(\theta)$ is antenna response at direction described by θ. From now on, we change the notation of transmitted baseband complex signal $s(t)$ and delayed version $s_\tau(t)$ in equation 3.5 to be $s_0(t)$ and $s(t)$ for clarity. Similarly, the received signals by the other $M-1$ antennas can be expressed by the same formula with an extra phase term that is related to θ:

$$x_m(t) = a(\theta)\alpha s_0(t)e^{-j2\pi f_c \tau}e^{j2\pi(m-1)dcos(\theta)/\lambda} \tag{3.8}$$

The extra phase term comes from the different distance of propagation. The difference between propagation distance of $m-th$ antenna and the reference antenna is $\Delta\tau_m = (m-1)dcos(\theta)$, thus the corresponding phase difference is $\Delta\phi = 2\pi\Delta\tau_m/\lambda = 2\pi(m-1)dcos(\theta)/\lambda$. Stacking $x_m(t)$ for $m = 1,...,M$ gives us the vector expression of received signal by:

$$\vec{x}(t) = \begin{bmatrix} x_1(t) \\ x_2(t) \\ \vdots \\ x_M(t) \end{bmatrix} = \begin{bmatrix} 1 \\ e^{j\frac{2\pi dcos(\theta)}{\lambda}} \\ \vdots \\ e^{j\frac{2\pi(M-1)dcos(\theta)}{\lambda}} \end{bmatrix} a(\theta)s(t) + \begin{bmatrix} n_1(t) \\ n_2(t) \\ \vdots \\ n_M(t) \end{bmatrix} = \vec{a}(\theta)s(t) + \vec{n}(t) \tag{3.9}$$

where $\vec{a}(\theta)$ is the antenna array response vector, $\vec{n}(t)$ is spatially and temporally white Gaussian noise, $a(\theta)$ is the response of the individual antenna element. Here, we assume every antenna faces the same direction such that the antenna responses of all antenna elements are the same. Thus the scalar term $a(\theta)$ is used. Next, we consider multiple user case. The basic concepts are the same as the single user case. Suppose we have d users emitting signals from directions of $\{\theta_i\}$, for $i = 1, ..., d$. Then the received signal will be the linear superimposition of delayed and attenuated version of these signals:

$$\begin{aligned}\vec{x}(t) &= \sum_{i=1}^{d} \vec{a}(\theta_i)s_i(t) + \vec{n}(t) \\ &= A(\Theta)\vec{s}(t) + \vec{n}(t)\end{aligned} \tag{3.10}$$

where:

$$\Theta = \begin{bmatrix}\theta_1 & \theta_2 & \cdots & \theta_d\end{bmatrix} \tag{3.11}$$

$$A(\Theta) = \begin{bmatrix}\vec{a}(\theta_1) & \vec{a}(\theta_2) & \cdots & \vec{a}(\theta_d)\end{bmatrix} \tag{3.12}$$

$$\vec{s}(t) = \begin{bmatrix}s_1(t) & s_2(t) & \cdots & s_d(t)\end{bmatrix}^T \tag{3.13}$$

If we sample the signals at a certain sampling rate, and denote nth sampled data vector $\vec{x}(t)$ as a snapshot $\vec{x}[n]$, we can stack N snapshots into a data matrix by:

$$\begin{aligned}X &= \begin{bmatrix}\vec{x}[1] & \vec{x}[2] & \cdots & \vec{x}[N]\end{bmatrix} \\ &= \begin{bmatrix}\vec{a}(\theta_1) & \vec{a}(\theta_1) & \cdots & \vec{a}(\theta_1)\end{bmatrix}\begin{bmatrix}s_1[1] & s_1[2] & \cdots & s_1[N] \\ s_2[1] & s_2[2] & \cdots & s_2[N] \\ \vdots & \vdots & \ddots & \vdots \\ s_d[1] & s_d[2] & \cdots & s_d[N]\end{bmatrix} + \begin{bmatrix}\vec{n}[1] & \vec{n}[2] & \cdots & \vec{n}[N]\end{bmatrix} \\ &= AS + N\end{aligned} \tag{3.14}$$

As a result, the direction finding problem becomes a parameter estimation problem. The target is to find the parameters Θ in matrix A based on the received signal matrix X, and prior knowledge of the distribution of noise N. Formula 3.14 is the primary and classical array model used in the most of the direction finding literature. [33] However, some modifications have to be done to make the model more accurate within the content of Bluetooth LE.

3.2. Modified Data Model

The fundamental antenna array data model expressed by 3.14 is the idealized model. In reality, the actual data model may vary depending on several factors. The factors are typically from physical phenomena and hardware imperfections, for examples, the mutual coupling among antenna elements and the switch imbalance in the receiver. This category introduces unpredictable phase shifts on received signals and requires array calibration. Apart from array mismodeling, a Bluetooth LE receiver accesses multiple antennas sequentially with a switch, which is unique to the normal array processing where antennas are accessed simultaneously with multiple receivers.

3.2.1. Multipath Signal Model

Bluetooth LE primarily operates in indoor environments. One character of such an environment is the dense distribution of obstacles and reflectors in a relatively small area. As a result, the heavy multipath effect exists, see figure 3.2. Wireless signals can be specularly or diffusely reflected off the walls or furniture when they impinge on these objects. As a result, multiple delayed and attenuated rays of the original signal will arrive

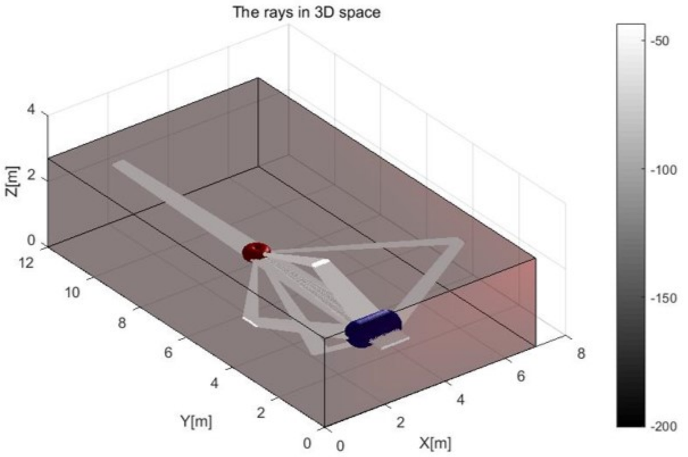

Figure 3.2: Multipath Environment

and superimpose at the receiver including the line-of-sight (LOS) path. The multipath wireless channel can be characterized as [1]:

$$u_r(t) = Re\left\{ \sum_{i=0}^{d(t)-1} \alpha_i(t) s_0(t - \tau_i(t)) e^{j2\pi f_c(t-\tau_i(t))} \right\} \tag{3.15}$$

where $d(t)$ is the number of multipath components in the wireless channel, $\alpha_i(t)$ is the amplitude attenuation of ith path, $\tau_i(t)$ is the time delay of the ith path, $u_r(t)$ is the received bandpass signal, $s_0(t)$ is the transmitted baseband complex signal, $i = 0$ denotes the LOS path. The channel parameters are time-variant because of movements in the channel. For Bluetooth LE direction finding, CTE lasts maximally 160 μs, which is short enough to assume that there is no channel variation within the period of CTE reception. Hence, it's valid to assume the channel parameters are constant throughout the direction finding operation. For an antenna array, the baseband envelope that arrives at the $1st$ antenna element is:

$$x_1(t) = \sum_{i=0}^{d-1} \alpha_i s_0(t) e^{-j2\pi f_c \tau_i} \tag{3.16}$$

If we regard each path as a signal that is from a distinct virtual source, and we do not take interference into account, then the S matrix in equation 3.14 can be written as:

$$\begin{aligned} S &= \begin{bmatrix} s_1[1] & s_1[2] & \cdots & s_1[N] \\ s_2[1] & s_2[2] & \cdots & s_2[N] \\ \vdots & \vdots & \ddots & \vdots \\ s_d[1] & s_d[2] & \cdots & s_d[N] \end{bmatrix} \\ &= \begin{bmatrix} \alpha_0 e^{-j2\pi f_c \tau_0} & 0 & \cdots & 0 \\ 0 & \alpha_1 e^{-j2\pi f_c \tau_1} & \cdots & 0 \\ \vdots & \vdots & \ddots & \vdots \\ 0 & 0 & \cdots & \alpha_{d-1} e^{-j2\pi f_c \tau_{d-1}} \end{bmatrix} \begin{bmatrix} s_0[1] & s_0[2] & \cdots & s_0[N] \\ s_0[1] & s_0[2] & \cdots & s_0[N] \\ \vdots & \vdots & \ddots & \vdots \\ s_0[1] & s_0[2] & \cdots & s_0[N] \end{bmatrix} \\ &= MS_0 \end{aligned} \tag{3.17}$$

The matrix M contains multipath parameters of all components on its diagonal entries. Matrix S_0 is rank one since its rows are identical. As a result, the signal matrix S is of only rank one.

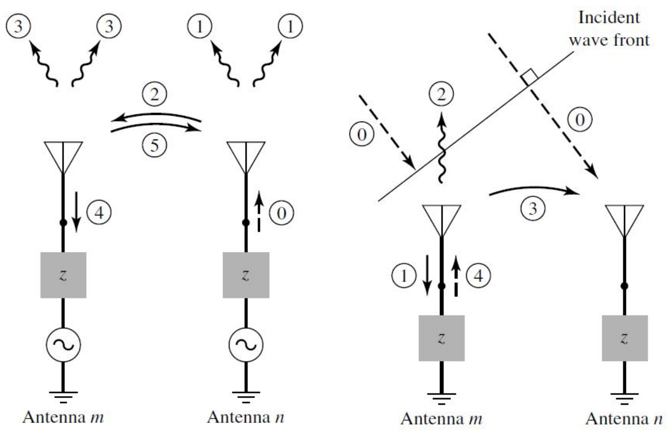

(a) Transmission Mode

(b) Reception Mode

Figure 3.3: Mutual Coupling in Antenna Array. [2]

3.2.2. Mutual Coupling

The existence of nearby antennas within an antenna array not only brings us the spatial diversity but also raises additional signal distortion due to the interaction that is named as Mutual Coupling (MC). Elaboration of such an effect is figure 3.3.

Antennas are passive devices which may generate radiated EM waves due to some excitation. Essentially the excitation of radiation is the alternating current distribution on antennas [2], which is either from time-varying current source, discontinued or curved antenna shapes. Suppose an antenna is in transmission mode, as depicted in figure 3.3a. Antenna n radiates into space in (1) due to a current source. Meanwhile, the radiated wave also impinges on the adjacent antennas as (2). This portion of radiation induces current flow on the adjacent antennas and excites additional radiation in (3) and (5). The induced radiation and reflection/scattering (5) from the neighboring antenna comes back to antenna n then the same procedure repeats.

The similar phenomenon also happens in the reception mode, see figure 3.3b. The incident wave (0) impinges at antenna m. The induced current (1) and reflected current (4) induces additional radiation. This radiation together with reflected and scattered EM waves goes to neighboring antennas in (3) and induces the current again.

The effect of mutual coupling influences the performance of an antenna array since unknown and additional signal components are contributed to the original signals in each antenna. Its influence on the array performance in direction finding was thoroughly studied over decades, for instance, see [38], [31], and [10]. The mutual coupling matrix can characterize the effect of MC on the antenna array in reception mode. As a result, the antenna array model can be rewritten as :

$$X_m = CAS + N \tag{3.18}$$

$$C = \begin{bmatrix} C_{11} & C_{12} & \cdots & C_{1M} \\ C_{21} & C_{22} & \cdots & C_{2M} \\ \vdots & \vdots & \cdots & \vdots \\ C_{M1} & C_{12} & \cdots & C_{MM} \end{bmatrix} \tag{3.19}$$

where C is a complex symmetric square matrix if the array structure and antenna response are symmetric such that the entry C_{ij} and C_{ji} has the same value. The entry C_{ij} specifies the voltage contribution from antenna j to antenna i. Matrix C can be simplified to be a band matrix because the MC between elements that are far apart are small enough to be neglected. In some literature, the diagonal elements of matrix C are approximated to be constant provided that the antenna impedance termination conditions are the same [10]. However, in practice, it's not strictly true when the antenna array is of finite size. The antenna elements in the middle and the edges experience different MC, such that they also have different reflection coefficients. For instance, the reflection coefficients of the first and fourth antenna in the mutual coupling matrix visualized in figure 5.16 on a 8-element ULA at $2.4GHz$ are $-0.0204-0.0028i$ and $-0.0288+0.0420i$.

3.2.3. Path Imbalance and Switch Leakage

Despite the physical phenomena such as MC, hardware imperfections are another set of mis-modeling source for antenna arrays[20]. The antennas have to be connected to the receiver via cables. Moreover, between the antennas and receiver, there is also a multiple-port RF switch according to the BLE specification. A sketch that depicts the structure of a BLE direction finding system is figure 3.4.

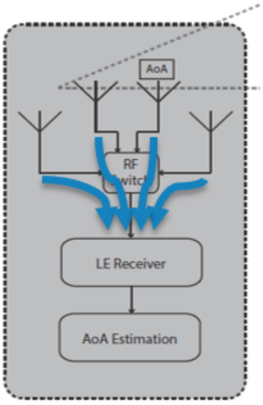

Figure 3.4: Path Imbalance and Switch Leakage in an BLE Direction Finding System

Transmission paths between antennas and the RF switch are formed by the cables and switch. These cables may have different lengths and attenuation such that they result in the path imbalance. The path imbalance is not only because of the quality of the cable and the switch but also depend on the way the cables are bent when assembling the system.

Moreover, the switch may leak from those ports that are turned off, such that an extra mixture of signals from other antennas is present. To conclude, the effect of path imbalance and switch leakage can be summarized into one matrix:

$$L = \begin{bmatrix} a_{11}e^{jb_{11}} & 0 & \cdots & 0 \\ 0 & a_{22}e^{jb_{22}} & \cdots & 0 \\ \vdots & \vdots & \ddots & \vdots \\ 0 & \cdots & 0 & a_{MM}e^{jb_{MM}} \end{bmatrix} \tag{3.20}$$

where a_{ii} denotes the insertion loss of ith port, b_{ii} is phase delay term between port i and output port when port i is switched on. These parameters all include cable. The off-diagonal components are approximated to be 0, because the isolation of the off-ports are normally below $-50dB$ in modern RF switches. The data model can be modified based on formula 3.18 to be:

$$X_l = LAS + N \tag{3.21}$$

3.3. Using Multiple Antennas with One Receiver

In this project, a unique distinction to the usual antenna array processing is that we use only one receiver to access multiple antennas. We sequentially sample the multiple antennas by using an RF switch. But all derivations in the section 3.1 are based on the assumption that all antennas are sampled simultaneously, such that the entries in the data vector $\vec{x}(t)$ are all from the same time instant. In this section, we are going to address the equivalent data model of the switched antenna mechanism, and discuss the factor that may destroy the equivalence - CFO.

(a) Return-to-First

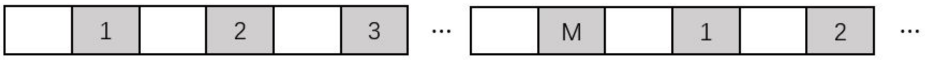

(b) Round-Robin

Figure 3.5: Examples of Switching Patterns (gray slots are sample slots).

3.3.1. The Equivalent Data Model

With sequential sampling, to construct a similar data vector to $\vec{x}(t)$, we need to stack samples from different time instances. We used Return-to-First switching pattern throughout the thesis, the switching pattern is illustrated in figure 3.5a. We call a round of complete scan of all antennas an antenna scan. For example, the period from the first sample of antenna 1 to the first sample of antenna M in figure 3.5a is an antenna scan. Antenna scans are repeated until the length of the CTE is exhausted.

With Return-to-First pattern, we collect the unique samples from each antenna scan to a data vector. Because we have more than one samples from the $1st$ antenna during an antenna scan, we take only the first one to represent the $1st$ antenna in the data vector. Thus, the data vector with sequential sampling at time t is then:

$$\vec{x}_{ss}(t) = \begin{bmatrix} x_1(t) \\ x_2(t+2T_{slot}) \\ x_3(t+6T_{slot}) \\ \vdots \\ x_M(t+(4M-6)T_{slot}) \end{bmatrix} := \begin{bmatrix} x_1(t) \\ x_2(t+\Delta T_{s2}) \\ x_3(t+\Delta T_{s3}) \\ \vdots \\ x_M(t+\Delta T_{sM}) \end{bmatrix} \tag{3.22}$$

where $x_i(t)$ denotes the signal received by the ith antenna, T_{slot} is the slot duration, M is the number of antennas, ΔT_{si} is the time delay of ith antenna to the first sample of the antenna scan, $\Delta T_{s1} = 0$. The corresponding matrix form is:

$$X_{ss} = \begin{bmatrix} x_1(t) & x_1(t+\Delta T_{as}) & \cdots & x_1(t+(N-1)\Delta T_{as}) \\ x_2(t+\Delta T_{s2}) & x_2(t+\Delta T_{s2}+\Delta T_{as}) & \cdots & x_2(t+\Delta T_{s2}+(N-1)\Delta T_{as}) \\ \vdots & & & \\ x_M(t+\Delta T_{sM}) & x_M(t+\Delta T_{sM}+\Delta T_{as}) & \cdots & x_M(t+\Delta T_{sM}+(N-1)\Delta T_{as}) \end{bmatrix} \tag{3.23}$$

where ΔT_{as} is the time interval between two successive antenna scans. For Return-to-First switching pattern, $\Delta T_{as} = \Delta T_{sM} + 2T_{slot}$, where T_{slot} is the slot duration, which can be $1\mu s$ or $2\mu s$. Based on the assumption that the channel stays unchanged during an antenna scan, the ith entry in the vector $\vec{x}(t)$ based on equation 3.16 with the presence of noise is:

$$x_i(t+\Delta T_{si}) = \sum_{i=0}^{d-1} \alpha_i e^{-j2\pi f_c \tau_i} s_0(t+\Delta T_{si}) + n_i(t+\Delta T_{si}) \tag{3.24}$$

Because the source signal $s_0(t)$ is CTE in this case, which is constant, we have $s_0(t+\Delta)T_{si} = s_0(t)$. Moreover, the noise in consideration is Gaussian noise that is both spatially and temporally white. Thus it's equivalent to write $n_i(t+\Delta T_{si}) = n_i(t)$ from the statistical perspective. As a result, equation 3.24 implies that the following relation holds:

$$x_i(t+\Delta T_{si}) = x_i(t) \tag{3.25}$$

As a result, the data vector with sequential sampling can be equivalent to the simultaneous sampling case by:

$$\vec{x}(t) = \vec{x}_{ss}(t) \tag{3.26}$$

Note that if the channel changes during an antenna scan, the channel parameters in 3.24 are different for different $x_i(t+\Delta T_{si})$s. Thus the equivalence in equation 3.26 does not hold anymore.

At this point, we can conclude that with the assumptions that the channel keeps unchanged during an antenna scan, and that the noise is spatially and temporally white, we can formulate the data model with sequential sampling in the same way as simultaneous sampling case.

3.3.2. The Influence of CFO

The equivalence analysis of data model is based on the signals in equation 3.24 are all in basedband. However, the low-cost receivers like BLE use local oscillators with relatively high ppm (up to 40 ppm), which could lead to carrier frequency offsets (CFO) in the received signals. As a result, the CFO Δf_c changes the equation 3.24 by:

$$x_i(t+\Delta T_{si}) = e^{j2\pi\Delta f_c(t+\Delta T_{si})} \sum_{i=0}^{d-1} \alpha_i e^{-j2\pi f_c \tau_i} s_0(t+\Delta T_{si}) + n_i(t+\Delta T_{si}) \tag{3.27}$$

As a result, even though the source $s_0(t)$ is constant over the antenna scan, there is still a phase progression. Thus the equality in equation 3.25 doe not hold anymore. Figure 3.6 shows this effect with the absence of noise. The figures consider a half-wavelength ULA receiving a single signal whose AoA is 30°. Such that the received signals by antenna 1 and 2 have a constant phase difference of 155.9°. Figure 3.6a shows the received signals when CFO is not present. The signals are constant as expected in equation 3.25. When a $50kHz$ CFO is present, as depicted in figure 3.6b, both received signals start to progress in phase. In both figures, t_{si} denotes the sampling time of ith antenna in an antenna scan, such that $\Delta T_{si} = t_{si} - t_{s1}$. The equation 3.25 can be re-written as:

$$x_i(t+\Delta T_{si}) = x_i(t) e^{j2\pi\Delta f_c \Delta T_{si}} \tag{3.28}$$

The data vector (with sequential sampling) then can be written as:

$$\vec{x}_{ss}(t) = \begin{bmatrix} x_1(t) \\ x_2(t+\Delta T_{s2}) \\ x_3(t+\Delta T_{s3}) \\ \vdots \\ x_M(t+\Delta T_{sM}) \end{bmatrix} = \begin{bmatrix} x_1(t) \\ x_2(t)e^{j2\pi\Delta f_c \Delta T_{s2}} \\ x_3(t)e^{j2\pi\Delta f_c \Delta T_{s3}} \\ \vdots \\ x_M(t)e^{j2\pi\Delta f_c \Delta T_{sM}} \end{bmatrix} = \begin{bmatrix} 1 & 0 & \cdots & 0 \\ 0 & e^{j2\pi\Delta f_c \Delta T_{s2}} & \cdots & 0 \\ \vdots & \vdots & \ddots & \vdots \\ 0 & 0 & \cdots & e^{j2\pi\Delta f_c \Delta T_{sM}} \end{bmatrix} \begin{bmatrix} x_1(t) \\ x_2(t) \\ x_3(t) \\ \vdots \\ x_M(t) \end{bmatrix} \tag{3.29}$$

Then the data model with sequential sampling shall be modified to be:

$$\vec{x}_{ss}(t) = O\vec{x}(t) = OA\vec{s}(t) + \vec{n}(t) \tag{3.30}$$

$$O = \begin{bmatrix} 1 & 0 & \cdots & 0 \\ 0 & e^{j2\pi\Delta f_c \Delta T_{s2}} & \cdots & 0 \\ \vdots & \vdots & \ddots & \vdots \\ 0 & 0 & \cdots & e^{j2\pi\Delta f_c \Delta T_{sM}} \end{bmatrix} \tag{3.31}$$

Because matrix O is diagonal and only introduces fixed phase shift, thus multiplying it to the noise term does not affect the distribution of the noise, so the noise term is left unchanged.

Parameter ΔT_{sm} depends on the duration of the CTE slots, and the switching pattern. When using Return-to-First pattern:

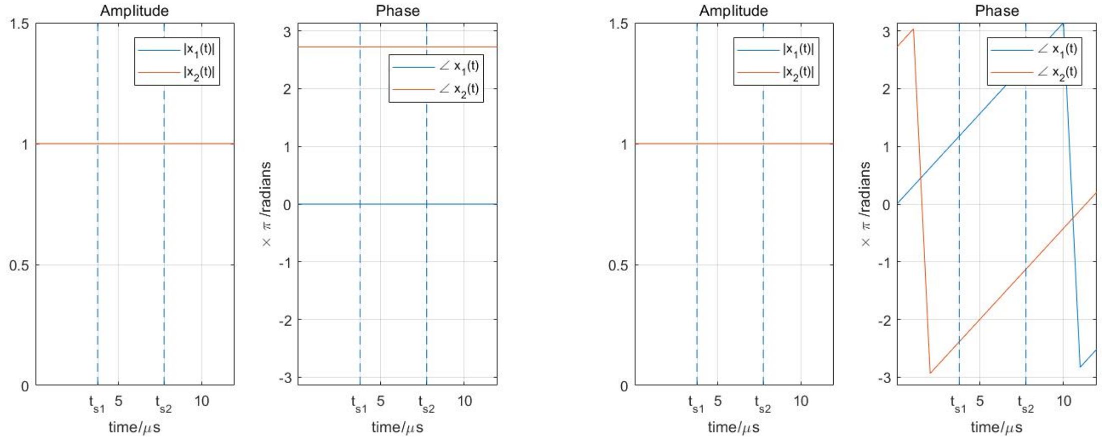

(a) Without CFO

(b) With $50kHz$ CFO

Figure 3.6: Sampling Time Misalignment

$$\Delta T_{sm} = \begin{cases} 0, & m = 1 \\ [2+4(m-2)]\,T_{slot}, & 2 \leq m \leq M \end{cases} \tag{3.32}$$

where T_{slot} is CTE slot duration, which is either $1\mu s$ or $2\mu s$.

3.4. Final Data Model and Estimation Target

To conclude this chapter, a new array model with antenna switching is formulated by taking array mismodeling into account. According to equations 3.14, 3.18, 3.21, and 3.30, the final antenna array model in matrix form can be formulated:

$$X_{ss} = OLCAS + N = A_r(\Theta)S + N \tag{3.33}$$

The matrix $A_r(\Theta)$ is calibrated antenna array response. The multiplication of O, L, and C is in such an order because coupling is the first phenomenon that takes place. After the interaction between antennas the signals goes into the switch so L is multiplied secondly. The CFO term is due to the sequential sampling which happens after the switch, such that the CFO term is on the left-most side. The noise term in equation 3.33 is independent from the mis-modeling terms. This is because the front end of a receiver (power amplifier) is the dominant source of noise for BLE systems. The switch imbalance, and mutual coupling effect happens before the signal gets into the receiver front-end such that these two terms apply to the signal matrix only. As for the CFO, the matrix O is a diagonal matrix containing only constant phase shifts, thus it does not influence the distribution of the noise.

Matrices O, L, and C introduce additional phase distortion to the received data matrix. If we use idealized antenna array matrix A, the estimation of AoA may be biased due to the phase distortion. Thus, the first aim of the thesis is obtaining these matrices. Then their influence and calibration methods can be analyzed.

The other target of this thesis is finding the bearing of a peer transmitting BLE device by estimating the AoA of LOS path. Recall the signal model in equation 3.17, d paths of coherent signals impinges at the receiving array including the LOS path. The coherent property of the signal model degrades the performance of subspace-based DF algorithm MUSIC. Moreover, only the LOS direction tells the information of peer device's bearing. Thus, in summary, the estimation algorithm has to tackle the coherent multipath environment and to identify the LOS direction from all multipath components.

4

Direction Finding Using Bluetooth LE

In this chapter, a super-resolution DF algorithm MUSIC is introduced first as the basis of our proposed direction finding algorithms. Then, we will introduce the techniques and algorithms that are used for achieving the targets that are derived from the last chapter. Several array calibration/modeling methods are considered and analyzed first. The most feasible and convenient method was chosen for this thesis. Next, based on the MUSIC algorithm, we proposed a supplemental algorithm for the multipath environment and LOS identification. Moreover, a new algorithm based on CLEAN and MUSIC is proposed. Its constraints and benefits are discussed next.

4.1. Sub-Space Based Algorithm - MUSIC

MUltiple SIgnal Classification (MUSIC) is proposed by [33] for estimating the bearing of wireless signals that are potentially from multiple sources. This algorithm is also referred to as super-resolution algorithm because it overcomes the resolution limitation introduced by the antenna array beam-width. This is done by utilizing the eigenvalue analysis of the covariance matrix of the data matrix, then separating the signal space and noise space according to the orthogonality property of eigenvectors.

We start the analysis from the array data model in equation 3.14. We assume the noise and signals are independent, and the noise is temporally and spatially white, which are normally valid. Then the true covariance matrix $R_x = E\{\vec{x}\vec{x}^H\}$ of the received signal vector can be approximated using N snapshots by the sample covariance $\hat{R}_x$:

$$\begin{aligned}\hat{R}_x &:= \frac{1}{N}XX^H \\ &= \frac{1}{N}(ASS^HA^H + ASS^H + NS^HA^H + NN^H) \\ &= \frac{1}{N}ASS^HA^H + \frac{1}{N}NN^H \\ &= A\hat{R}_sA^H + \sigma^2 I\end{aligned} \tag{4.1}$$

where σ^2 is the variance of noise, matrix I is a $M \times M$ identity matrix, M is the number of elements in the antenna array, $\hat{R}_s = \frac{1}{N}SS^H$ is the sample covariance matrix of source. We first consider the eigenvalue analysis when there are d independent sources without noise:

$$\hat{R}_x = U\Lambda U^H \tag{4.2}$$

Matrix U is $M \times M$ eigenvector matrix containing normalized eigenvectors as columns, while Λ is $M \times M$ diagonal matrix containing corresponding eigenvalues in non-increasing order ($\lambda_1 \geq \lambda_2 \geq ... \geq \lambda_M$). Because the rank of matrix X is d, there are only d non-zero eigenvalues. Then the dimension of U and Λ can be reduced:

$$\hat{R}_x = A\hat{S}_sA^H = U_s\Lambda_sU_s^H \tag{4.3}$$

where Λ_s is $d \times d$, U_s is $M \times d$ containing corresponding eigenvectors. We name the column subspace of U_s as signal space. We put the rest of eigenvectors into another matrix U_n, namely noise space. Then, the whole eigenvector matrix can be written as $U = [U_s | U_n]$. The corresponding eigenvalues of noise space depend on the variance of the noise, which means the noise space has different eigenvalues from those belonging to signal space. Combining the fact that the eigenvectors are normalized, we can conclude that matrix U is unitary.

Making use of the property of unitary matrices, the noise term in equation 4.1 can be reformulated:

$$\begin{aligned} \sigma^2 I &= \sigma^2 U U^H \\ &= \sigma^2 \begin{bmatrix} U_s & U_n \end{bmatrix} \begin{bmatrix} U_s^H \\ U_n^H \end{bmatrix} \\ &= \sigma^2 (U_s U_s^H + U_n U_n^H) \end{aligned} \tag{4.4}$$

Inserting 4.3 and 4.4 into 4.1:

$$\begin{aligned} \hat{R}_x &= U_s \Lambda_s U_s^H + \sigma^2 (U_s U_s^H + U_n U_n^H) \\ &= U_s (\Lambda_s + \sigma^2 I_d) U_s^H + U_n \sigma^2 I_{M-d} U_n^H \\ &= \begin{bmatrix} U_s & U_n \end{bmatrix} \begin{bmatrix} \Lambda_s + \sigma^2 I_d & 0 \\ 0 & \sigma^2 I_{M-d} \end{bmatrix} \begin{bmatrix} U_s^H \\ U_n^H \end{bmatrix} \\ &= U \Lambda U^H \end{aligned} \tag{4.5}$$

It's clear that the eigenvalues of signal space are larger than a floor. In practice, we can find the signal space by looking for the eigenvalues that are larger than the noise variance. According to equation 4.3, the columns of U_s and columns of A spans the same subspace. As a consequence, A is orthogonal to noise space U_n. Then, the estimation of parameters θ in A can be obtained by minimizing the following cost function:

$$J(\theta) = \vec{a}(\theta)^H U_n U_n^H \vec{a}(\theta) \tag{4.6}$$

where $\vec{a}(\theta)$ is the array response vector. The curve of the cost function to θ is called MUSIC pseudo-spectrum. Finding the d lowest peaks in the spectrum gives the estimate of AoAs of d signals. For more intuitive spectrum graph, we normally use the normalized inverse cost function to find the maxima rather than the minima:

$$J(\theta) = \frac{\vec{a}(\theta)^H \vec{a}(\theta)}{\vec{a}(\theta)^H U_n U_n^H \vec{a}(\theta)} \tag{4.7}$$

In the cost function, the scalar array element response $a(\theta)$ in equation 3.9 cancels out. Thus we do not consider the antenna pattern throughout the project. The cost function addresses the importance of an accurate array model. The mismodeling of array response may destroy its orthogonality with noise space. Moreover, the ability to resolve d independent peaks relies on the assumption that the matrix R_s is of full rank. Otherwise, $A R_s A^H$ is rank deficient. The dimension of signal space would be less than d. The steering vectors merge into one vector linearly. The resulting vector is not a legitimate steering vector anymore [25][35].

4.2. Array Calibration

Recall the realistic antenna array model in equation 3.33. Two mis-modeling factors that mutate the original array response matrix are added to the ideal response matrix. The estimation and compensation of these factors are often referred to as array calibration.

4.2.1. Mutual Coupling

Mutual coupling compensation techniques can be roughly divided into four categories: self-calibration methods (or online methods), mutual impedance-based methods, active antenna pattern based methods, and S parameter based methods. Most of these methods either are derived under some assumption of antenna type and geometry (most interests are in linear dipole arrays), or involves massive costs of computation and memory [13]. This section will give overviews of these methods, and analyze the trade-offs between computational complexity and efficiency to find a most suitable method for our project.

Self-Calibration Method

Friedlander and Weiss proposed a self-calibration method for direction finding with the presence of mutual coupling in [10] in 1991. The algorithm considers the mutual coupling, antenna gain and phase uncertainties in the array model:

$$X = C\Gamma AS + N \tag{4.8}$$

$$\Gamma = diag\{\alpha_1 e^{-j2\pi f_c\phi_1},\ \alpha_2 e^{-j2\pi f_c\phi_2},\ ...,\ \alpha_M e^{-j2\pi f_c\phi_M}\} \tag{4.9}$$

where α_m and ϕ_m are gain and delay of antenna m, respectively. The estimation of Γ, C and $\{\theta_n\}$ is still based on the orthogonality with noise space. A reasonable estimation can be obtained by solving the minimization problem:

$$\min_{\{\theta_n\},\Gamma,C} \sum_{n}^{d} \parallel U_n^H C\Gamma\vec{a}(\theta_n) \parallel^2 \tag{4.10}$$

The cost function is based on the cost function 4.6. The algorithm proposed by Friedlander is based on some approximations. They assume C to be banded Toeplitz such that the coupling between any two equally spaced antennas are the same and the coupling coefficients between two far-apart antennas are negligible. The procedure of solving the minimization problem is iterative. Initially, the prior knowledge of Γ and C is used, and the normal MUSIC operation is carried out to obtain initial guesses of $\{\theta_n\}$. Next, with the estimated $\{\theta_n\}$, given C, and a linear constraint of $\Gamma_{11} = 1$, the cost function is minimized with respect to Γ. Finally, given Γ, $\{\theta_n\}$, and a linear constraint $C_{11} = 1$, the cost function is minimized on mutual coupling coefficients. The procedure is repeated until J converges.

The minimization solution in the last two steps is derived in closed form. Specifically, the solution of step three is based on the assumption that the mutual coupling matrix C is banded Toeplitz, which is not true for a linear array with finite size. Furthermore, the Toeplitz assumption imposes a symmetry constraint of an antenna array system, but the presence of local scatterers can destroy the symmetry. [12] suggests that the algorithm fails with local scatterers. Besides, the uniqueness of the solution is not proven in [10], either.

Mutual Impedance Method

The first attempt to analyze the effect of mutual coupling on small antenna arrays is based on open-circuit mutual impedance by Gupta and Ksienski [11][16]. Later this idea was adopted to compensate the mutual coupling effect for direction finding with a dipole array in [49]. This method recovers the open circuit output voltage of uncoupled antennas using the mutual impedance, whose definition is the same as Z parameters. The compensation is done by:

$$\begin{bmatrix} V_{oc1} \\ V_{oc2} \\ \vdots \\ V_{ocM} \end{bmatrix} = \begin{bmatrix} 1+\frac{Z_{11}}{Z_L} & \frac{Z_{12}}{Z_L} & \cdots & \frac{Z_{1M}}{Z_L} \\ \frac{Z_{21}}{Z_L} & 1+\frac{Z_{22}}{Z_L} & \cdots & \frac{Z_{2M}}{Z_L} \\ \vdots & \vdots & \ddots & \vdots \\ \frac{Z_{M1}}{Z_L} & \frac{Z_{M2}}{Z_L} & \cdots & 1+\frac{Z_{MM}}{Z_L} \end{bmatrix} \begin{bmatrix} V_1 \\ V_2 \\ \vdots \\ V_M \end{bmatrix} \tag{4.11}$$

where $Z_{ij} = \frac{V_i}{I_j}\Big|_{I_k=0\ for\ k\neq j}$ are mutual impedances between antenna elements, Z_L is the load impedance of antennas, V_m for $m = 1,2,...,M$ are received voltages including mutual coupling, V_{ocm} for $m = 1,2,...,M$ are coupling-free open circuit voltage at the port of mth antenna. The mutual impedance between two thin wire antennas is expressed as:

$$Z_{ij} = \frac{V_{ij}}{I_j} = -\frac{1}{I_i(0)I_j(0)}\int_{-l_i/2}^{l_i/2} E_{ij}(\mathbf{r})I_i(\mathbf{r})dl \tag{4.12}$$

where V_{ij} is induced open circuit voltage on antenna i because of the radiation from antenna j, $I_i(0)$ is the current of antenna i at the feeding point, E_{ij} is the electric field component radiated by antenna j which is parallel to antenna i. This equation can be calculated by using the Integral Equation-Moment Method, or Induced EMF Method [2].

A few comments can be made about this method: First, this method introduces error when analyzing receiving antenna array. Equation 4.12 is derived based on the assumption that the antennas are excited by internal sources, while in receiving mode, antennas are excited by impinging waves from outside. Second, the open circuit voltage is calculated based on a Thevenin equivalent circuit. It assumes the affected antenna j is short-circuited. The open circuit voltage is calculated then by multiplying the short circuit current and the equivalent impedance. However, [16] points out that there are still some arguments about the validity of Thevenin equivalence, especially when modeling a receiving antenna.

Hui proposed a new definition of mutual coupling in [15] to overcome the drawbacks of open circuit mutual impedance method. It tries to obtain the coupling-free received voltage on the antenna loads when they are operating in receiving mode. This method is also called Receiving Mutual Impedance Method (RMIM). With respect to this method, the previous method is called Conventional Mutual Impedance Method (CMIM). The definition of the receiving mutual coupling is the ratio of the induced voltage across the antenna terminal i and the induced current on antenna terminal j that is excited only by an impinging wave:

$$Z_t^{ij} = \frac{V_i}{I_j} \tag{4.13}$$

The calculation can be done with EM wave simulators such as FEKO by calculating the received voltage with and without neighboring antenna elements. [18] Measurements can also obtain the receiving mutual impedance. This can be carried out in an anechoic chamber. Scattering parameters under particular conditions are measured, then the S parameters are converted to mutual impedance. [17] After obtaining the mutual impedance, the un-coupled received voltage across the load can be recovered by [50]:

$$\begin{bmatrix} U_1 \\ U_2 \\ \vdots \\ U_M \end{bmatrix} = \begin{bmatrix} 1 & -\frac{Z_t^{12}}{Z_L} & \cdots & -\frac{Z_t^{1M}}{Z_L} \\ -\frac{Z_t^{21}}{Z_L} & 1 & \cdots & -\frac{Z_t^{2M}}{Z_L} \\ \vdots & \vdots & \ddots & \vdots \\ -\frac{Z_{M1}}{Z_L} & -\frac{Z_{M2}}{Z_L} & \cdots & 1 \end{bmatrix} \begin{bmatrix} V_1 \\ V_2 \\ \vdots \\ V_M \end{bmatrix} \tag{4.14}$$

It was shown in the same literature that RMIM is superior to CMIM in direction finding applications.

So far, we can summarize the mutual impedance methods. CMIM and RMIM both try to characterize and quantify mutual coupling by finding mutual impedance. CMIM has drawbacks because of the definition of the conventional mutual impedance and its Thevenin equivalence when modeling the antenna. RMIM overcomes these drawbacks. However, these mutual impedance-based methods do not take the influence of local scatterers into consideration. In practice, the reflection and scattering from both neighboring antenna elements and nearby objects are all sources of mutual coupling. It is particularly true in indoor environments. Besides, the amount of computation involved in obtaining the parameters is substantial.

Active Antenna Pattern Method

The other direction of research is called active or embedded antenna pattern methods. They look for the radiation pattern of each antenna element when they are excited while the others are terminated [19][28]. The active antenna patterns can be used to formulate the array response vector.

The problem with this class of methods is that the whole angular space is discretely separated. Only on a limited number of angles, the array response is accurate. To obtain higher resolution a large memory is required even with interpolation techniques, which estimates the array response in intervening directions, for instance, see [34] and [44].

S Parameter Method

Steyskal in [38] gave another way to characterize the mutual coupling matrix. The well-known scattering matrix can be used to derive the coupling matrix in a relatively easy way. [41]

See figure 4.1, it depicts the voltage wave flowing in a two-antenna array in transmitting mode. An antenna array can be modeled to be an M-port network. The connection point between the antenna and transmission line is defined to be the ports. In the picture, a_i denotes the incident power wave in port i, b_i denotes the

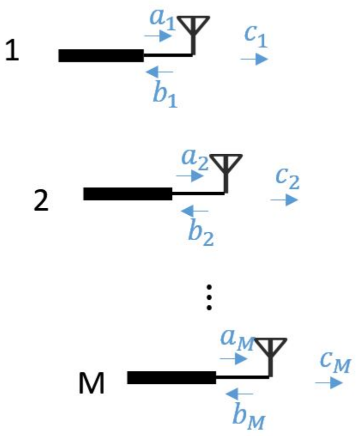

Figure 4.1: Voltage Flow on A Transmitting Antenna Array

reflected power wave in port i, while c_i denotes the power wave that goes into the antenna. The incident and reflected power waves are defined as: [22]

$$a_i = \frac{V_i + Z_i I_i}{2\sqrt{|Re\{Z_i\}|}} \tag{4.15}$$

$$b_i = \frac{V_i - Z_i^* I_i}{2\sqrt{|Re\{Z_i\}|}} \tag{4.16}$$

where V_i and I_i are the voltage at and the current flowing into the ith port, Z_i is the impedance looking from the ith antenna to its transmission line. So the incident and reflected power waves a_i and b_i are voltages of incident and reflected waves that are normalized in such a way that the square of them are powers incident on and emerging from the ith port.

According to the definition of scattering parameters:

$$\begin{bmatrix} b_1 \\ b_2 \\ \vdots \\ b_M \end{bmatrix} = \begin{bmatrix} S_{11} & S_{12} & \cdots & S_{1M} \\ S_{21} & S_{22} & \cdots & S_{2M} \\ \vdots & \vdots & \ddots & \vdots \\ S_{M1} & S_{M2} & \cdots & S_{MM} \end{bmatrix} \begin{bmatrix} a_1 \\ a_2 \\ \vdots \\ a_M \end{bmatrix} \tag{4.17}$$

If all ports are terminated by the same impedance, meaning Z_i for $i = 1,2,...,M$ are all the same, then the equation 4.17 can be re-written to be:

$$\begin{bmatrix} v_{b1} \\ v_{b2} \\ \vdots \\ v_{bM} \end{bmatrix} = \begin{bmatrix} S_{11} & S_{12} & \cdots & S_{1M} \\ S_{21} & S_{22} & \cdots & S_{2M} \\ \vdots & \vdots & \ddots & \vdots \\ S_{M1} & S_{M2} & \cdots & S_{MM} \end{bmatrix} \begin{bmatrix} v_{a1} \\ v_{a2} \\ \vdots \\ v_{aM} \end{bmatrix} \tag{4.18}$$

where v_{bi} and v_{ai} are voltages of incident and reflected waves on the ith port. Thus, the voltages of the waves that goes into all ports can be expressed by:

$$\vec{v}_c = \vec{v}_a - \vec{v}_b = (I - S)\vec{v}_a \tag{4.19}$$

where $\vec{v}_c = [v_{c1}, v_{c2}, ..., v_{cM}]^H$, v_{ci} is the voltage of the wave that gets into ith port, $\vec{v}_a = [v_{a1}, v_{a2}, ..., v_{aM}]^H$, $\vec{v}_b = [v_{b1}, v_{b2}, ..., v_{bM}]^H$. $\vec{v}_a$ can be regarded as the original signals without mutual coupling and reflection, while $\vec{v}_b$ are the signals after reflection and mutual coupling. Thus, the coupled signals and the coupling-free signals are related by the mutual coupling matrix [41]:

$$C = I - S \tag{4.20}$$

This method has similar drawbacks to CMIM. According to the definition of scattering parameters, the antennas are excited by an active source connected to one of the antennas. Thus it fails to model a receiving array which is driven by external impinging sources. However, this method has an advantage that unlike mutual impedance, S parameter can be easily measured with a network analyzer.

Termination Mismatch

Another interesting approach is deliberately introducing impedance mismatch to the antennas [31]. The simulation showed in [31] that when a 500Ω load mismatches the antenna array, the influence of mutual coupling is much lower than when it's perfectly matched by 75Ω. The idea behind this is increasing the reflection such that the components from mutual coupling are overwhelmed. It's worth noticing that if the primary source of noise is from external, the SNR is not compromised since the noise power degrades in proportion to the signal.

However, in our case, the noise power primarily comes from the front end of receivers. Introducing mismatch would compromise the communication range. This is unacceptable because the communication range of Bluetooth LE is already limited.

Conclusion

We highlighted a few mutual coupling compensation techniques. We analyzed their feasibility and effectiveness. Self-calibration algorithms need the prior knowledge of the coupling matrix and claims adaptive to the change of environment. However, studies revealed that the oversimplified assumptions such as symmetric system structure and Toeplitz matrix structure make it fail with the presence of local scatterers.

Mutual impedance methods have two variations that are distinguished by their definition. CMIM is popular in antenna array calibration despite that the termination condition and Thevenin equivalent circuit model do not strictly hold true. RMIM has better performance than CMIM and does not add burden to computation and memory cost like the active antenna pattern methods do. However, the calculation involves complex modeling and simulation of the antenna and the nearby structure of the array setup.

S parameter method models the receiving array using the S parameter that is defined in transmitting mode, which produces an error. However, it is advantageous in that the measurement of the S parameter is straightforward with a network analyzer. In conclusion, the S parameter method is preferred.

4.2.2. Switch Leakage and Path Imbalance

A matrix models switch leakage and path imbalance in subsection 3.2.3. The matrix parameters can be incorporated into the self-calibration algorithm in the mutual coupling compensation context. Its structure is similar to the mutual coupling matrix. They are both complex, approximately Toeplitz and they both have off-diagonal elements that are much smaller than diagonal entries. However, incorporating an extra parameter to be estimated in the self-calibration algorithm requires more investigation such as the convergence check. This method is depreciated.

More accurately, we can obtain the parameter matrix by S parameter measurement using a network analyzer. Then add the matrix to array manifold by $A_L = LA$ as in equation 3.21. The RF switch that we used is $ZSWA4-63DR+$ solid state 4-port switch from Mini-Circuits. It has four RF ports to the antenna and one COM RF port to the receiver. This model has a wide operation band ranging from $1MHz$ to $6GHz$. The isolation level is $57dB$ at up to $2.7GHz$. The switching can be finished in $320ns$, and the highest switching frequency is $12.5kHz$.

The controlling of the switch is through a 9-pin D-Sub female connector. The pinout and the pin connection is in figure 4.2b and table 4.1. The supported states and the controlling logic can be seen in table 4.2. The female D-Sub connector was connected to a Teensey module [26] via a flat ribbon cable. The module is loaded with IMEC firmware with which we can issue commands from a computer to control the GPIO pins on the board via serial communication with the micro-USB connector. A Python script was written to handle the serial communication and issue command.

Before the measurement, it's worth noting that the parameters in the switch matrix suggested in equation 3.21 are not scattering parameters between two RF ports. Specifically, L_{ij} for $i \neq j$ stands for the isolation

---

[1] NC: Not Connected.

[2] Connecting one of pin 6-9 to GND is sufficient.

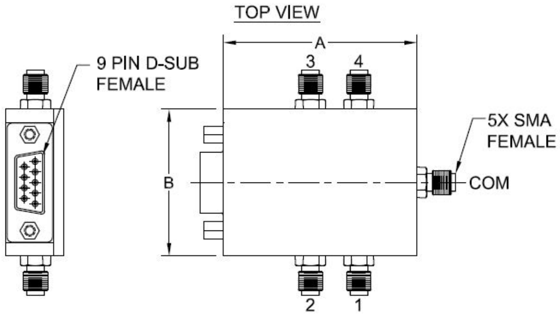

(a) Connector and Top View of RF Switch. Figure from data sheet of ZSWA4-63DR+

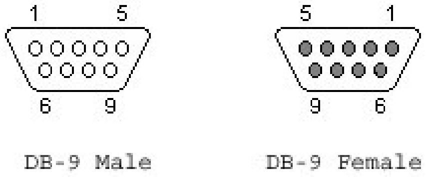

(b) 9-Pin D-Sub Connector Pinout

Figure 4.2: Sketch of RF Switch and D-Sub Pinout.

from RF port j to the COM port when RF port i is switched on, while L_{ii} stands for the ratio between the voltage that is output by COM port and the total voltage that is input in RF port i when it's switched on.

To include the effect of cable length, four SMA cables are attached. The network analyzer we used is an Agilent N5242A 4-port vector network analyzer (VNA). Since there are 5 ports on the switch in total, there is always one port that can not be analyzed. More than one round of measurement was conducted to cover all RF ports. A 50Ω terminator always terminated the RF port(s) that are not connected to the network analyzer because the internal impedance of RF ports is 50Ω.

An example of the switch parameter as a function of frequency is in figure 4.4 when port 4 is chosen. The blue line is the insertion loss of the on-port, yellow lines are reflections of all RF ports, and the gray lines are the isolation of the off-ports. A few conclusions can be drawn from the amplitude graph. First, the insertion loss is $-3dB$. Second, the switch ports are well-matched to the VNA cables. Third, the interference from the off-ports is negligible as the isolation levels are all below $-50dB$.

The insertion phase delays is a function of frequency as can be observed in figure 4.4b because with different frequency, the phase rotation changes within the same period. To avoid keeping a large switch compensation table for all possible frequencies in the memory, we can record the slope of the phase response of the ith port as the time delay Δt_i. Then, the phase delay can be obtained by:

$$\Delta\phi_i = 2\pi f_c \Delta t_i \tag{4.21}$$

As a result, the diagonal elements of switch matrix L defined in equation 3.20 is formed by $\{a_1 e^{-j\Delta\phi_1}$, $a_2 e^{-j\Delta\phi_2}$, ..., $a_M e^{-j\Delta\phi_M}\}$, where a_i here is the insertion loss in linear scale of the ith port. As for the off-diagonal elements, they are negligible since their magnitudes are below $-50dB$. Thus, the actual L matrix that we used is diagonal.

4.3. Using Multiple Antennas with One Receiver

The data model with antenna switching is derived in section 3.3. A CFO matrix O is derived to characterize the switching mechanism. Within the matrix, the only parameter that is unknown is the CFO. Thus, in this section, we propose a method for CFO estimation.

Pin Number	Function
1	NC [1]
2	V3
3	V2
4	V1
5	Vdd
6-9	GND [2]

Table 4.1: Pin Connection of the RF Switch

State	V3	V2	V1	RF COM-RF1	RF COM-RF2	RF COM-RF3	RF COM-RF4
1	Low	Low	Low	OFF	OFF	OFF	ON
2	Low	Low	High	ON	OFF	OFF	OFF
3	Low	High	Low	OFF	ON	OFF	OFF
4	Low	High	High	OFF	OFF	ON	OFF
5	High	Low	Low	OFF	OFF	OFF	ON
6	High	Low	High	All Off (disconnected state)			
7	High	High	Low	All Off (disconnected state)			
8	High	High	High	Unsupported			

Table 4.2: Controlling Logic of RF Switch

Figure 4.3: Teensey Module

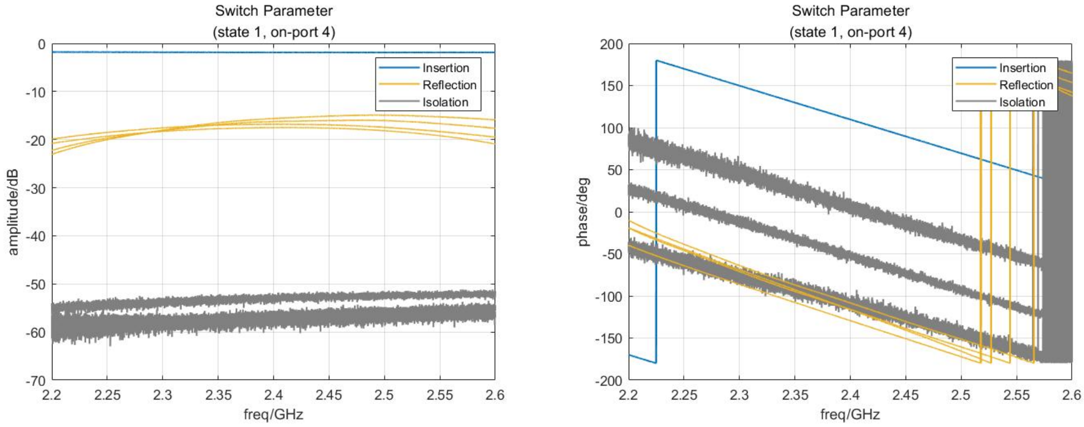

(a) Magnitude (b) Phase

Figure 4.4: Switch Parameters in state 1, when port 4 is switched on.

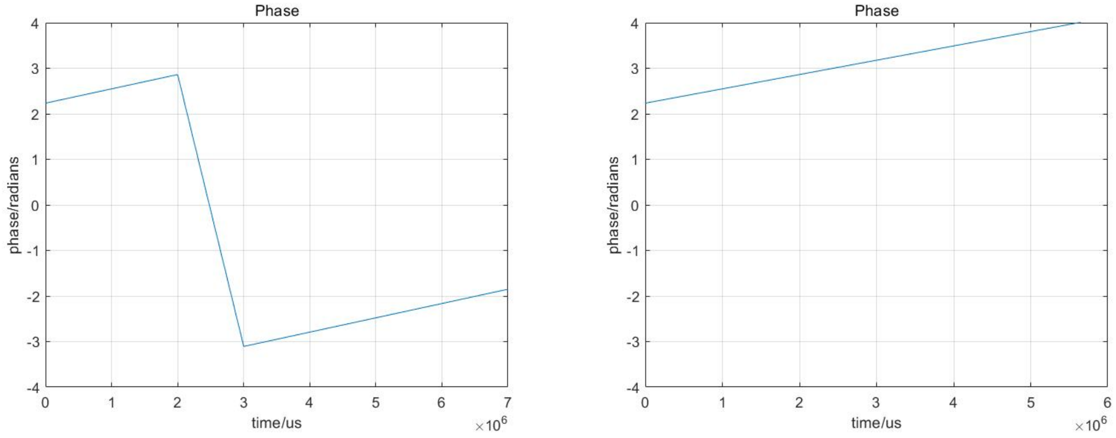

(a) Before compensation

(b) After compensation

Figure 4.5: Phase of reference perod samples before and after phase flipping compensation with 50kHz CFO.

4.3.1. CFO Estimation

Moose in [24] proposed a CFO estimation algorithm based on Maximum Likelihood (ML) estimator for OFDM systems. This method makes use of a sequence of symbols that can be divided into two identical halves. In OFDM systems, this sequence of symbols can be the preamble. The similar field that we can use is the reference period in the CTE as introduced in section 2.3.2. The reference period can be divided into two identical halves since the whole CTE is constant. It provides us with 8 samples in total sampled every $1\mu s$. Then, we can express the preamble in baseband as

$$s(t) = \begin{cases} s_1(t) & 0 \le t \le T \\ s_1(t-T) & T \le t \le 2T \end{cases} \tag{4.22}$$

where T is the time interval between two halves. Now we introduce CFO into the preamble. We assume the CFO is constant throughout the reception, and then the received preamble can be written as:

$$s(t) = \begin{cases} s_1(t)e^{j2\pi\Delta f_c t} & 0 \le t \le T \\ s_1(t-T)e^{j2\pi\Delta f_c (t-T)} & T \le t \le 2T \end{cases} \tag{4.23}$$

where Δf_c is the CFO. It's clear that the first and the second halves of the received preamble symbol have a fixed phase difference of $\Delta\omega T$ in sample wise when the additive noise is absent. The ML estimator derived in [24] is then:

$$\Delta\hat{f}_c = \frac{1}{2\pi T} tan^{-1} \frac{\sum_{n=0}^{N-1} Im[r_1^*(nT_s)r_2(nT_s)]}{\sum_{n=0}^{N-1} Re[r_1^*(nT_s)r_2(nT_s)]} \tag{4.24}$$

where $r_1(t)$ and $r_2(t)$ are first and second half of received signal $s(t)$ respectively, N is the number of samples in each half, T_s is the sample period, T is the duration of each half, $T = NT_s$. Note that the phase difference between two halves is calculated over time interval T. If the CFO is large enough such that the phase exceeds π, then the phase would flip by 2π. Then the estimation algorithm fails.

As a result, phase flipping compensation is necessary to ensure the capability of CFO estimation. With CFO's presence in the reference period, the phase shall increase or decrease monotonically. Based on this, we check the phase difference of successive samples. If we observe a phase difference that is more than π, then we think the phase is flipped. Then 2π is added or subtracted accordingly to the rest samples. See figure 4.5 for the effect of phase flipping and its compensation result. In figure 4.5a, after the sample at $2\mu s$, the phase exceeds π from the next sample at $3\mu s$. In equation 4.24 we use tan^{-1} function to obtain the phase angle, but tan^{-1} cannot distinguish angles that are outside $[-\pi, \pi]$. So the phase at $3\mu s$ drops to negative angle.

The drawback of using reference period only is that the number of available samples is limited, which makes the algorithm struggle when the SNR is low. To obtain more suitable samples, we can leverage the switching pattern design. Among the default switching patterns specified in IPS 1.1, Return-to-First can offer

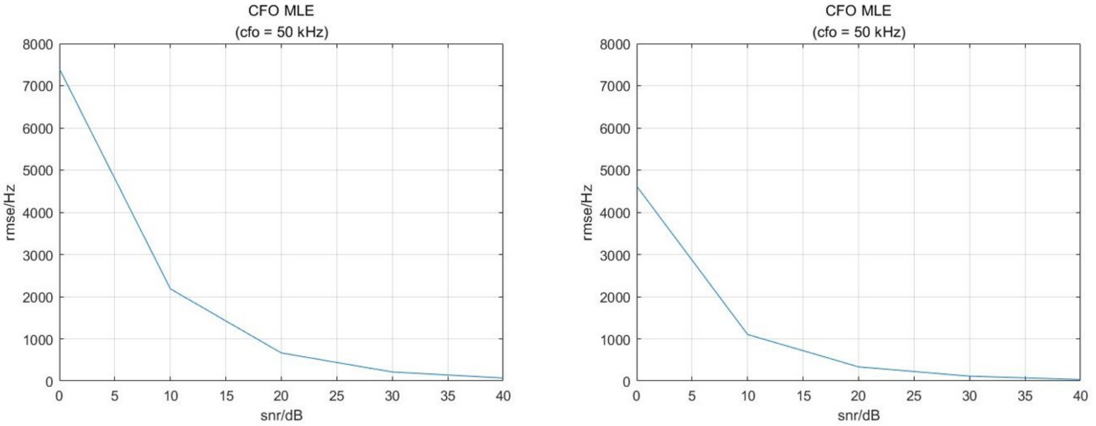

(a) With reference samples only.

(b) With extra samples from the $1st$ antenna in sampling slots

Figure 4.6: RMSE of CFO estimation vs SNR.

the feature of periodically repeated samples. The switch comes back to the first antenna on every two sample slots. Collecting all samples from antenna 1 gives us another 'preamble'. We applied ML estimator on two preambles separately and took the mean as the final estimation. Their performance in terms of RMSE against SNR are presented in figure 4.6. The definition of SNR here is the ratio between the signal power and the variance of the complex noise without taking bandwidth into consideration:

$$SNR = 10log_{10}\frac{\frac{1}{N}\sum_{i=1}^{N}|s[n]|^2}{\sigma_n^2}\ (dB) \tag{4.25}$$

where N is the number of samples in the signal $s[n]$, σ_n^2 is the variance of the complex noise.

The rationality of the SNR range chosen in the figures is proven as follows. In reality, receivers have a certain bandwidth even though the CTE is a pure DC signal. In our case we used a $200kHz$ low pass filter in the receiver processing chain and the sample rate of our simulation is $8MHz$. As a result, with this bandwidth into consideration, the SNR shall be $10log_{10}(40) = 16dB$ better than the SNR calculated by the definition in equation 4.25, making the SNR range to be $[16dB, 56dB]$. Now we compute the typical SNR in an BLE device. The noise figure F of a BLE receiver is typically $6dB$. Then the noise floor is calculated by:

$$NF_{dBm} = 10log_{10}(1000kT_0) + F + 10log_{10}BW \tag{4.26}$$

where $k = 1.38 \times 10^{-23}$ jourles per kelvin is the Boltzmann's constant, T_0 is the environment temperature in Kelvin, we choose 290 Kelvin corresponding to 20 Celsius. The noise floor with $200kHz$ bandwidth is then $-115dBm$. The reference sensitivity for a BLE receiver is $-70dBm$. Then the corresponding typical SNR is $-45dB$. Thus the choice of SNR range in the figures is reasonable.

Figure 4.6a is the RMSE versus SNR when utilizing only the samples from the reference period. Figure 4.6b is the RMSE versus SNR when not only utilizing the reference samples, but also using the samples of the $1st$ antenna from the sampling slots. We used Return-to-Fisrt switching pattern. We can observe that with the additional samples from sampling slots, the RMSE reduces substantially especially in low SNR.

The simulation of figure 4.6b was done with $2\mu s$ time slots and maximum $160\mu s$ CTE, thus giving us 18 samples from antenna 1. The time interval between these samples is $8\mu s$. Larger inter-sample intervals make the phase flip compensation fails earlier as CFO grows. When the phase difference between two successive samples is more than π, then it's impossible for us to tell whether a phase flip happens or not. The critical CFO at which the algorithm starts to fail is $\Delta\omega_c = \pi / T_s$. This effect makes CFO estimation fails at $500kHz$ and $62.5kHz$ when using reference only and using extra samples from antenna 1, as depicted in figure 4.7.

Practically, in the worst case, the error of an oscillator on a low-cost BLE device can be 40 ppm, corresponding to a CFO of roughly $96kHz$ at $2.4GHz$. It seems a problem since the algorithm fails after $62.5kHz$. However, direction finding is on the tail of the receiving chain in the receiver. Before we carry out angle estimation, the CFO shall be already compensated to a relatively low level such that both the CFO estimation techniques can both be utilized safely to refine the CFO estimation.

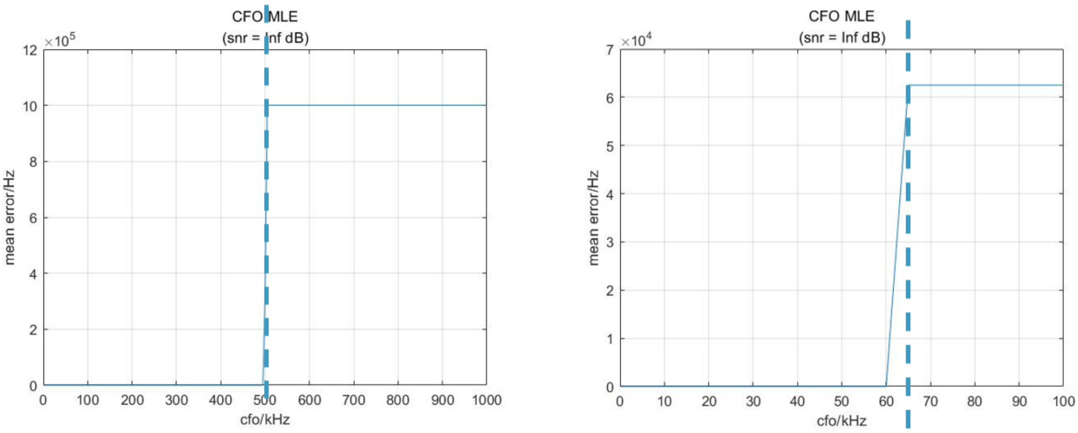

(a) Use reference only

(b) With extra samples from antenna 1

Figure 4.7: RMSE of CFO estimation against CFO. (SNR=inf dB)

.

4.3.2. Usage of CFO Matrix

In section 4.1, data vector $\vec{x}$ and data matrix X are based on the simultaneous sampling over all antennas. The usage of antenna switching used in the project, however, makes the samples from antennas not align in time. As discussed in section 3.3, a CFO matrix is derived to relate the data model with sequential sampling and the one with simultaneous sampling. As the MUSIC algorithm takes the data matrix obtained by simultaneous sampling as the input, we need to adapt to make our data model compatible.

The first way is including the CFO matrix into the array response matrix A by:

$$A' = OA \tag{4.27}$$

Then the modified array response is used in equation 4.7. Thus out data matrix X_{ss} with sequential sampling can be directly used as the input of the MUSIC algorithm.

The second way is essentially equivalent to the first way. We can cancel the CFO term in equation $X_{ss} = OX$ by

$$\hat{X} = O^{-1} X_{ss} \tag{4.28}$$

then input $\hat{X}$ to the MUSIC algorithm. In our case, we used the latter method.

4.4. Spatial Smoothing for Coherent Signals

As discussed in 4.1, MUSIC algorithm fails when the received signals are coherent. More specifically, if d coherent signals impinges to an antenna array with M elements, then the signals can be expressed by a common signal $s_0[n]$ multiplied by different scalar factors as: $s_i[n] = a_i s_0[n]$. Then the received data vector can be written as:

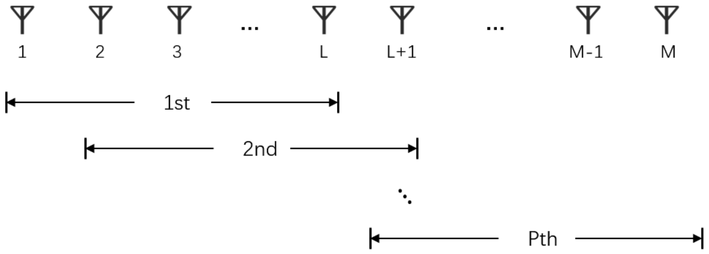

Figure 4.8: Subarray Division of Spatial Smoothing

$$\begin{aligned}
\vec{x} &= \begin{bmatrix} \vec{a}(\theta_1) & \vec{a}(\theta_2) & \cdots & \vec{a}(\theta_d) \end{bmatrix} \begin{bmatrix} s_1 \\ s_2 \\ \vdots \\ s_d \end{bmatrix} + \vec{n} \\
&= \begin{bmatrix} \vec{a}(\theta_1) & \vec{a}(\theta_2) & \cdots & \vec{a}(\theta_d) \end{bmatrix} \begin{bmatrix} a_1 s_0 \\ a_2 s_0 \\ \vdots \\ a_d s_0 \end{bmatrix} + \vec{n} \\
&= \begin{bmatrix} a_1 \vec{a}(\theta_1) + a_2 \vec{a}(\theta_2) + \cdots + a_d \vec{a}(\theta_d) \end{bmatrix} s_0 + \vec{n}
\end{aligned} \tag{4.29}$$

As a result, the steering vectors is linearly combined into a single vector which is not a legitimate steering vector anymore. To tackle this problem, in this section, a technique called Spatial Smoothing (SS) and its improvement - Forward and Backward Spatial Smoothing (FBSS) - will be introduced and the choice of subarray size will be analyzed.

4.4.1. Spatial Smoothing

Spatial Smoothing as proposed by Evans *et al.* [7] is the most promising solution to the coherent signal problem. [45] The idea behind is quite simple. A uniform linear array consisting of M antennas is considered. Let this array be divided into overlapping subarrays of size L. For instance, antenna $\{1,2,...,L\}$ forms the first subarray, and antenna $\{2,3,...,L+1\}$ forms the second subarray, and etc. (see figure 4.8). then, the number of subarray P is $M-L+1$. Then, following the same notation in equation 3.9, the data matrix belonging to the kth subarray is:

$$X_k = A_L D^{(k-1)} S + N \tag{4.30}$$

where A_L is the array response matrix for L antenna elements, D is a diagonal matrix whose diagonal is $[e^{j2\pi \frac{d}{\lambda} cos\theta_1}, e^{j2\pi \frac{d}{\lambda} cos\theta_2}, ..., e^{j2\pi \frac{d}{\lambda} cos\theta_q}]$, q is number of sources. The sample covariance matrix associated with this data matrix is:

$$\hat{R}_{x_k} = A_L D^{(k-1)} \hat{R}_s D^{(k-1)H} A_L^H + \sigma^2 I \tag{4.31}$$

The spatially smoothed covariance matrix is defined to be the sample mean of subarray covariances:

$$\bar{R}_x = \frac{1}{P} \sum_{k=1}^{P} \hat{R}_{x_k} \tag{4.32}$$

The ability to resolve coherent signals comes at a price. Intuitively it's true since the effective aperture is reduced to L. Shan in [35] proved that as long as $P \geq d$, where d is the number of coherent signals, the signal covariance matrix will be nonsingular no matter the coherency of signals. As a result, the total number

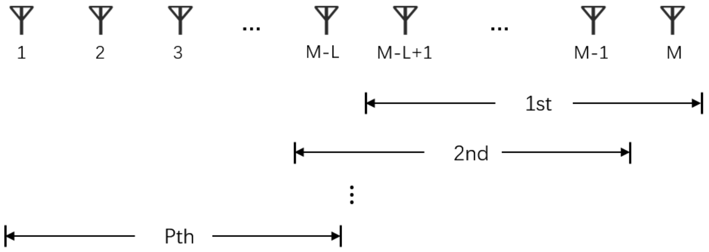

Figure 4.9: Backward Subarray Division of Forward/Backward Spatial Smoothing

of elements M has to be at least $L + d - 1$. Because of the size of subarrays, the dimension of eigenspace is reduced to L, which has to be higher than the dimension of signal space. As a result, the size of the subarrays has to be at least $d + 1$. As a conclusion, the total number of elements required is then $M \geq 2d$.

Note that the data model in equation 4.31 requires the antenna array to be shift-invariant, which means the array response matrix shall have the so-called Vandermonde structure. This requirement is explained as follows. The transpose of a $d \times M$ Vandermonde matrix with the terms of a geometric progression in each of its rows can be written as:

$$V_t = V^T = \begin{bmatrix} 1 & 1 & \cdots & 1 \\ \alpha_1 & \alpha_2 & \cdots & \alpha_d \\ \alpha_1^2 & \alpha_2^2 & \cdots & \alpha_d^2 \\ \vdots & \vdots & \ddots & \vdots \\ \alpha_1^M & \alpha_2^M & \cdots & \alpha_d^M \end{bmatrix} \tag{4.33}$$

With this structure, any group of L adjacent rows can be expressed by the first L rows and a diagonal matrix by:

$$V_{tk} = \begin{bmatrix} \alpha_1^{k-1} & \alpha_2^{k-1} & \cdots & \alpha_d^{k-1} \\ \alpha_1^k & \alpha_2^k & \cdots & \alpha_d^k \\ \vdots & \vdots & \ddots & \vdots \\ \alpha_1^{k+L-2} & \alpha_2^{k+L-2} & \cdots & \alpha_d^{k+L-2} \end{bmatrix} = \begin{bmatrix} 1 & 1 & \cdots & 1 \\ \alpha_1 & \alpha_2 & \cdots & \alpha_d \\ \vdots & \vdots & \ddots & \vdots \\ \alpha_1^L & \alpha_2^L & \cdots & \alpha_d^L \end{bmatrix} diag\left\{\alpha_1\ \alpha_2\ ...\alpha_d\right\} = V_{tL} D_V \tag{4.34}$$

By comparing equation 4.34, and 4.31, V_{tL} corresponds to A_L, D_V corresponds to D, thus we can conclude that in order to use spatial smoothing, the whole antenna response matrix has to follow the same structure as 4.33. Now recall the array response vector for our ULA in equation 3.9, ULA is eligible for using spatial smoothing technique because its array response matrix satisfies Vandermonde structure. The same requirement applies for the Forward/Backward Spatial Smoothing.

4.4.2. Forward/Backward Spatial Smoothing

To overcome the drawback of reduced aperture, additional P subarrays are added in addition to the subarrays introduced by SS. [25] [45] A set of backward subarrays are defined by grouping antenna $\{M, M-1, ..., M-L+1\}$ as the first backward subarray, etc. (see 4.9).

Then the spatially smoothed covariance matrix in this case is:

$$\bar{R}_x = \frac{\bar{R}_x^f + \bar{R}_x^b}{2} \tag{4.35}$$

where $\bar{R}_x^f$ and $\bar{R}_x^b$ are forward and backward covariance matrices. The forward covariance matrix $\bar{R}_x^f$ is calculated using equation 4.32. The backward covariance matrix $\bar{R}_x^b$ is calculated using the same principle as in equation 4.32 but with reversed subarrays:

$$\bar{R}_x^b = \frac{1}{P}\sum_{k=1}^{P} \hat{R}_{x_k}^b \tag{4.36}$$

$$\hat{R}_{x_k}^b = J\hat{R}_{x_k}^* J \tag{4.37}$$

where $*$ denotes complex conjugate and J is the exchange matrix:

$$J := \begin{bmatrix} 0 & 0 & \cdots & 0 & 1 \\ 0 & 0 & \cdots & 1 & 0 \\ \vdots & \vdots & \iddots & \vdots & \vdots \\ 0 & 1 & \cdots & 0 & 0 \\ 1 & 0 & \cdots & 0 & 0 \end{bmatrix} \tag{4.38}$$

The minimum number of total elements required is improved to $3d/2$ [25].

4.4.3. Optimal Subarray Size

About the minimum times of smoothing needed to completely de-correlate the sources, studies are done by Chen and Liu in [5]. They proved from two perspectives that the minimum number of smoothing required to make the correlation coefficient between two signals to approach zero is:

$$P_{min} = \frac{\lambda}{d(sin\theta_i - sin\theta_j)} \tag{4.39}$$

where λ is operation wavelength, d here indicates the inter-element spacing in the array, θ_i is the AoA of the ith source with respect to antenna norm. When two signals are closely separated,

$$P_{min} \approx \frac{\lambda}{d(\theta_i - \theta_j)cos\theta_i} \tag{4.40}$$

This formula gives us insight into the behavior of spatial smoothing. This formula suggests that more subarrays would be necessary when signals are more closely spaced, which matches the intuition. We can also observe from the formula that the smaller the inter-element spacing is, the more subarrays would be needed. This also makes good sense since further spatial separation implies less correlation of the wireless channels. Finally, from formula 4.40, if the signals are from end-fire directions (which is close to the direction of the array baseline), the number of necessary subarrays would rise.

In practice, in an indoor multipath environment at around $2.4GHz$, the number of multipath rays could be up to several dozens [32][27]. In another word, the number of the coherent signals is always larger than the antenna element number, which makes formula 4.39 and 4.40 less interesting. However, measurements suggest that the indoor multipath components tend to group in clusters in each of which includes components with similar delay and AoA [32]. For instance, a multipath channel model generated by a ray tracer including up to $3rd$ order reflections are presented in figure 4.10. The reflections include those from the ceiling and floor. The environment is a rectangular meeting room without furniture, which is sketched in figure 3.2.

It is extremely hard and costly to resolve every single path within each cluster. But since the AoAs within a cluster are concentrated in a tiny range, finding the AoAs of clusters could give us close estimation for each path. According to formula 4.39, the more subarrays there are, the better chance there will be to resolve the clusters that are closely separated. But in the meanwhile, because of the limitation of physical array size, the total amount of element M is limited. As a result, more subarray would lead to smaller subarray size, which in return limits the number of resolvable clusters.

In this thesis, we chose to let the inter-element spacing to be half-wavelength of $2.4GHz$, which is $62.5mm$. An 8-element antenna array was considered which already has an aperture of $43.75cm$. Another more commercially interesting configuration is the 4-element array because of its relatively small physical size. With the fixed antenna size, increasing P would result in an increased performance since the rank of signal covariance is increased. However, when P are increased to a certain extent when the signal covariance matrix achieves its maximum rank, the MUSIC would not benefit from increasing P. In contrast, continue increasing P makes the subarray size L shrinks, such that the performance would degrade afterward.

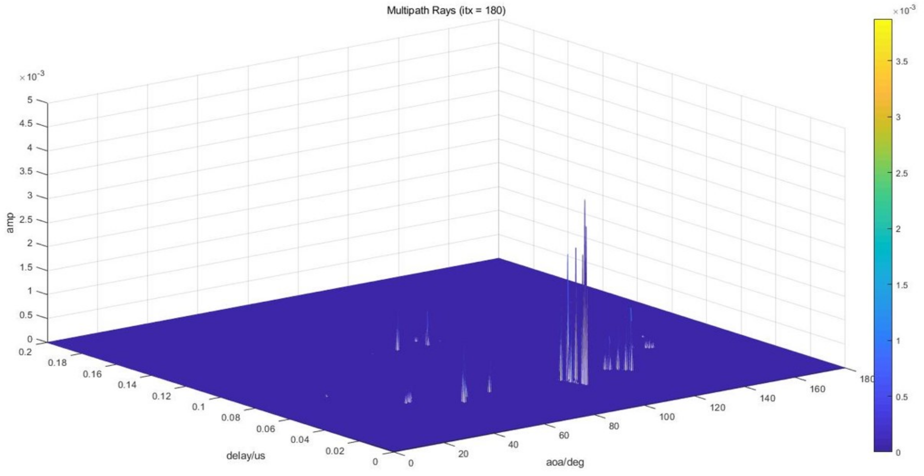

Figure 4.10: Multipath Component Clusters

In conclusion, there is a trade-off when choosing the number of subarrays P. Thus we usually choose an intermediate subarray number (2 or 4 for 8-element ULA, and 2 for 4-element ULA). No in-depth mathematical and experimental analysis is done within the context of this thesis.

4.5. LOS Identification

Incorporating array calibration, FBSS, and MUSIC algorithm that are discussed above would give us an estimation of each path's AoA. But for indoor localization, the AoAs of multipath components other than LOS is of no interest since they do not indicate the relative bearing of the peer device. Among all AoA estimations, identifying the LOS direction is another topic we need to tackle.

To identify the LOS, we need to extract the feature(s) that distinguish(es) the LOS component to the others. One noticeable feature is that LOS experience the least amount of time delay since the direct link between the transmitting device and the receiving device is the shortest. The second feature is a result of smallest time delay. The LOS attenuates the least among all multipath components, meaning it has the most power when it arrives at the receiver. We will first describe the joint angle and delay estimation and its problem in our application. Next two methods will be proposed based on the power information.

4.5.1. Joint Angle and Delay Estimation

One of the early yet important investigations of joint angle and delay estimation is JADE developed by Michaela Vanderveen $et\ al.$ in [43]. Similarly to ours, it models the received data vector experiencing the multipath fading with d rays by an M-element array as:

$$\vec{x}(t) = \sum_{k=1}^{d} \vec{a}(\theta_k)\beta_k(t)r(t-\tau_k) + \vec{n}(t) \tag{4.41}$$

where $\beta_k(t)$ is the complex envelope of $k-th$ path fading, τ_k is the delay in time of $k-th$ path, and $r(t) = \sum_i b(i)g(t-iT)$ is the transmitted signal, given that $b(i)$ is the ith symbol, and $g(t)$ is the modulation waveform. It's assumed during the period in consideration, the channel is stationary, such that both β_ks and τ_ks are constant. Sampling the data vector at symbol rate gives the model in terms of channel effect and transmitted symbols:

$$\vec{x}[k] = H\vec{s}[k] + \vec{n}[k] \tag{4.42}$$

P samples covering the transmitted signal duration and the maximum excess delay are taken. H is the matrix including the information of all M channels and modulation effects by

$$H = \begin{bmatrix} \vec{a}(\theta_1) & \vec{a}(\theta_2) & \cdots & \vec{a}(\theta_d) \end{bmatrix} \begin{bmatrix} \beta_1 & & \\ & \ddots & \\ & & \beta_d \end{bmatrix} \begin{bmatrix} \vec{g}^T(\tau_1) \\ \vdots \\ \vec{g}^T(\tau_d) \end{bmatrix} \tag{4.43}$$

where $\vec{g}(\tau_i)$ is a column vector containing samples of $g(t-\tau_i)$. The matrix H is then vectorized to be an MP long by taking the transpose of each row of H, and stacking them below the transpose of the previous one:

$$\vec{h} = U(\vec{\theta}, \vec{\tau})\vec{\beta} \tag{4.44}$$

where ith column of $U(\vec{\theta}\vec{\tau})$ is $\vec{a}(\theta_i) \otimes g(\tau_i)$, $\otimes$ stands for Kronecker product. Then, a minimization problem which is related to a channel information matrix is formulated based on Maximum Likelihood estimator:

$$\min_{\vec{\theta},\vec{\tau},B} \| Y - U(\vec{\theta}, \vec{\tau})B\|_F^2 \tag{4.45}$$

m time slots are used and the impulse response of each time slot is stacked as the columns of $MP \times m$ matrix Y. The similar formulation is formed on B with each column being $\vec{\beta}$. Due to the channel stationarity assumption, the columns of Y should be about the same with the absence of noise. The columns of B should also be about the same without noise.

Despite the multi-dimensional searching introducing computational burden, there's a clear aspect making it impractical for our BLE scenario, which is that the channel has to be estimated first. In a typical working area, the maximum excess path delay is up to several hundred nanoseconds. However, in BLE direction finding, the maximum sampling rate is defined to be $1MHz$ when it's in the reference period. In this case, the channel impulse response cannot be estimated. Another JADE algorithm in [43] solved the multi-dimensional search problem, but also raises the requirement of channel response estimation.

Another reason for the impracticality of JADE in [43] is that it makes use of the phase response of the channel. We can indeed use multiple packets at different frequencies to widen our bandwidth to give an estimation of the phase response. But for BLE transmitters, the initial phase of the transmitted signal is not constant when switching to another transmission frequency. Thus a single-direction communication cannot enable us to estimate the phase response.

4.5.2. Proposed Power-Based LOS Identification

Since the channel information-related JADE is inapplicable due to the lack of temporal resolution in BLE, we proposed a method for identifying the LOS direction by making use of the power signature in the eigenspace. The algorithm is named as MUSIC LOS-Id. Ideally, the LOS path has the least amount of time delay, plus it is reflection free, it would have the most energy preserved when it arrives at the receiver. If we could find an estimated direction where the received power is the most concentrated, then we can obtain an estimate of LOS.

We start by recapping the eigenvalue analysis of the data covariance matrix. We split the eigenvector matrix into two halves corresponding to signal space and noise space respectively. So the eigenvalue decomposition of data covariance matrix can be written as:

$$\begin{aligned} R_x &= U\Lambda U^H \\ &= \begin{bmatrix} U_s & U_n \end{bmatrix} \begin{bmatrix} \Lambda_s + \sigma^2 I_d & 0 \\ 0 & \sigma^2 I_{M-d} \end{bmatrix} \begin{bmatrix} U_s^H \\ U_n^H \end{bmatrix} \end{aligned} \tag{4.46}$$

The physical meaning of eigenvectors can be interpreted as follows. The eigenvectors are a set of orthogonal directions with which the subspace of R_x is decomposed. Note that the subspace spanned by columns of R_x is the same as A's if noise is not present. These orthogonal directions are sorted according to their dominance in space, which is related to the corresponding eigenvalues. As a result, the first eigenvector points to the direction in space which influences R_x the most. Specifically, if the first eigenvector $\vec{u}_1$ is used as a beamformer, then the output power of the beamforming is

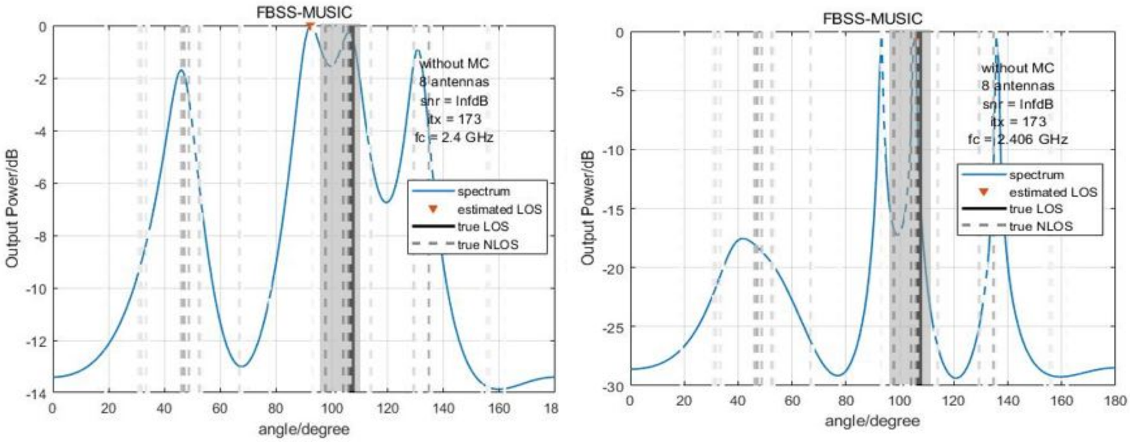

(a) $f_c = 2.4GHz$ (b) $f_c = 2.406GHz$

Figure 4.11: MUSIC spectrum at two different frequencies

$$\begin{aligned} P &= \frac{1}{N}\vec{u}_1^H X(\vec{u}_1^H X)^H \\ &= \vec{u}_1^H R_x \vec{u}_1 \\ &= \lambda_1 \end{aligned} \tag{4.47}$$

This can be generalized to any eigenvector. As a result, the eigenvalues indicates the power that is received in the direction specified by the corresponding eigenvector. Then, the first eigenvector of the data covariance matrix always implies in space where the most power is coming from. Based on this observation, we propose the following algorithm for LOS identification.

The algorithm consists of three steps:

1 First apply MUSIC with FBSS to give a set of initial estimate of AoAs $\hat{\Theta} = \left[\hat{\theta}_1, \hat{\theta}_2, \cdots, \hat{\theta}_p\right]$, where p is the amount of resolved peaks.

2 Then form array response vectors $\vec{a}(\hat{\theta}_i)$ for $i = 1, ..., q$.

3 Find the $\hat{\theta}_i$ that maximizes the following cost function as the estimate of LOS direction:

$$\mid \vec{a}(\hat{\theta}_i)^H \vec{u}_1 \mid \tag{4.48}$$

The result of equation 4.48 shows the closeness in terms of direction of two vectors, since all $\vec{a}(\theta_i)$ have the same norm and $\vec{u}_1$ is normalized.

Analysis

The drawback of this method comes from the clustering of multipath components. The physical size of the array limits the aperture, thus limits the resolution. The lack of angular resolution means the initial estimates $\{\theta_i\}$ are AoAs of clusters in most of the cases. Inside each cluster, multipath components may constructively or destructively interfere with each other such that the total power is diminished, even though a strong LOS path is present.

See figure 4.11. The MUSIC spectrum is drawn for two different center frequencies - $2.4GHz$ and $2.406GHz$ without noise. The vertical solid line indicates the true LOS direction, while the vertical dotted lines are true AoAs of NLOS paths. The shade of the vertical lines shows the relative power. The darker the line, the stronger the power. The red triangle indicates the estimated LOS direction. The multipath channel is modeled using the ray tracer. In both cases, the peaks at around 110° are resolved, but at $2.4GHz$, the LOS is falsely detected.

If we take a closer look at the signals that are coming within a small range around LOS (as indicated by the gray shade in 4.11), we can observe the signal of destructive interference. Figure 4.12 shows the absolute value, the real part and imaginary part of individual received complex baseband signals at antenna 4 in an

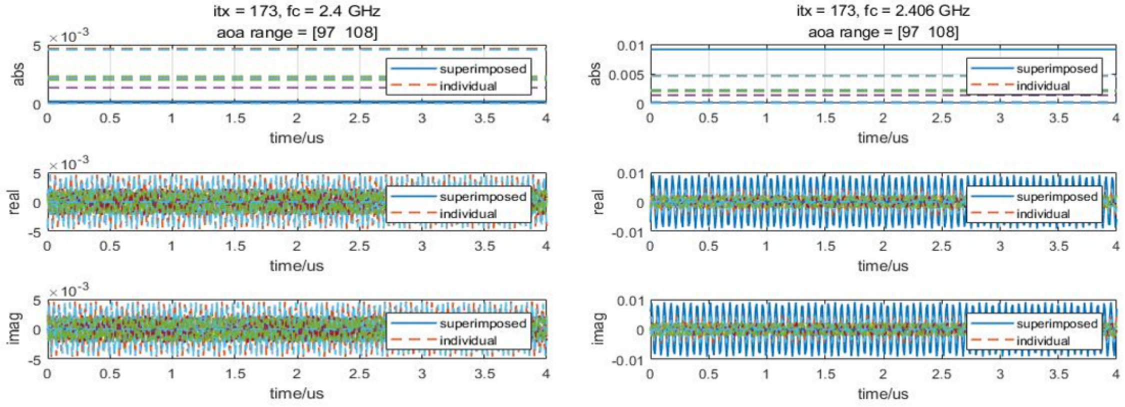

(a) $f_c = 2.4GHz$ (b) $f_c = 2.406GHz$

Figure 4.12: Received signal superimposition

8-element ULA. The solid blue curves are the superimposed version of those individual components. At $2.4GHz$, the combined signal nearly vanishes while at $2.406GHz$, the combined signal is amplified. The different result of multipath superimposition is because, at a different frequency, the phase rotation during the same time period is different. This results in different phase relations between multipath rays.

4.5.3. Proposed CLEAN based LOS Identification

The analysis for the MUSIC LOS-Id algorithm above reveals the incapability of resolving within the clusters sometimes leads to the failure of LOS estimation. Starting from this a CLEAN based algorithm is proposed to overcome this problem. The algorithm then is named as CLEAN-MUSIC LOS-Id.

The CLEAN algorithm was firstly published in [14] for subtracting the brightest point in a sky map collected by radio astronomy. This idea was brought to the content of direction finding in [41] for a semi-nonuniform linear array (NLA) with coherent sources. The authors claim in [41] that this method has no superior improvement to FBSS for a ULA because FBSS already performs well. A large number of multipath components in indoor environments and the necessity to find the LOS component require a better performing algorithm than FBSS, so we modified the CLEAN algorithm based on [41].

The idea is that increasing the resolution inside a cluster by leaving only the multipath components within that cluster in the data matrix. The proposed algorithm is carried out in an iterative manner:

1 Apply MUSIC with FBSS to obtain a set of initial estimates of AoAs $\hat{\Theta} = \left[\hat{\theta}_1, \hat{\theta}_2, \cdots, \hat{\theta}_p\right]$, where p is the amount of resolved peaks.

2 Construct array response matrix A using $\hat{\Theta}$, then recover the source matrix by

$$\hat{S} = \left(A(\hat{\Theta})^H A(\hat{\Theta})\right)^{-1} A(\hat{\Theta})^H X \tag{4.49}$$

3 For each $\hat{\theta}_i$ (in an arbitrary order), do following:

   a Construct $A'(\hat{\Theta})$ by deleting ith column in $A(\hat{\Theta})$, and construct $\hat{S}'$ by deleting ith row of $\hat{S}$.

   b Subtract the part in data matrix due to clusters other than ith cluster by

$$X' = X - A'\hat{S}' \tag{4.50}$$

   c Do FBSS-MUSIC again on X' to resolve more multipath.

   d Add the new estimated angles to $\hat{\Theta}$

4 Repeat step 2-3 until no more new multipaths can be resolved.

5 For each $\hat{\theta}_i$, subtract the other rays by the same method as in step 2 to 3-b to obtain a new cleaned data matrix X_i'. Then find the $\hat{\theta}_i$ that maximizes

$$\frac{1}{N}\vec{a}^H(\hat{\theta}_i)X_i'X_i'^H\vec{a}(\hat{\theta}_i) = \vec{a}^H(\hat{\theta}_i)R_{xi}\vec{a}(\hat{\theta}_i) \tag{4.51}$$

which is the output power of a beamformer, as the estimate of LOS direction.

Analysis

This method uses the same principle of cleaning the data matrix in step $3-b$ as in [41]. The stability analysis is done in that literature. In the same literature, experiments are done to verify the effectiveness of their algorithm. Results show that using a 6-element NLA, the algorithm can resolve precisely two closely separated correlated signals coming at 75° and 80°.

The intention of the algorithm in [41] was for refining the estimation of FBSS-MUSIC. The lack of ULA aperture in a semi-NLA keeps FBSS from giving satisfying enough accuracy. However, FBSS is well capable of resolving all peaks for a limited number of coherent signals that are considered in the experiment. That makes the signal matrix estimation in step 2 reasonably reliable. In our case, however, the initial estimates of FBSS-MUSIC generally only gives the estimates for the clusters without having the resolution of the components inside the clusters. Thus the resolved angles are only a subset of all multipath component AoAs. This makes the constructed A in step 2 have much less dimension than the real one. An error is introduced in step 2 because of this.

Moreover, several coherent signals may lie within the vicinity of each angle in $\hat{\Theta}$. As a result, subtraction in step 3-b almost definitely would leave coherent residuals in the cleaned data matrix. For blocking out the coherent residuals from the unwanted clusters, techniques have to propose in the future work. One hypothesis is that looking for an eigenvalue threshold for step 3-c for determining the signal space of the wanted cluster.

Finally, an obvious drawback of our proposed algorithm is the computational complexity. Within each iteration, p times more operations of MUSIC shall be done compared to MUSIC LOS-Id. From the experiences in simulation, the number of iterations required to obtain a satisfying result is less than 4. More operations of MUSIC may also make the algorithm more sensitive to array mis-modeling.

4.5.4. Multi-Tone Technique

As concluded in 4.5.2, the primary factor restricting the LOS-Id accuracy is the unpredictable destructive interference among multipath component at receiver. This effect is frequency sensitive. A slight frequency shift of a few MHz could result in a significant difference of received energy, as demonstrated in figure 4.12. Based on this knowledge, and combining the frequency hopping character of BLE, a multi-tone technique can be adopted to overcome the destructive interference effect.

BLE uses frequency hopping among 40 physical channels in $2.4GHz$ ISM band with $2MHz$ inter-channel spacing. The hopping rate is 1600 $hops/s$ as a standard, which can well accommodate a CTE supplemented packet. What we can do is commanding the transmitting device to consecutively transmit a packet burst containing several packets that are carried by different frequencies within a short time interval. Then combine the CTEs from these packets in the receiver before conducting direction finding. The combined data matrix then becomes:

$$X = \begin{bmatrix} X_1 & \cdots & X_m \end{bmatrix} \tag{4.52}$$

where data matrix with subscript X_i is the data matrix taken from ith packet whose carrier frequency is f_{ci}, m is the number of packets used in the direction finding estimation. This technique is also referred to as Packet Aggregation (PA). When doing direction finding, the whole matrix X is used as an input, meaning using the same array response vectors for all frequency. This shall not pose a problem. The frequency band of BLE is $2.402-2.48GHz$. The wavelength difference between the starting an ending frequency in the band is mere $0.004m$, which is negligible. This leaves array response vector defined in section 3.9 approximately unchanged even though the frequency is changed.

The advantage of PA is twofold. First, it reduces the chance that the LOS signal is canceled out by neighboring multipath components, which reduces difficulty to our power based LOS-Id algorithm. Second, aggregating more packets means more snapshots. This makes the covariance matrix approximation in 4.1 more accurate.

The limitation of PA, of course, is related to channel coherence time. The packet burst enlarges the observation period. If during the observation period the channel is changed, then the array vectors belonging to the latter packets can be different than the previous ones'. But, the channel coherence time is related to Doppler spread in [1] by:

$$T_c \approx \frac{1}{f_d} \tag{4.53}$$

where f_d is the Doppler frequency spread given by $f_d = \frac{v}{c} f_c$, v is radial speed. If an object is moving at $2m/s$ along the radial direction, which is already quick in a typical indoor working environment, the Doppler spread is $16Hz$. Thus the channel coherence time is $62.5ms$, which is much longer than a BLE link layer packet. As a result, we can feel safe to use multi-tone without worrying about the change of channel.

Another Interpretation

We can interpret the effect of the multi-tone technique from another perspective. Consider again the combined data matrix in equation 4.52. Then we compute the data covariance matrix:

$$\begin{aligned} R_x &= \frac{1}{mN} X X^H \\ &= \frac{1}{mN} \begin{bmatrix} X_1 & \cdots & X_m \end{bmatrix} \begin{bmatrix} X_1^H \\ \vdots \\ X_m^H \end{bmatrix} \\ &= \frac{1}{mN} \sum_{i=1}^{m} X_i X_i^H \\ &= \frac{1}{m} \sum_{i=1}^{m} R_{x_i} \end{aligned} \tag{4.54}$$

As a result, essentially the multi-tone technique obtains the pre-processed data covariance matrix by takes the sample mean of data matrices from every packet. This is the same idea as spatial smoothing, but here we use different packets carried by different frequencies rather than different subarrays. Thus, this technique can also be regarded as a frequency smoothing (FS) technique.

4.6. Conclusion

During this chapter, the techniques for LOS direction finding under the framework of Bluetooth LE are presented. The super-resolution DF algorithm MUSIC is used as a basis algorithm. Various techniques for modeling the MC and switch imbalance are compared. Eventually, we chose to use S parameter method to compensate mutual coupling, and to use VNA measurement to calibrate the switch and cable. We also employ a classical ML estimator on the reference period and the repetitive switching pattern of CTE to estimate CFO to make our sequentially sampled data vector to be compatible to the MUSIC algorithm. Next, FBSS is adopted to tackle the coherent signal problem. Finally, two algorithms are proposed to find the LOS direction. Among the two proposed algorithms, the CLEAN-MUSIC LOS-Id is less interesting because of its computational complexity. Moreover, more work needs to be done to make CLEAN-MUSIC work more efficiently with coherent residuals.

5

BLE Direction Finding Simulator, and Simulation Results

The algorithms derived in the preceding chapters are verified in this chapter. The means of verification includes Monte-Carlo simulations using ray tracer simulated channel model with simulated physical imperfections, as well as a set of measurement campaign that was conducted to obtain a real channel model, which will be presented in the next chapter. Then the derived algorithms are applied, a few analysis and conclusions follow in the end.

Note that we have the freedom to choose a switching pattern. In this thesis, simulations are done with the Return-to-First pattern, unless explicitly specified otherwise. The choice and effects of switching pattern are out of the scope of the thesis.

5.1. BLE Direction Finding Simulator

The simulator is based on Bluetooth LE 1M PHY. It simulates transmitter effects such as modulation, multipath channel effect, and receiver effects such as noise, antenna array response, mutual coupling, CFO and switches imperfection. The transmitter is modeled to be equipped with a single half-wavelength dipole antenna, while the receiver is modeled to be a ULA with 4 or 8 half-wavelength dipole elements. The whole processing chain are simulated on baseband at a constant sampling frequency of $8MHz$ since GHz level frequency requires too high sampling rate, thus is computation costly.

5.1.1. Transmitter

A typical transmitter model of a BLE device is shown in figure 5.1. A stream of binary symbols $m_i \in \{1,-1\}$ are generated from the transmitter at a symbol rate of 1 $Msymbols/s$, corresponding to a bit rate of 1 Mb/s. We only consider the CTE field. Thus the symbols are all 1s. Besides, we used the $2\mu s$ CTE slot. The CTE duration used here is $160\mu s$, giving the maximum number of samples.

The symbols first are passed to a pulse shaping filter. The pulse generated in this step is a rectangular

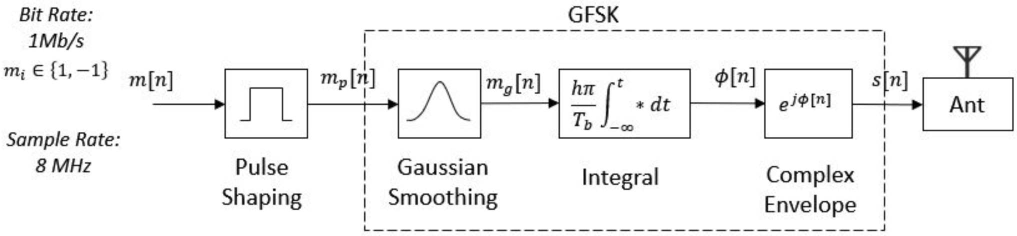

Figure 5.1: Bluetooth LE 1M PHY Transmitter Model

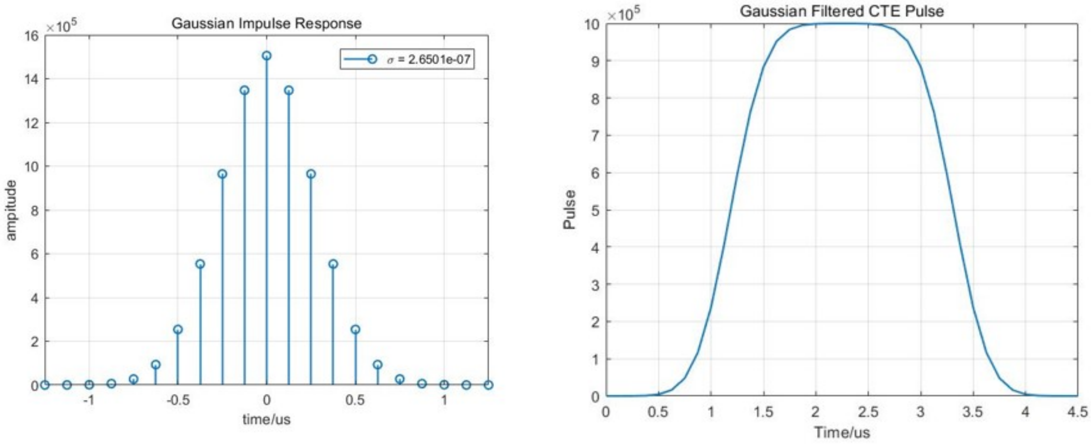

(a) Gaussian filter impulse response

(b) A Gaussian filtered CTE pulse

Figure 5.2: Gaussian filter impulse response and a filtered CTE pulse

waveform with $1\mu s$ duration. The Bluetooth LE adopts the GFSK modulation technique. A normal procedure for generating a GFSK signal is first smoothing the rectangular pulse shaped signal by a Gaussian filter. The impulse response of the Gaussian filter is:

$$h_g[n] = \begin{cases} \frac{1}{\sqrt{2\pi}\sigma} e^{\frac{1}{2}\left(\frac{n-5\sigma/T_s}{\sigma/T_s}\right)^2} & 0 \leq n \leq 10\sigma/T_s \\ 0 & elsewhere \end{cases} \tag{5.1}$$

Where σ is the standard deviation. Because the Gaussian function is infinite, so we truncate the Gaussian function at 5σ away on both sides of the peak. The truncation is far away enough such that the filtered pulse height will not be reduced. The choice of σ follows the following formula:

$$\sigma = \frac{\sqrt{ln\,2}}{2\pi B} \tag{5.2}$$

where B is the bandwidth of the Gaussian filter. As specified in Bluetooth LE physical layer, the bandwidth-symbol time product $BT = 0.5$ (see table 2.1). Bandwidth B is then $500kHz$. As a result, parameter σ is then 2.65×10^{-7}. The shape of the impulse response and filtered CTE pulse is shown in figure 5.2.

An operation of integral forms the phase of a GFSK signal:

$$\phi(t) = \frac{h\pi}{T_b} \int_{-\infty}^{t} m_g(t)dt \tag{5.3}$$

The discrete approximation is:

$$\phi[n] = \frac{h\pi T_s}{T_b} \sum_{i=0}^{n} m_g[i] \tag{5.4}$$

This operation can be done at higher accuracy by using the $trapz$ function in Matlab. Parameter h is the modulation index, whose nominal value in Bluetooth LE is 0.5. A segment of positive signal pulse results in increasing phase, while a segment of negative signal pulse results in decreasing phase, thus positive/negative frequency deviation is formed. The final step of the GFSK generation is the phase synthesize. The transmitted baseband signal is $s[n]$.

The phase rotation in each second according to equation 5.3 is $h\pi/T_b$, thus the frequency deviation with modulation index 0.5 is $125kHz$. Thus $8MHz$ sampling rate is well efficient.

5.1.2. Wireless Channel

The wireless channel model is constructed by applying a ray tracer model [42]. The environment is an empty rectangular room whose dimension is $7m \times 12m$. The height of the room is $2.7m$. See figure 3.2. The channel includes reflections of up to $3rd$ order. The reflections include those from the ceiling and floor. The

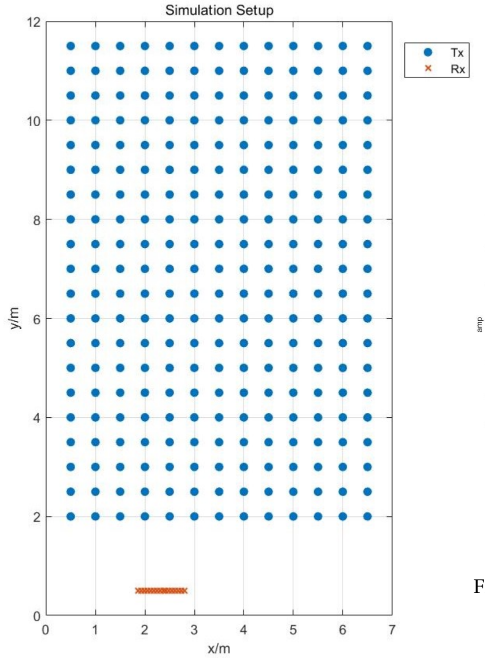

Figure 5.3: Transmitter and receiver position configuration

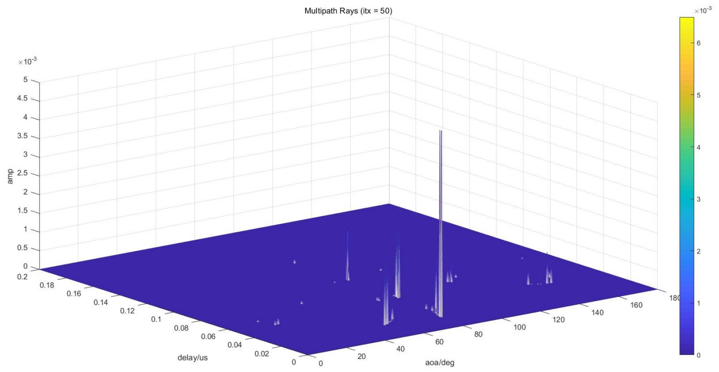

Figure 5.4: Multipath channel between itx 50 and irx 8.

reflections are considered specular and the diffused reflections and diffraction are not considered here. All antennas are vertically polarized half-wavelength dipoles. The power at the receiving antenna is calculated using the Friis transmission equation including polarization. The walls are modeled as dielectric interfaces, such that the reflection coefficient can be calculated according to [30].

A grid of 260 positions of transmitters is sampled over the room with a separation of $0.5m$, as shown in figure 5.3. The transmitters are equipped with vertically polarized half-wavelength dipoles. The receiving array is 16-element vertically polarized half-wavelength dipoles with half-wavelength spacing at $2.4GHz$. The 16-element array is not very interesting because of its large physical size. A subset of the big array can be used as a smaller 8-element or 4-element array. The array is put in a place that is close to a short wall but biased away from the middle point of the wall. Otherwise, the transmitters on both sides would experience symmetric multipath. The mutual coupling effect and the switch imbalance is not considered in the channel model.

Channel models are simulated between each pair between receiver and transmitter ($16 \times 260 = 4160$ channels). The simulated channel is modeled to be tapped delay model. Each channel impulse response can be expressed as:

$$h[n] = \sum_{i=0}^{d-1} \alpha_i \delta(t - \tau_i) \tag{5.5}$$

Figure 5.4 shows an example of the simulated channel. The x and y-axis show the delay and AoA respectively. The height of peaks indicates the magnitude of paths. The output signal of the channel follows the narrowband assumption in equation 3.15. The received signal is corrupted by white noise. The noise is added to each antenna independently.

5.1.3. Receiver

The structure of the receiver is shown in figure 5.5. The sampling rate in the receiver is $8MHz$ up to the LPF. After that, the signal is decimated such that only one sample is taken from every microsecond during guard and reference period, and from every sample slot in the middle of sampling window. In the front is an antenna array that outputs a vector of the received signal at a time instant. Then the signal is processed by a switch which selects an entry of the array output at a time according to the switching pattern. The switch here is assumed to be perfect in a sense that the switching is done immediately without settling. The effect of

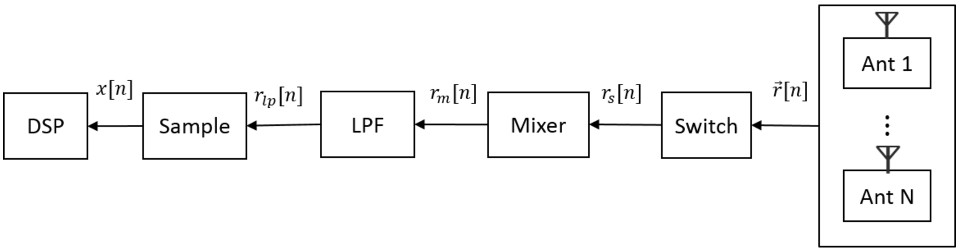

Figure 5.5: Bluetooth LE Direction Finding Receiver Model

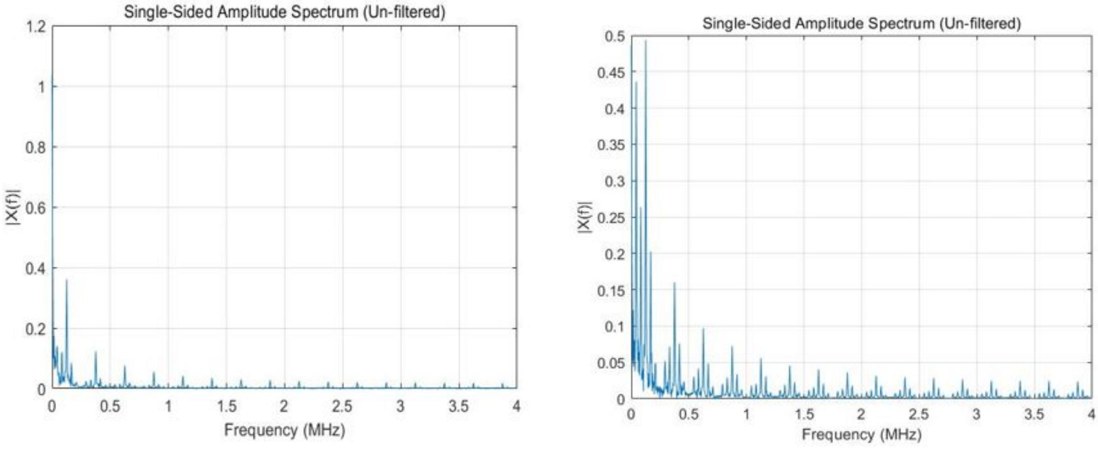

(a) AoA 80° (b) AoA 20°

Figure 5.6: Spectrum of $r_s[n]$ with a single signal impinging at different directions. Antenna array is half-wavelength ULA.

settling will be included in the low pass filtering later. After the switch, there is a mixer that mixes down the signal frequency to baseband from frequency deviation $125kHz$.

The low pass filtering (LPF) is a digital filter simulating the settling time of the analog filters in the front end, the settling time of switch and the digital filter after sampling in a real receiver. The LPF is necessary because the switching of antenna results in sudden phase jumps in the output signal of the switch. It results in high-frequency components in the spectrum. As can be observed in figure 5.6, an AoA that is close to the antenna norm (80°) gives less high-frequency component compared to the one close to end-fire (20°). It can be easily understood since the phase difference between neighboring antennas are more substantial when the signal comes from the end-fire region.

The design of the LPF is not arbitrary. The settling time has to fulfill the requirement restricted by the sampling guard time. Recall from 2.3.4, every sampling slot has a dedicated sample window within which the sampling can be done. The periods outside the sampling window are sampling guard periods that keeps the sample from being polluted by the neighboring sample due to the filter and switch settlement. For less restricted system requirement, we used $2\mu s$ time slot only.

As shown in figure 5.7a, the guarding time before sampling window with $2\mu s$ slot is $1.125\mu s$. If the switching happens at the last moment of the previous switching slot, then the filters and the switch must settle within $2.25\mu s$. The reason why the settling time is twice as long as the guard time is that the group delay is roughly half the settling time for an FIR filter:

$$\tau_s \simeq (n-1)T_s \tag{5.6}$$

$$\tau_g = (n-1)T_s/2 \tag{5.7}$$

where n is the filter order, τ_s is settling time, while τ_g is group delay. After filtering, the whole signal is delayed by half of the settling time. In the packet detection and processing, it is synchronized with the filtered version rather than the raw version of the signal. Thus the sampling time will be aligned with the middle of settling.

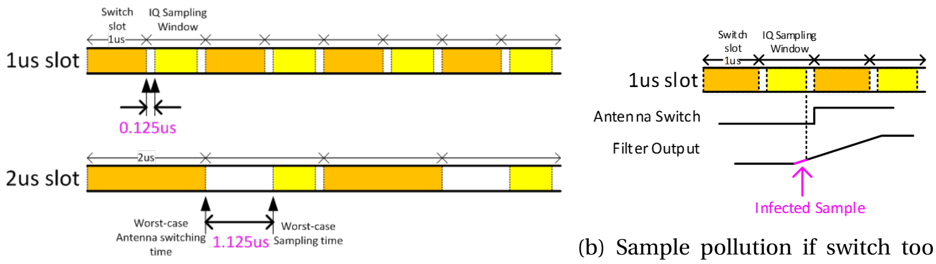

(a) Sample pollution if switch too late

(b) Sample pollution if switch too early

Figure 5.7: Sample pollution due to settlement.

Parameter	Value	Notes
Sample Rate	$8MHz$	None
Slot Duration T_{sl}	$2\mu s$	
Max Settling Time τ_{sm}	$2.25\mu s$	- Switch at the end of the switch slot
Max Order n_m	19	

Table 5.1: A summary of LPF requirement.

The same story happens when the switching happens too early, as shown in figure 5.7b. If the receiver samples at the beginning edge of the switching slot, then the filters and switch must settle within $0.25\mu s$, which is a very extreme requirement. Thus, we avoid switching too early to avoid this requirement.

Table 5.1 shows the requirements of the LPF. Then the LPF is carefully designed such that the high-frequency components can be filtered out efficiently while not exceeding the max order of 19. Figure 5.6 shows the height of the high-frequency components are relatively small compared to the baseband component. As a result, we do not need very deep stopband attenuation. The passband frequency shall be close to zero frequency, but the transition bandwidth cannot be too narrow. The transition bandwidth is an important influencer on filter order. Besides, the passband ripple shall be small to reduce distortion. The stopband ripple is less restricted as long as it provides enough attenuation. As a result, the specifications of FIR LPF is chosen, see table 5.2. The filter is designed using the Parks-McClellan (PM) filter design method. The resulting order is 17, and its response is in figure 5.8

The effect of filtering can be visualized in figure 5.9 when only one component is considered in the multipath channel. The signal after filtering is compensated by group delay such that it aligns in time with the signal before filtering. It can be observed that in the second microsecond of each sample slot, the signal is completely settled, such that the sample is interference free from the neighboring samples.

In the final part of the receiving processing chain, the DSP denotes all the processing needed for direction finding algorithm. It collects the samples in a data matrix, then carries out array calibration and LOS-Id

Parameter	Value
Passband Frequency f_p	$100kHz$
Stopband Frequency f_{st}	$300kHz$
Transition Bandwidth B_{tr}	$200kHz$
Passband Ripple r_p	$3dB$
Stopband Ripple r_s	$15dB$
Resulting Order n	17

Table 5.2: Designed PM FIR LPF specifications

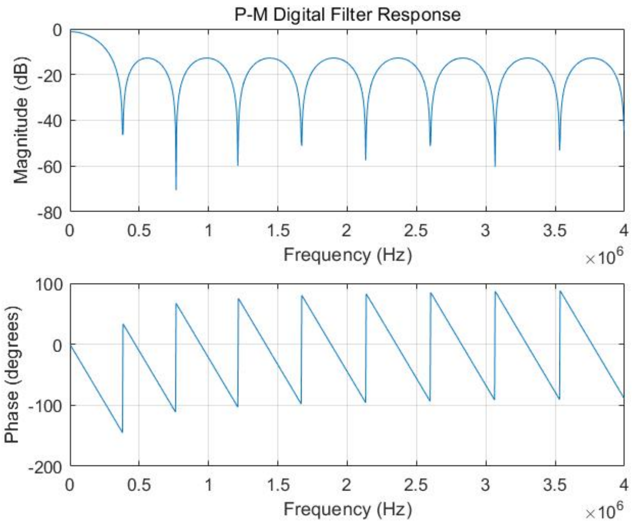

Figure 5.8: Frequency response of the designed LPF

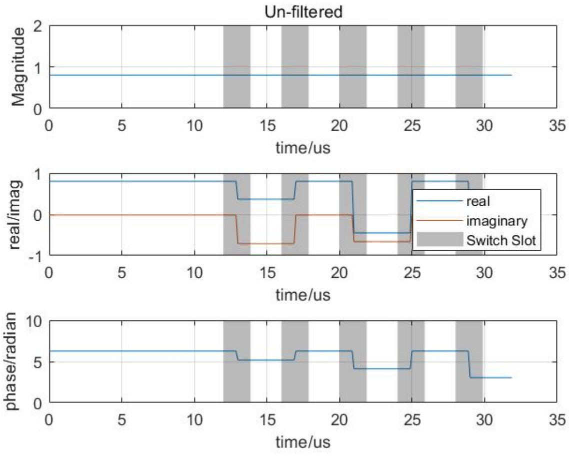

(a) Before LPF

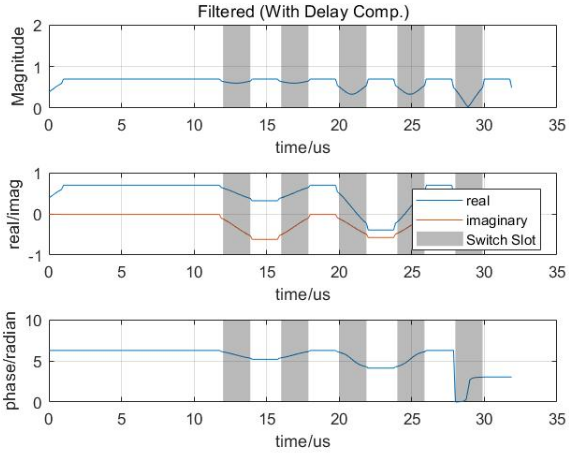

(b) After LPF

Figure 5.9: Complex signal before and after LPF when only one component is present in the channel.

algorithm.

5.1.4. Influence of Antenna Switching and LPF to Noise Color

The MUSIC algorithm relies on the spatially white property of the noise. The validity of the data model with sequential sampling also relies on the temporally white property of the noise. Because the dominant source of noise in a BLE receiver is the frond end, signals from the antennas have the same noise source. This seems contradictory to the spatial white assumption. However, the samples from different antennas are taken at different time instances so they are actually uncorrelated since the noise is temporally white.

Another concern to the noise color is that the filtering destroys the temporally white property of noise, such that the noise for antennas may be correlated with each other. The response of the LPF in section 5.1.3 is $2.125\mu s$ long, while the closest time interval between two different antenna sampling is $4\mu s$ which is well larger than the filter response time. The noise samples from the sample slots are still uncorrelated. Thus the noise color remains white.

5.2. Simulation Results

In this section, we focus on the performance evaluation for the accuracy of the algorithms proposed in the previous chapters. First, we will show the general performance of MUSIC LOS-Id algorithm without array mismodeling effects such as mutual coupling, etc. Then the performance improvement of incorporating multi-tone technique and CLEAN MUSIC LOS-Id will be shown. The effect of mutual coupling is also evaluated with the simulated MC matrix and switch matrix.

For all evaluation of the performance, simulations are carried out using the aforementioned ray tracer channel model. A thousand Monte-Carlo simulations are done for each transmitting position at a certain SNR. During the simulation, the antenna array configurations is an 8-element ULA. The performance metric we used is the root mean square error (RMSE).

5.2.1. Performance of MUSIC LOS-Id

RMSE is calculated for each transmitting position based on the estimation results of 1000 simulation runs when using MUSIC LOS-Id algorithm. No array mismodeling effects are included. The results of using an 8-element ULA when the carrier frequency is fixed to be $2.402GHz$ with SNR of $20dB$ is shown in figure 5.10. Figure 5.10a shows a heat map of RMSE obtained at each transmitting position. The color indicates the level of RMSE. The brighter the color, the better is the performance. The color of those areas in the vicinity of transmitting points is obtained by interpolation.

In the upper right corner of the heat graph, we can observe a dark area. The algorithm experiences difficulty in this area because the LOS component comes at the end-fire region (the angular section that is close to the direction formed by the antenna array, $\theta \approx 0°$ or $180°$) of the antenna array. If we examine the cosine function, the curve around 0° and 180° is flat, meaning that the cosine function is insensitive in these regions. This insensitivity reflects on the array response vector yielding the difficulty to obtain accurate estimation in the end-fire region.

Another round of simulation is shown in figure 5.11 with the same setting apart from the carrier frequency that is $2.44GHz$. Immediately we can observe the algorithm experiences difficulties in different spots as in the $2.402GHz$ case. This matches the analysis in 4.5.2. The performance of our power based algorithm suffers from destructive interference of the multipath component at the receiver. The interference varies as the center frequency varies since, with fixed time delays, the phase delays are different.

The cumulative density function (CDF) is calculated based on the proportion of transmitting positions where RMSE is smaller than a certain value over all positions. For instance, in figure (5.10b), ninety percent of transmitting positions have RMSE better than 20°.

5.2.2. Performance Improvement of Multi-Tone Technique

In 4.5.4, we proposed a multi-tone technique or packet aggregation (PA) to minimize the effect of destructive interference at the receiver. Figure 5.12a and figure 5.12b shows the heat graph of RMSE when the Monte-Carlo simulation is done with two individual frequencies - $2.4GHz$ and $2.412GHz$. We can observe different dark spots in these two cases. If we aggregate the two frequencies as proposed in 4.5.4, the result is shown in

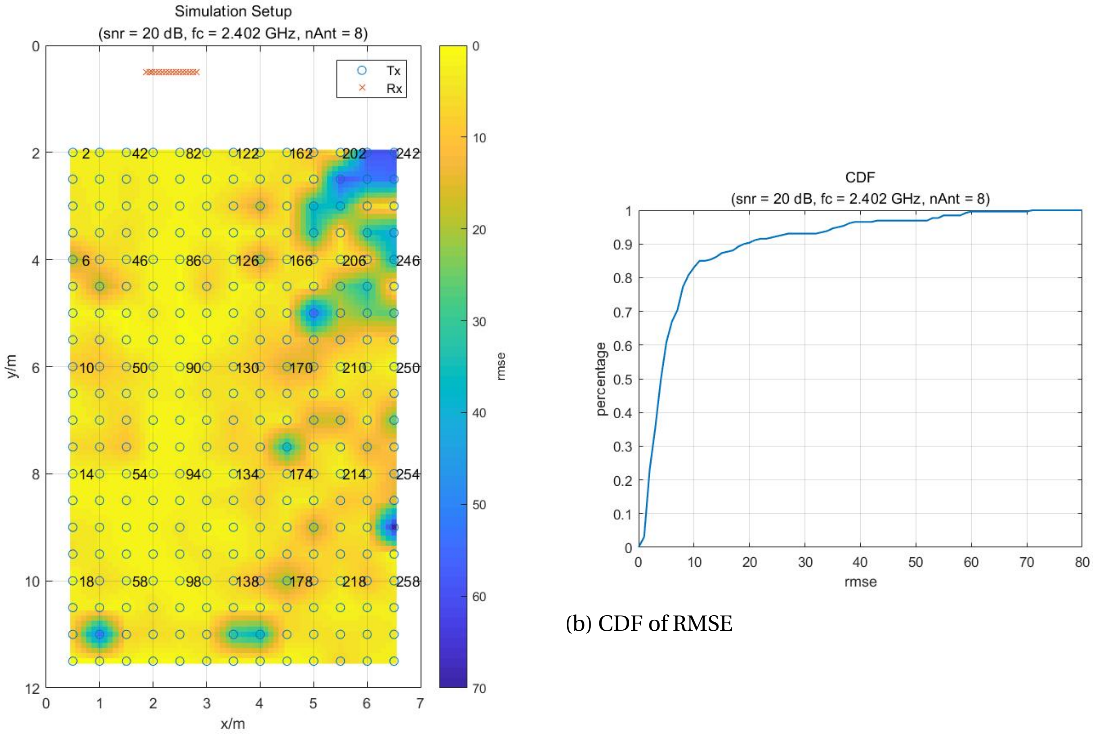

(a) Heat map of RMSE

(b) CDF of RMSE

Figure 5.10: Performance of an 8-element ULA at 2.402GHz

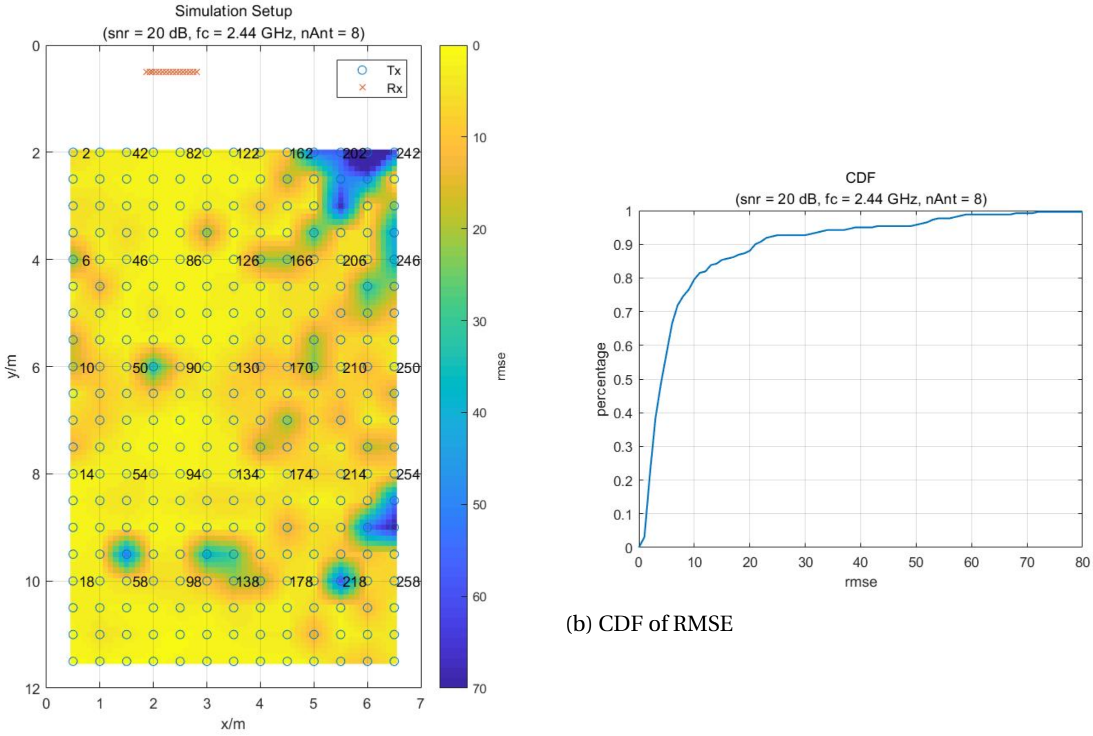

(a) Heat map of RMSE

(b) CDF of RMSE

Figure 5.11: Performance of an 8-element ULA at 2.44GHz

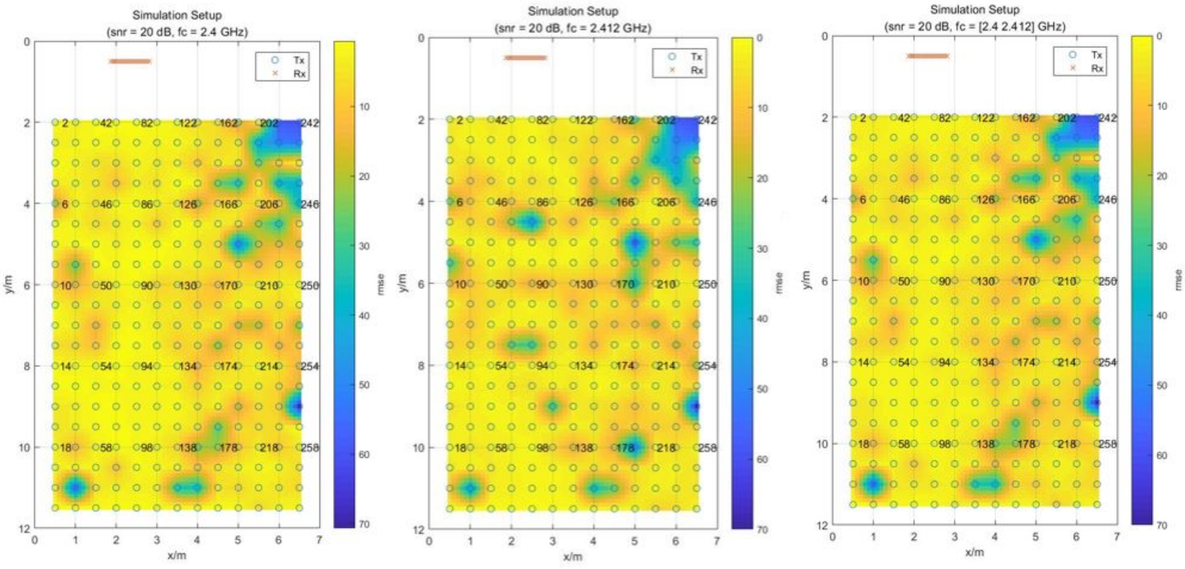

(a) Single frequency 2.4GHz (b) Single frequency 2.412GHz (c) Aggregating two frequencies

Figure 5.12: Performance of an 8-element ULA at two single frequencies and the performance of aggregating the frequencies.

figure 5.12c. An observation is that after aggregation, the performance always follows the better frequency. Poor performance only appears when the algorithm experiences poor performance on that spot at all aggregated frequencies.

To evaluate the performance more generally another set of Monte-Carlo simulations are carried out. In each run, the carrier frequency is randomly chosen from the 40 physical channels of BLE, simulating the frequency hopping. When applying multi-tone aggregation, we assume the transmitter does not change its location during the transmission of all the packets. Figure 5.13a is the heat map of RMSE when two frequencies/channels are aggregated. It's clear that the map is cleaner than those at single frequencies. Figure 5.13b shows a comparison of aggregated frequencies and single frequencies case. As it turns out, the 90th percentile and 50th percentile of the aggregated case is better than the single frequency case by around 5° and 3° respectively.

5.2.3. Effect of Mutual Coupling and Switch

Mutual coupling is incorporated in the simulator by using Antenna System Toolbox from Matlab. An array of thin wire dipoles can be constructed with an inter-element spacing of 62.5mm. In Matlab, we can create strip dipole antennas rather than cylindrical dipoles because of the complexity. The relation between the width of the strip dipole and the diameter of the equivalent cylindrical dipole is:

$$w = 2d \tag{5.8}$$

where w is the width, while r is the diameter of the equivalent dipole. The choice of dipole width is made such that thin wire approximation can be satisfied. The width is chosen to be 1/100 of dipole length. The impedance of a thin wire half-wavelength dipole is 75Ω. But since the dipole model is not infinitely thin, the impedance is not exactly 75Ω if the length is half-wavelength. As a result, the dipole is chosen to be 0.48λ where λ is the wavelength of 2.4GHz. See figure 5.15.

S parameter of the array is calculated with mutual coupling being taken into account in Matlab. The reference impedance of antennas is 75Ω since its a typical figure in transmission lines. Then the mutual impedance matrix is calculated according to equation 4.20. The mutual coupling is visualized in figure 5.16, which makes perfect sense as the coupling coefficients between two elements that are further away is much smaller. The diagonal elements are related to reflection coefficients. They are not exactly the same even though the termination conditions are all the same. The diagonal is symmetric.

The mutual coupling effect is applied by multiplying the coupling matrix with received signal vector $\vec{r}[n]$ in figure 5.5. After including MC into consideration without calibration, the simulation result is shown in fig-

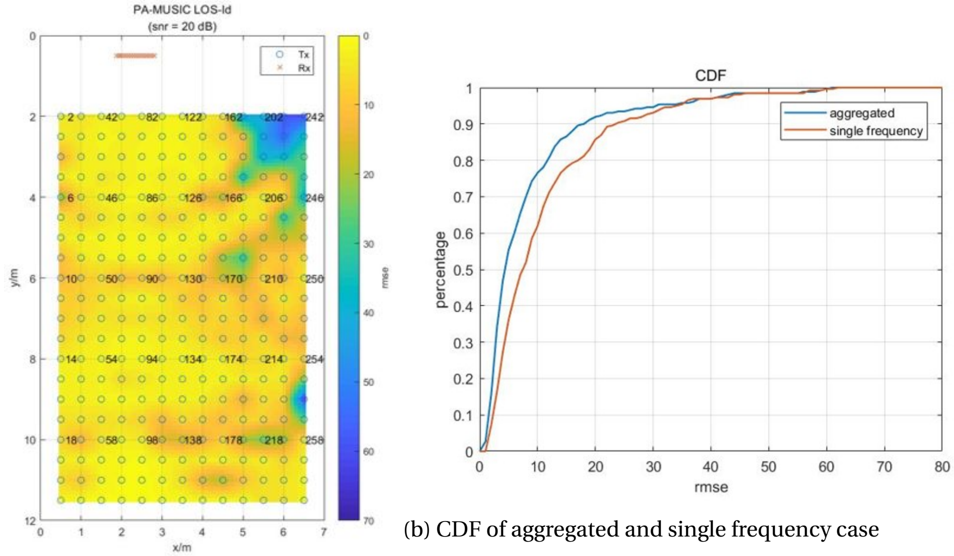

(b) CDF of aggregated and single frequency case

(a) Heat map of RMSE

Figure 5.13: Performance of an 8-element ULA at random frequencies.

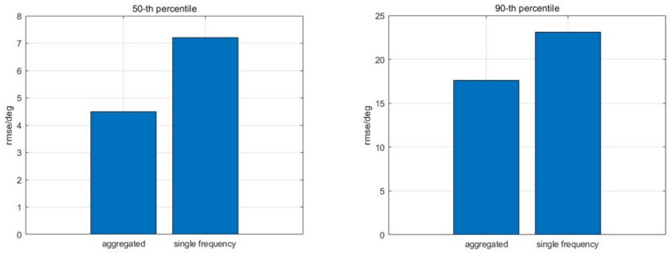

(a) 50th percentile

(b) 90th percentile

Figure 5.14: 50th and 90th percentile.

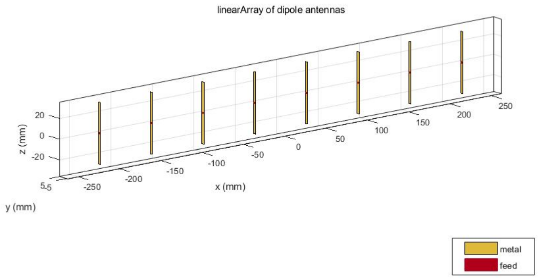

Figure 5.15: Dipole array geometry in Matlab

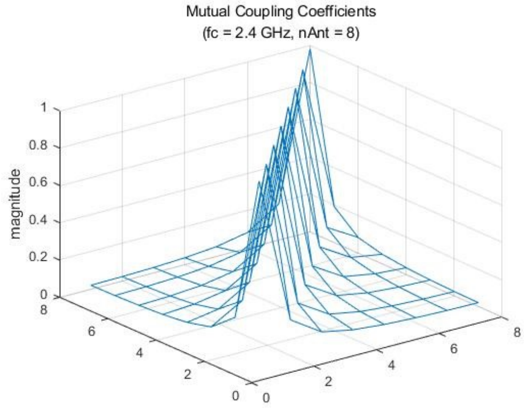

Figure 5.16: Mutual Coupling matrix

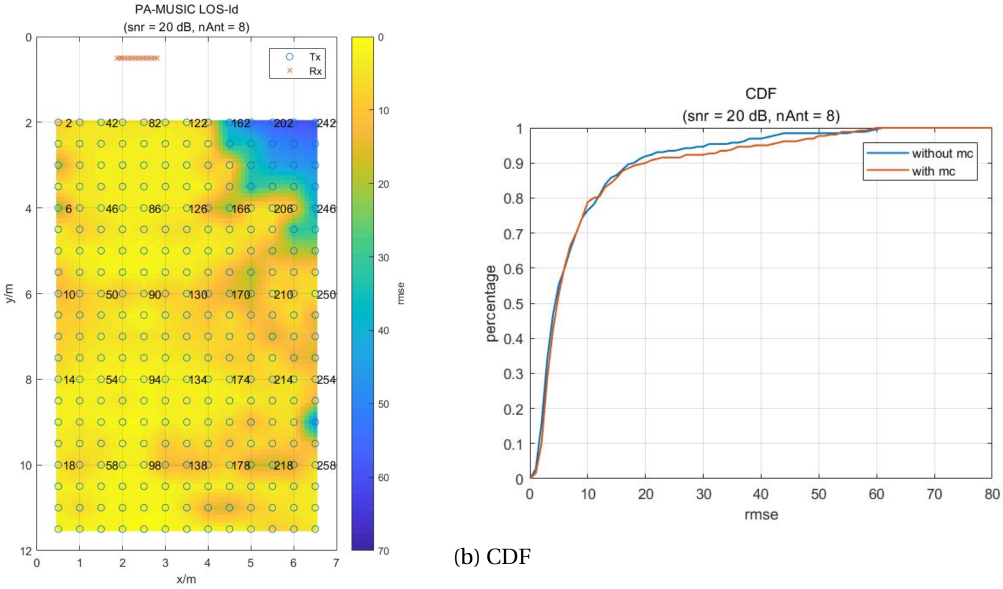

(b) CDF

(a) Heat map of RMSE

Figure 5.17: Performance of a 8-element ULA with PA when MC is present.

ure 5.17. As compared to the case without MC, the result barely shows any difference. The similar conclusion is also drawn for the effect of the switch, as shown in figure 5.18. Thus the most significant limiting factor on the performance is multipath.

5.2.4. Performance Improvement of CLEAN-MUSIC LOS-Id

We mentioned in section 4.5.3, the proposed CLEAN-MUSIC LOS-Id algorithm does have its limitation. Because of the harshness of the indoor multipath environment, coherent residuals are present after data matrix subtraction in step 3-b. Moreover, the complexity of the algorithm limits its usefulness for Bluetooth LE devices since their intention of being less costly and complex steers them away from powerful processors. In this thesis, no any further action was done for the improvement beyond the algorithm described in 4.5.3.

However, it's still worthwhile to point out the potential of this method. To set a benchmark, simulations are done for the single-frequency MUSIC LOS-Id algorithm without noise. The corresponding result is shown in figure 5.19a. For comparison, the same simulations are also done for CLEAN-MUSIC LOS-Id. Because we did not derive a technique to block out the coherent residuals, we set a set of eigenvalue thresholds. In each iteration, the eigenvalues that are below the threshold are considered to be residual. The thresholds that give the best LOS AoA estimation accuracy are selected, and the corresponding accuracy is recorded. Figure 5.19b is the outcome. Most of the dark spots where MUSIC LOS-Id has difficulties with are eliminated apart from the upper-right area, which is limited by the array beamwidth. Moreover, the $90th$ percentile is improved by about 3°, as shown in figure 5.19c.

5.3. Conclusion

In this chapter, the proposed algorithms are verified by utilizing simulation. The frameworks of the receiver and transmitter are constructed according to the physical layer and link layer of Bluetooth LE. The multipath channel is simulated by applying a ray tracer model which excludes the array mis-modeling factors, such as the mutual coupling.

Overall, in the simulated multipath environment, the proposed MUSIC LOS-Id algorithm can achieve RMSE of about 20° at 90% transmitter locations, and RMSE of about 8° at 50% transmitter locations, with an SNR of $20dB$. If no noise is present, the $90th$ and $50th$ percentiles can be 10° and 1° respectively. With multi-tone technique Packet Aggregation, the performance is improved substantially.

Besides, we simulated the mutual coupling and measured switch imbalance. Results show that these two effects are minor since the multipath effect is the dominating factor that degrades performance. Finally, the CLEAN-MUSIC LOS-Id algorithm is proven to have the potential to improve the performance even further.

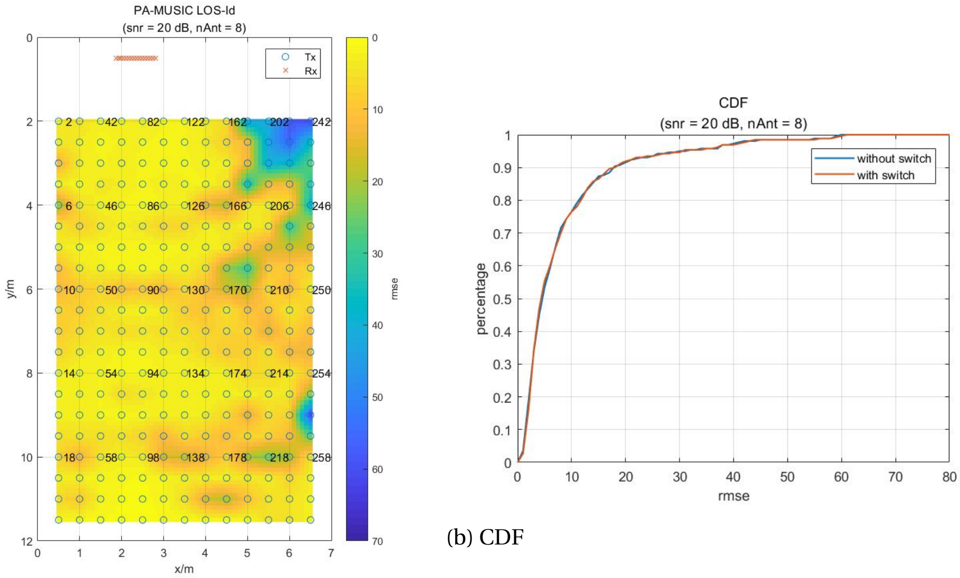

(b) CDF

(a) Heat map of RMSE

Figure 5.18: Performance of a 8-element ULA with PA when the switch is present.

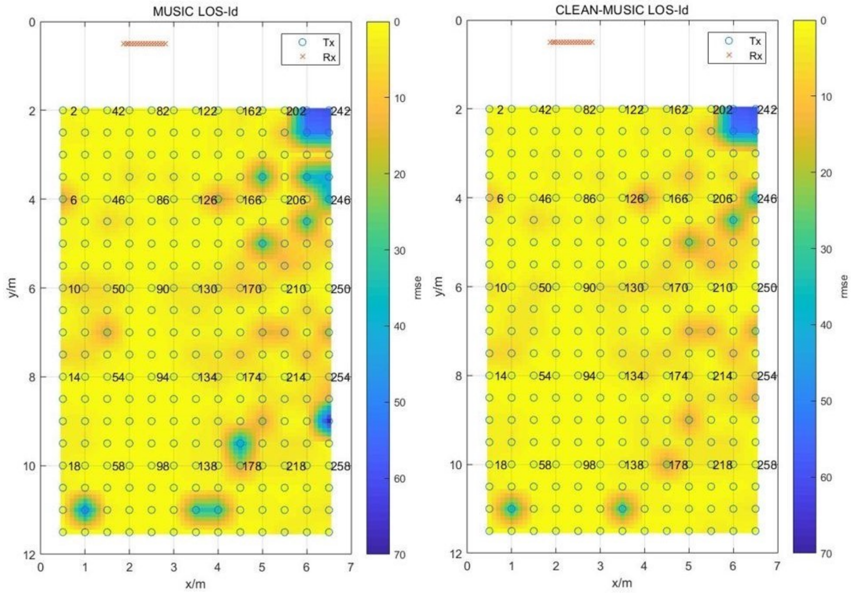

(a) Heat map of RMSE of MUSIC LOS-Id (b) Heat map of RMSE of CLEAN-MUSIC

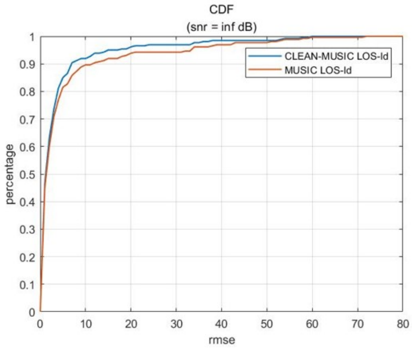

(c) CDF

Figure 5.19: Performance of a 8-element ULA with CLEAN-MUSIC LOS-Id.

6

Real Channel Measurement

In the previous chapter, the algorithms and theories are verified using simulated channel models which excludes the effects of mutual coupling and path imbalance. In this chapter, measurement campaigns are carried out to obtain a real channel model in an empty meeting room to obtain the insight into the performance of a BLE direction finding system. The evaluation of algorithm performance is done as well.

The measurements are conducted using a four-port Vector Network Analyzer (VNA) N5242A from Agilent Technology in $2.4GHz$ ISM band. Three measurement campaigns are carried out. The first and second uses ULAs consisting of 4 and 8 elements respectively. The third one uses a 2 × 4 uniform rectangular array (URA) to provide beamforming in elevation plane to eliminate reflections from the ceiling and floor. Different transmitting antenna orientations are used to provide freedom or potential accuracy improvement.

Like chapter 5, all simulation results are based on Return-to-First switching pattern, unless explicitly specified.

6.1. Measurement Description

6.1.1. Environment Setup

The environment where the measurement is conducted in a meeting room P.054 in IMEC-Holst Centre, Eindhoven. The room is rectangular without furniture, and two of its walls are made of wood while the others are made of glass. A map of the room is depicted in figure 6.1.

The positions where the transmitter is placed are indicated by a carpet where a shape of number eight is drawn. There are 109 points separated evenly by $25cm$ on edges of the eight-shape. The whole eight-shape is formed by 7 segments that are named by the endpoints (for instance, 'AB'). The points on edge are referred by appending an index number to the corresponding segment's name. The third point on segment AB, for instance, is referred to as 'AB03'.

The transmitting antenna consists of two elements of monopole, forming an angle of 90 degrees to provide the diversity of polarization. The receiver array is placed in the corner of the room. Four rounds of measurement will be conducted. In each round, a different corner is chosen. The array baseline is 45° to the nearby walls. The middle point of the array will be placed $0.5m$ away from two neighboring walls.

The coordinate system is also shown in 5.3. The origin point is the upper left corner. The x-axis starts from the origin point and points to the right along the short wall. The y-axis starts from the origin point and points to the lower direction along the long wall.

6.1.2. VNA Setting

The VNA output power shall be chosen such that the noise floor is avoided on the reception side. The link budget has to be calculated then according to the free space path loss formula [1]:

$$P_r = P_t + G_{at} + G_{ar} - 20log\frac{4\pi d}{\lambda}(dB) \tag{6.1}$$

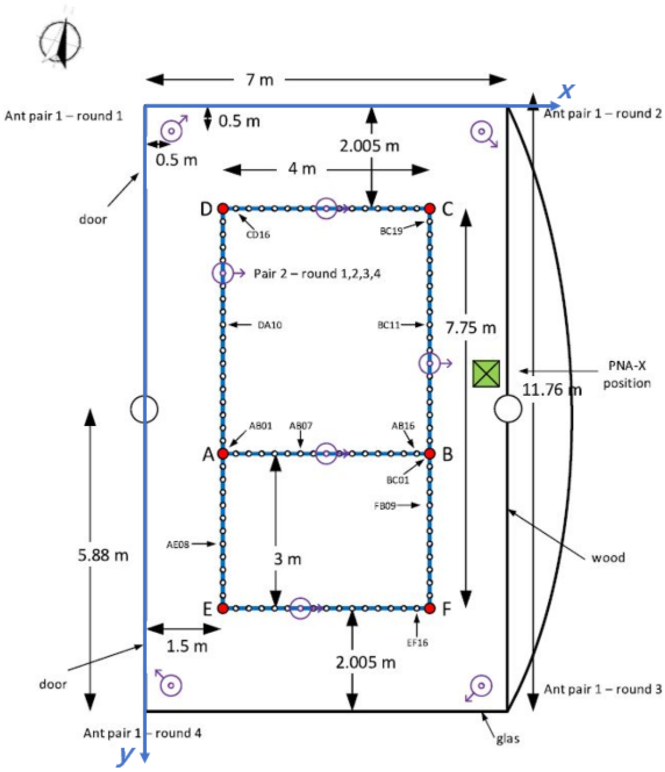

Figure 6.1: Top view of measured room

Parameter	Value
Frequency range	$2.2-2.6095GHz$
Frequency points	4096
Frequency step	$100kHz$
VNA output power	$10dBm$

Figure 6.2: VNA Setting

where P_t is transmitted power, P_r is received power, G_{at} is the gain of transmitting antenna, Gar is the gain of receiving antenna, d is the distance between transmitter and receiver. The maximum distance between transmitter and receiver is $11m$, the wavelength λ is chosen to be $62.5mm$, which corresponds to $2.4GHz$. The path loss is then $-66.89dB$. We assume the transmitter and receiver antenna are omnidirectional in azimuth plane(the receiver patch antenna does have a gain of $5dB$ in the direction where it faces, but for the worst case it's reasonable to consider the gain to be $0dB$), and they are placed on the same height, the transmitter and receiver gains are approximate $0dB$. The reference sensitivity of a BLE device receiver is $-70dBm$, such that the transmission power has to be at least $-3.1dBm$. Then the choice of $10dBm$ output power in table 6.2 suffices.

The measurement frequency range is chosen to be $2.2-2.6095GHz$ spanning a $409.6MHz$ frequency range. It is sampled by 4096 points with $100kHz$ frequency step. This corresponds to a maximum resolvable delay of $10\mu s$ (or $3km$ in the distance), and a delay resolution of $2.44ns$ (or $75cm$ of spatial resolution).

6.1.3. Antenna Configuration

Receiving Antenna Array

The antenna elements of the receiving antenna array are dual-band circular polarized patch antenna WDMP2458A from Taoglas. It can operate on both $2400-2500MHz$ band and $5150-5850MHz$ band with 50Ω impedance. The antenna is directional, as can be seen in figure 6.3

Since there will be three campaigns involving similar array structures, a small base array module is built first, as depicted in figure 6.4. The array consists of 4 patch antennas with an adjustable inter-element spacing between 56.25mm and 68.75mm, corresponding to 0.45 to 0.55 times the wavelength of 2.4GHz. The feeding points of the array are connected to an RF Switch via SMA cables, with the COM port connected to VNA. Throughout the measurement, the inter-element spacing is fixed to be $62.5mm$.

The 8-element ULA is constructed by placing two array module side-by-side, see figure 6.5a. At this time, the inter-element spacing is nonadjustable since the plastic housing limits the spacing between two array modules. The allowable inter-element spacing, in this case, is 62.5mm, corresponding to half-wavelength of 2.4 GHz.

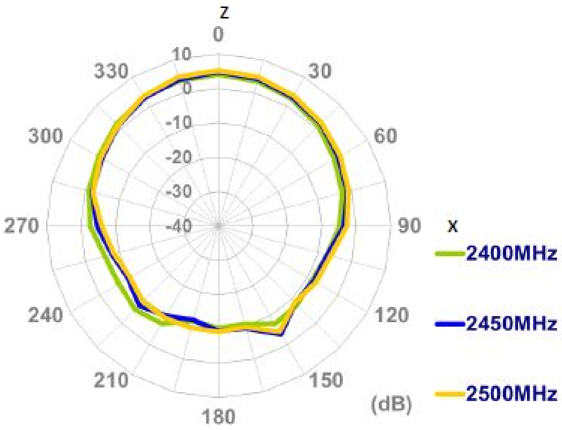

Figure 6.3: Radiation pattern of WDMP2458A patch antenna.[37]

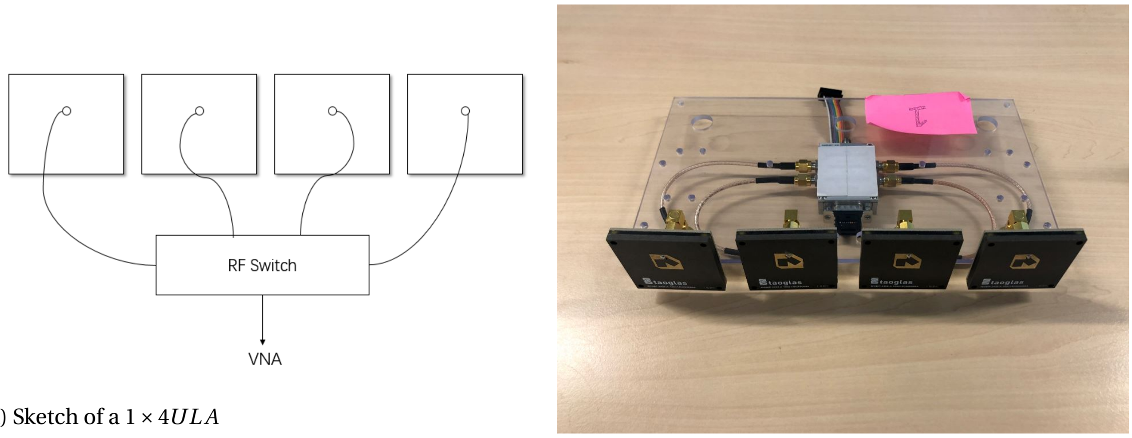

(a) Sketch of a 1 × $4ULA$

(b) Photo of a 1 × $4ULA$

Figure 6.4: 1 × 4 ULA

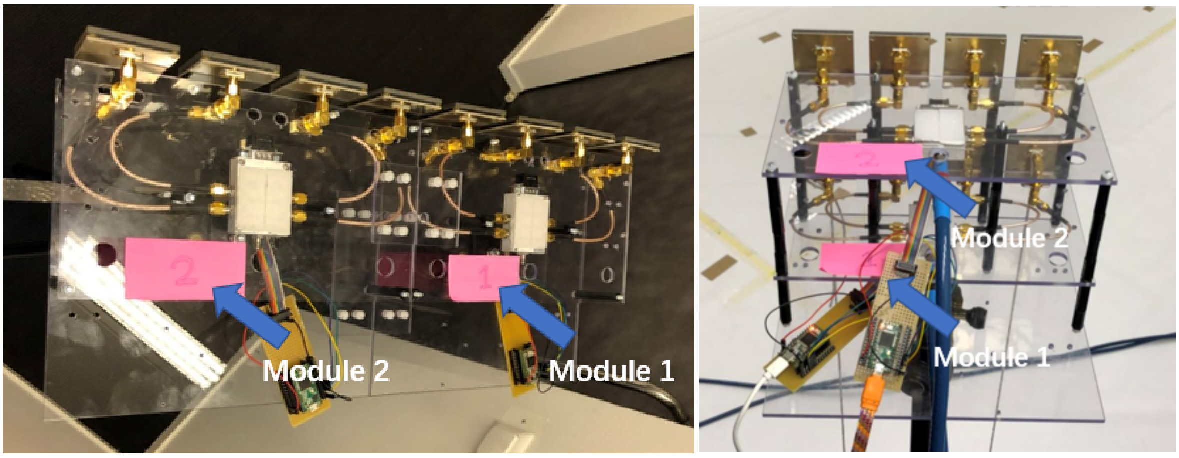

(a) 1 × 8 ULA

(b) 2 × 4 ULA

Figure 6.5: 1 × 8 and 2 × 4 ULAs

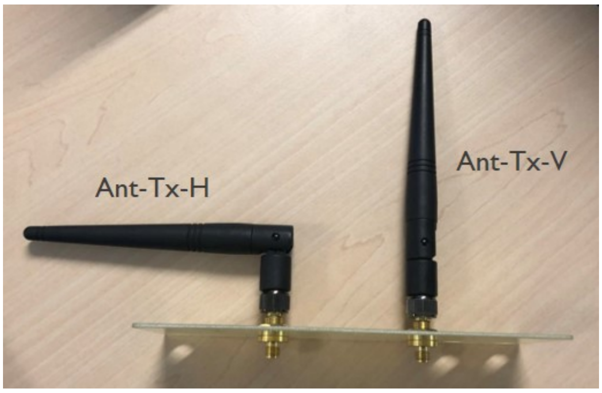

Figure 6.6: Transmitting antnna pair

VNA Port	Antenna (Array)	Note
1	Ant-Tx-V	None
2	Ant-Tx-H	
3	Rx Module 1	
4	Rx Module 2	VNA port 4 is not connected in campaign 1

Table 6.1: VNA port connection list

The 2×4 rectangular array is constructed by stacking an array module on top of the other one, see figure 6.5b. In this case, the element spacing within a module is fully adjustable between 56.25mm and 68.75mm. The inter-module spacing is also fully adjustable by tuning the length of the spacer. In the measurement, the inter-module spacing is $10cm$ to form a narrow beam on the elevation plane. Note that we do not actively conduct beamforming in the elevation plane. We assume the transmitter is on the same level as the receiver. Thus we just combine the received signals from two modules to let the beam point horizontally. The intention of using this geometry is experimental. We would like to try to block the multipath components that are reflections from floor and ceiling to reduce the number of multipath rays.

Two base modules are constructed and used throughout the measurement. The combination of these two base modules in the latter two campaigns are shown in figure 6.5. Due to the usage of 4-port RF switch, only one connection to VNA is necessary for each 1×4 base module. Module 1 and module 2 are connected to VNA port 3 and 4.

Transmitting Antenna Pair

On the transmitting side, a pair of monopole antennas is used as the mobile site, as depicted in figure A.4. Two monopole antennas are placed at an angle of 90 degrees to create the diversity of polarization. The antennas are quarter wavelength whip antenna DS ANT-24G-HL90-1 from RF solutions.

The antennas are connected to the VNA using phase-stable and armored cables produced by Huber and Suhner. The whole receiving antenna setup is held by a tripod and is $1.36m$ off the ground. The vertical antenna is connected to VNA port 1, and the horizontal antenna is connected to VNA port 2. The VNA connection configuration is listed in table 6.1.

6.1.4. Antenna Mounting, Positioning, and Orientation

The Rx antenna array is mounted on tripods. In measurement campaign 1 and 3, one array assembly is mounted on one tripod, see figure A.1 and A.2 in the appendix. In the second campaign, the two 4-element array modules are mounted on two separate tripods, see A.3. Meanwhile, the two modules are connected by a plastic connector to ensure rigid connection and precise inter-element spacing.

The positioning of antennas is ensured by using plumb lines. A long string with a screwdriver tied on one side is attached to an antenna such that the projection point on the floor can be determined. For Rx array, the two outer-most antennas are attached by these plumb lines. In campaign 3, the lower array is attached only. The attaching point should be as close as possible to the patch antenna. A picture demonstrating the attaching point can be found in Figure 4. The line formed by the two projection points shows the orientation of the array. The middle point of the line segment is the position of the array.

The Tx antennas are mounted on a plastic plate with inter-spacing of $6cm$. The orientation of the Tx antenna pair is set such that the plane formed by the antenna pair is always parallel to the short walls. The arrows on antenna pair 2 in figure 5.3 points from the horizontally polarized antenna to the vertically polarized antenna.

6.1.5. Data Collection

The measurement consists of four rounds, in each one of which the Rx antenna array is placed against a distinct corner. In each round, the Tx antenna pair will cover the eight-shape on the map. Software in Python is developed to control the RF switch to connect to all Rx antennas consecutively. Collaboratively, Matlab software is developed to control the VNA to save the desired S parameters. The VNA records sweeping frequency range and $[S13\_DB, S13\_DEG, S14\_DB, S14\_DEG, S23\_DB, S23\_DEG, S24\_DB, S24\_DEG]$ for each frequency sweeping step in a .csv file. Additionally, in the first Tx location of each round, the reflection coefficient of each antenna is also recorded to check whether the antennas are properly functioning. The naming convention for the file is:

Cmp**id**$\_Rnd$**n**$\_Rx$**ij**$\_LocAB$**xx**$\_Date\_$**dd_mm_yyyy**$\_Time\_$**hh_mm_ss**$.csv$

With id being the index of campaign, n being round number, ij being the activated receiving antenna numbers, AB being the eight-shape edge indicator, x being the position index of the edge, dd/mm/yyyy being the date, hh/mm/ss being the time in hours/minutes/seconds when the saving was done.

VNA recording happens 1 second after the switching command is issued for switching to be completed. The same measurement is carried out again in each Tx position after finishing a complete round of switching among the whole Rx array. This enables us to verify that the channel is still coherent within the measurement period since the assumption of a stationary channel is vital in Bluetooth direction finding.

6.1.6. Additional S Parameter Measurement for Mutual Coupling

A series of complement measurements are carried out to obtain the mutual coupling matrix by S parameter method as specified in section 4.2.1. The measurement is a complement to the first measurement campaign, where a 4-element ULA is used. In this case, the S parameter in the transmission mode of the array can be easily measured using four ports of VNA.

The measurement is carried out after each round of multipath measurement. The array is placed where it was. The patch antennas are connected directly to VNA after detaching the SMA cables. The settings on the array housing (position of RF switch and Teensey) shall remain as similar as they were when the multipath measurement was done, to ensure the scattering effect of the background is kept unchanged. Then record the S parameters of all port combinations.

6.2. Validation of Measurements

Before incorporating the measured channel into the simulator, the validity of the measurement shall be checked first. The validity check is three-fold: channel reciprocity check, channel stationarity check, and power delay profile (PDP) check.

6.2.1. Channel Reciprocity Check

If the measurement is done correctly, the wireless channel shall be reciprocal. This means the forward and reverse channel response between two antennas at fixed locations shall be the same. This is verified by comparing the S_{ij} and S_{ji}. Figure 6.7, for instance, depicts the magnitude and phase response of the channel between an element in the antenna array and vertically polarized whip antenna. The overlapping between the forward and reverse response proves the reciprocity.

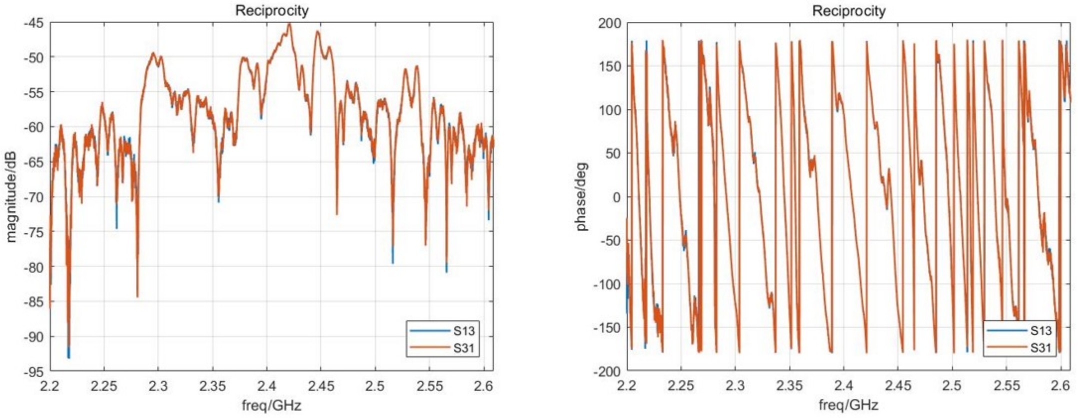

(a) Forward and reverse channel magnitude response (b) Forward and reverse channel phase response

Figure 6.7: Channel reciprocity check.

6.2.2. Channel Stationarity Check

Due to the single receiver nature of Bluetooth LE, antennas cannot be sampled simultaneously. The sequential sampling makes the samples mis-align in time. That's why we need to assume the channel is stationary throughout the CTE reception. To prove the validity of this assumption in the indoor environment, we calculate the correlation coefficients between channels that are measured during two measurements. The correlation coefficients as a function of transmission position trajectory in the first round of the first campaign is plotted in figure 6.8. The channels used in the plots are formed between the vertical whip antenna and the respective receiving antennas. The time interval between two measurements, in this case, is about $25s$. The plots show that the correlation coefficients are well above 90%, such that we can safely use the channel stationarity assumption.

6.2.3. Power Delay Profile Check

It's valuable to analyze the power delay profile (PDP) to verify the accuracy of the channel measurement since our simulator operates on time-domain channel models. The S parameter measurements can compose the frequency domain channel response:

$$H(f) = 10^{Sij\_DB/20} e^{j\pi Sij\_DEG/180}, 2.2GHz \le f \le 2.6095GHz \tag{6.2}$$

Where S_ij_DB and S_ij_DEG are magnitude in dB and phase angle in degree of S parameters between transmitting antenna j and receiving antenna i. The frequency domain response is converted to the time domain using IFFT. Because the measurement is carried out on a limited frequency range, equivalently, the frequency domain response is obtained by applying a rectangular window, which in the time domain corresponds to a sinc function. The sidelobes of the sinc function cause time leakage thus decrease the accuracy of time domain response. Therefore, to reduce the time leakage, we apply a Hann window over the measurement bandwidth at the cost of reduced $3dB$ bandwidth. The bandwidth penalty is the reason why we choose a much wider measurement bandwidth than the BLE band. Because we process in baseband in the simulator, the channel response $h(t)$ shall also be in baseband. Moving the measured channel frequency response to baseband, the equivalent baseband channel information in the time domain is then:

$$h_0(t) = \mathscr{F}^{-1}\Big(H(f+f_0)hann(f)\Big), for\ 0 \le f \le 409.5MHz \tag{6.3}$$

where f_0 is the starting point of the measurement frequency range, which is $2.2GHz$. For a signal carried by frequency f_c, the equivalent baseband channel impulse response is:

$$h(t) = h_0(t)e^{-j2\pi(f_c-f_0)t} \tag{6.4}$$

The PDP is calculated by multiplying the channel impulse response $h(t)$ by its complex conjugate. Then, PDP is analyzed along a transmitter position trajectory, which allows us to view the relationship between

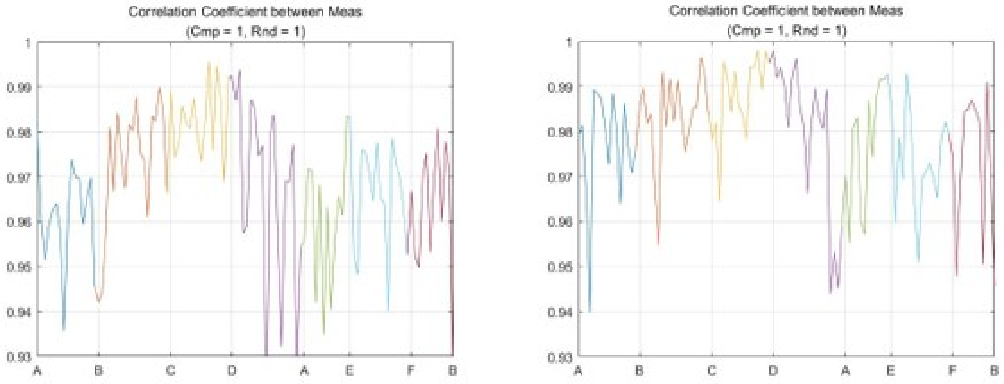

(a) irx=1

(b) irx=2

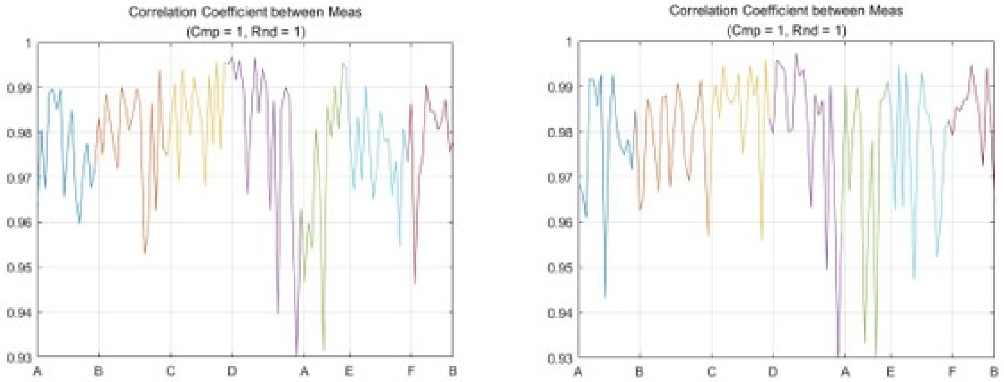

(c) irx=3

(d) irx=4

Figure 6.8: Channel correlation coefficients as a function of transmission position.

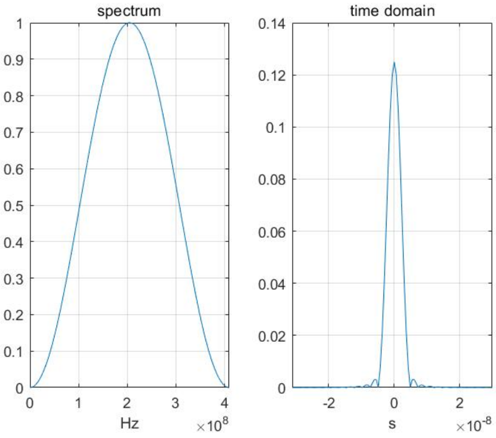

Figure 6.9: Hann window in frequency domain and its equivalence in time domain.

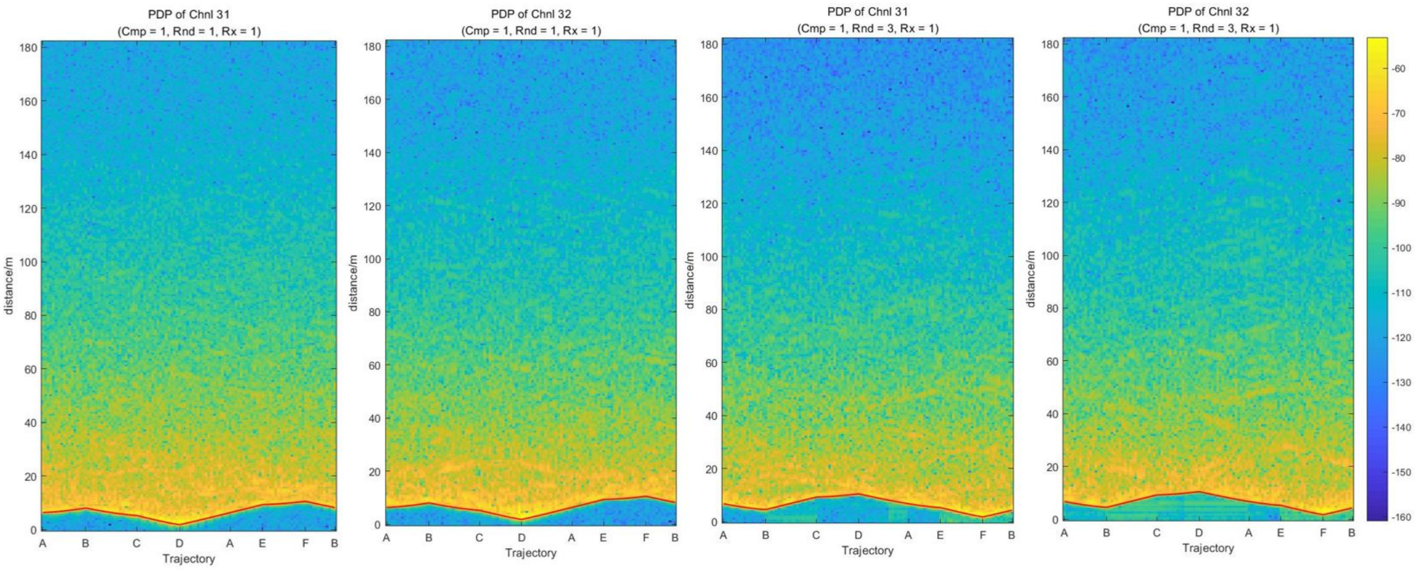

Figure 6.10: Power delay profile as a function of space in trajectory 'A-B-C-D-A-E-F-B' in the first campaign.

power and the expected time of arrival of the LOS component. A trajectory can be formed by concatenating segments. In this case, we chose the trajectory 'A-B-C-D-A-E-F-B' which is the concatenation of segments 'AB', 'BC', 'CD', 'DA', 'AE', 'EF', and 'FB', see figure 6.10. The PDP as a function of distance (derived from delay) is plotted along the columns. Each column corresponds to a transmitter location on the x-axis. The red lines represent the expected traveling distance of the LOS component calculated with the coordinates of antenna 1 in receiver array and transmitter antennas. The front edge of PDP where significant component emerges shall correspond to LOS.

Figure 6.10 shows the PDP between receiver antenna 1 and transmitter antennas in round 1 and 3 of campaign 1. The power in dB is mapped to the color bar shown on the right side. The brighter the color, the stronger the power is. The expected distance well matches the first arrivals of PDP, and thus validates the measurements.

6.3. Simulation Results after Incorporating Measured Channel

With the measured channel, we substitute the ray tracer channel model in the simulator. A series of experiments are done to evaluate the proposed algorithms in a realistic scenario. Note that in all experiments, the second channel measurement for each transmitter location is used. This is because we want to ensure the stationarity throughout the channel measurement since before the first measurements, I have to get back to the laptop from the transmitter, which may cause movements at the beginning of the first measurements. Even though in the actual scenarios, during the direction finding operation the channel will change, the time interval between antenna switching is only at a level of microseconds, while in the measurement such a time interval is $4-5$ seconds because we need to reserve time for VNA to finish data saving. During such a time period, the channel can indeed change such that the channel stationarity assumption does not hold anymore.

6.3.1. Effect of Array Geometry

Three array geometries are considered in the measurement: 1×4 ULA, 1×8 ULA, and 2×4 URA. The difference between 1×4 and 1×8 arrays can be easily foreseen since their aperture, and the available number of subarrays are large influence factors on MUSIC performance. The 2×4 array is an experimental geometry aiming at eliminating the multipath reflections from ceiling and floor. We collect the samples received from both 1×4 arrays and directly combined them by:

$$X_{2\times4} = X_{upper} + X_{lower} \tag{6.5}$$

where $X_{2\times4}$ is the combined data matrix as an input to the LOS-Id algorithm, X_{upper} and X_{lower} are data

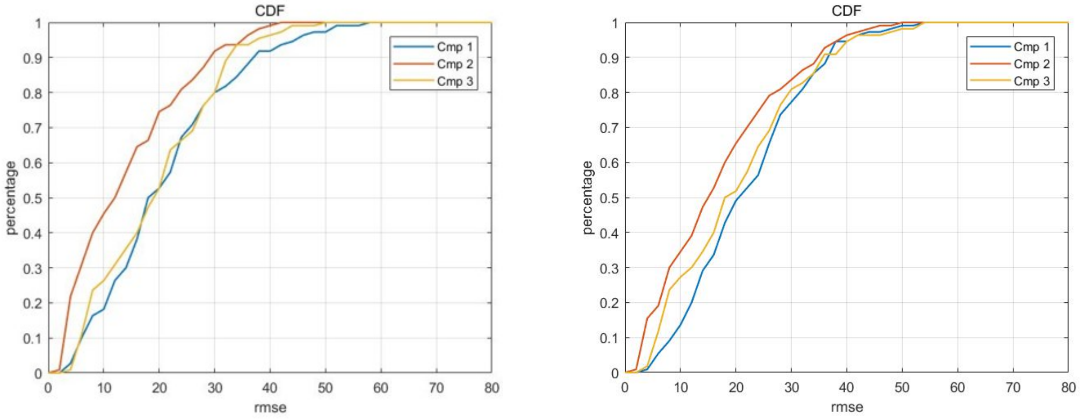

(a) Round 1, Measurement 2

(b) Round 2, Measurement 2

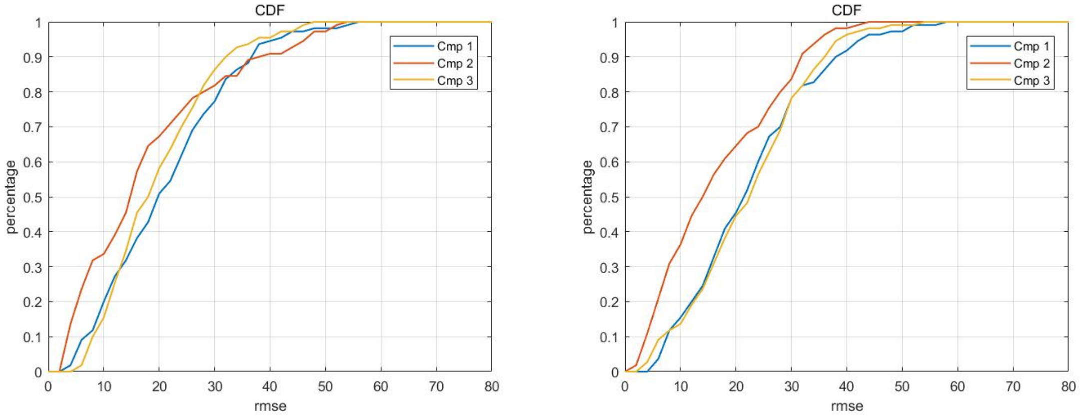

(c) Round 3, Measurement 2

(d) Round 4, Measurement 2

Figure 6.11: Comparison of array geometry when measured channel is incorporated. FBSS is applied to all array geometries. Four subarrays are used for 1 × 8 array, and 2 subarrays are used for the other two geometries.

matrices of the upper and lower 1 × 4 subarrays. We applied FBSS to all three antenna array geometries. The number of subarrays used for the 1 × 8 array is four, while we use two subarrays for the other two array geometries.

Comparisons in terms of CDF of RMSE are shown in figure 6.11. What we can conclude is that the 1 × 8 ULA leads the performance substantially, as expected. As for the 2 × 4 URA, it shows its superiority to the 1 × 4 ULA. The narrower elevation beamwidth indeed improves the performance by blocking out the ceiling and floor reflections, since these reflection components normally coincide in azimuth angle with the LOS component, and they have similar time-of-arrivals with the LOS component.

6.3.2. Effect of Antenna Polarization

During the measurement, we used both horizontally and vertically polarized transmitter monopole antennas. The receiving patch antenna is circularly polarized such that there is no difference in the receiving polarization mismatch. The influence of antenna polarization is then evaluated with the $q \times 8$ ULA. A weaker performance can be observed when horizontal polarization is used, see figure 6.12. The difference could be from the different interaction between the reflectors (walls, floor, and ceiling) and EM waves. When a vertically polarized transmitter is used, the E-field is parallel to the walls but has an angle with respect to the ceiling and floor. But for the horizontally polarized transmitter, it is the opposite: the E-field has an angle with respect to the walls but is parallel to the ceiling and floor. The in-depth analysis is not done within the scope of this thesis. But the observation made here can be a reference for the placement of polarized antennas in the real scenarios.

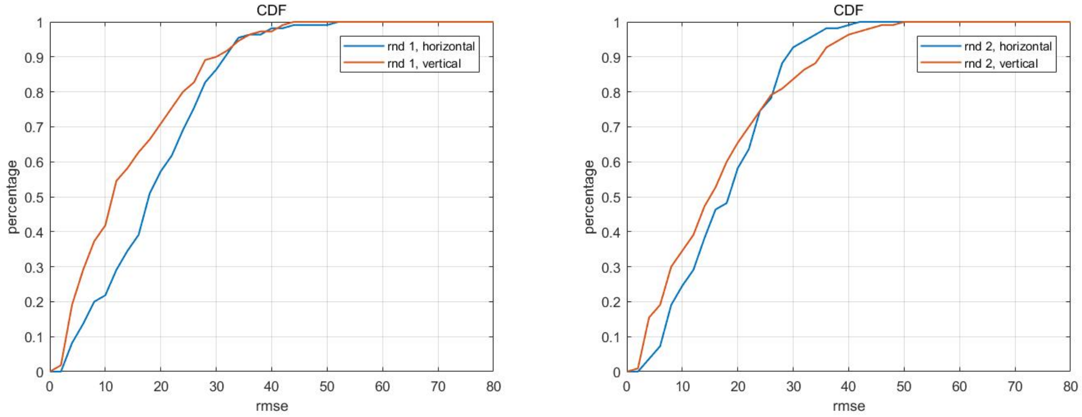

(a) Round 1, Measurement 2

(b) Round 2, Measurement 2

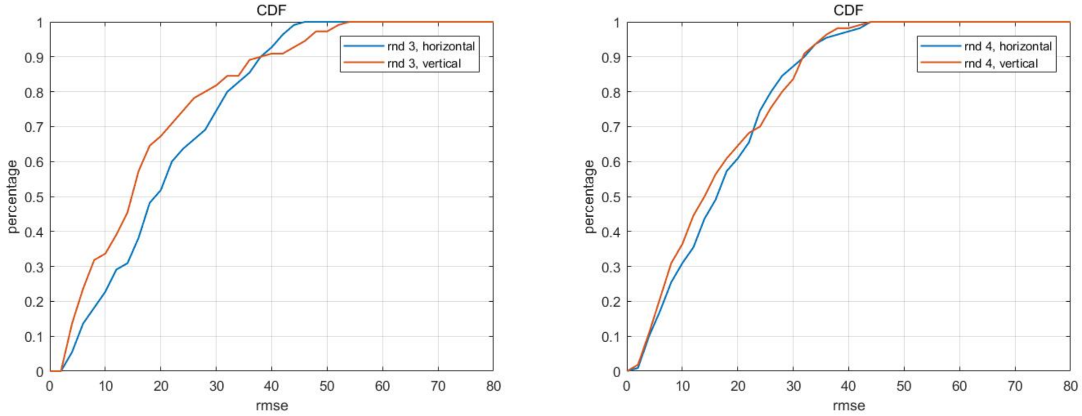

(c) Round 3, Measurement 2

(d) Round 4, Measurement 2

Figure 6.12: Performance influence from different transmitter antenna polarization. (snr = 20dB)

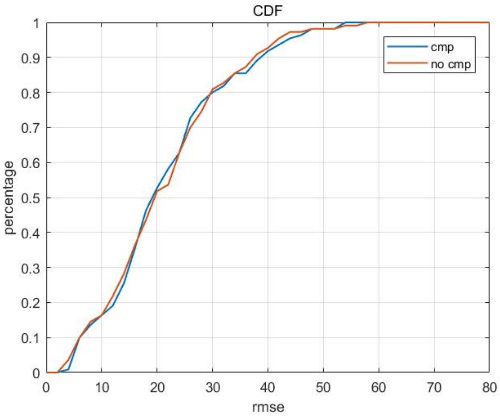

Figure 6.13: Performance of switch compensation. (Campaign 1, round 1, snr = $20dB$).

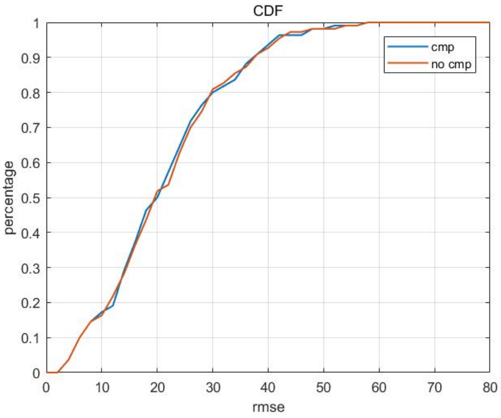

Figure 6.14: Performance of mutual coupling compensation. (Campaign 1, round 1, snr = $20dB$).

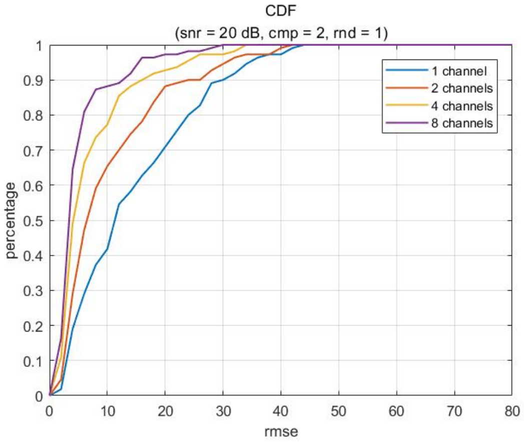

Figure 6.15: Performance improvement of packet aggregation using 1 to 8 channel(s) for a 1 × 8 ULA.

6.3.3. Effect of Mutual Coupling and Switch Compensation

In section 5.2.3, we already show and analyze the effect of mutual coupling and switch imperfection in our multipath-dominant application scenario. The conclusion is that mutual coupling and switch artifact has minimal influence compared to multipath. Nevertheless, we tested mutual coupling and switch compensation with coupling matrix obtained in 6.1.6 and 4.2.2. In this section, the 1 × 4 array geometry in the first measurement campaign is used.

Figure 6.13 shows the improvement of performance because of switch compensation. No clear improvement is observed as expected in section 5.2.3. Similarly, the minor improvement of mutual coupling compensation is shown in figure 6.14.

6.3.4. Performance Improvement of Multi-Tone Technique

We applied packet aggregation for the measured channel model using $[1,2,4,8]$ channels. The results are shown in figure 6.15. As expected, significant improvements are provided as the number of aggregated channels increases. When using 8-channel aggregation, the overall direction finding error when frequency hopping is considered is controlled to be less than 10° at about 90% of transmitter positions in the room.

Note that the aggregation of more than one channel does increase the channel occupancy time. When applying $3200Hz$ hopping rate, 8 channel aggregation would take $2.5ms$ if transmitted consecutively, which is still much less than the nominal channel coherence time as analyzed in section 4.5.4.

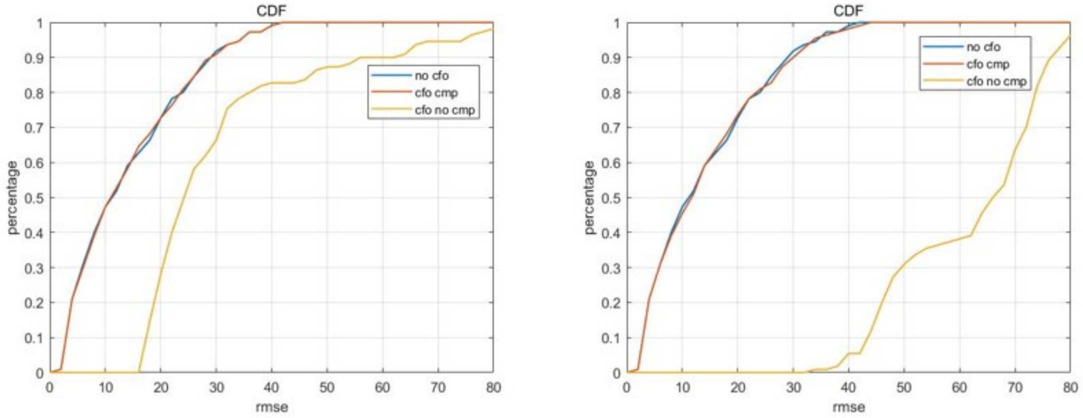

(a) CFO = $20kHz$

(b) CFO = $50kHz$

Figure 6.16: Performance influence of CFO, and the effectiveness of CFO compensation. (snr=$40dB$)

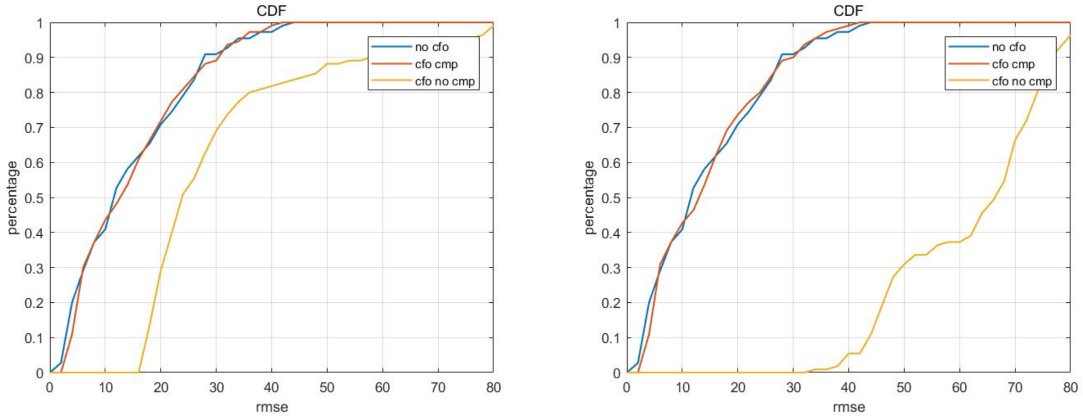

(a) CFO = $20kHz$

(b) CFO = $50kHz$

Figure 6.17: Performance influence of CFO, and the effectiveness of CFO compensation. (snr=$10dB$)

6.3.5. Effectiveness of CFO Compensation

Another influencing factor in our BLE direction finding system is CFO. CFO causes phase rotation as time goes by, which raises additional phase shift among samples from different antennas due to the switch-then-sample nature of BLE data collection. In section 4.3.1, we introduced a CFO estimation technique based on Maximum Likelihood Estimator. The packet field used for it can be either CTE reference period only or incorporating antenna samples with appropriate switching pattern. Here, we use only CTE reference period to estimate CFO, since it generally applies to all scenarios.

With CFO, we can expect dramatic performance loss when CFO is present and uncompensated. More specifically, the performance loss is expected to be more severe as CFO grows larger. It is proven by the yellow curves in figure 6.16 with $40dB$ SNR. The red curves in the figures very well coincide with the blue curves which correspond to ideal cases without CFO. Besides, the performance of CFO estimation degrades with decreasing SNR. This is proven by the bigger performance deviation in figure 6.17. Nevertheless, the CFO compensation technique proposed in 4.3.1 does provide sufficient performance to neutralize the effect of CFO.

6.4. Conclusion

With further experiments with the measured channel model, we observe that the MUSIC based LOS-Id algorithm with multi-tone technique within the Bluetooth direction finding framework offers satisfying performance in typical office indoor environments. We observed significant performance improvement when aggregate more than one frequency (sometimes is referred to as the channel or tone). When aggregating 8 channels, 90% of transmitter positions on the eight-shape grid can obtain direction finding RMSE of about $10°$. In the future, it's potential to incorporate the choice of the number of aggregation channels in the future version of Bluetooth standard to obtain a certain level of service quality.

Besides, the effect of mutual coupling and switch imperfection is further improved to be much less relevant than multipath effect and CFO because of the antenna directivity and high isolation level and path balance of modern RF switch. By choosing proper antennas and switches can avoid the complexity of calibration. Finally, it's demonstrated that CFO causes a massive performance drop. With the proposed CFO compensation technique, the effect of CFO can be compensated very well.

7

Conclusions and Future Works

7.1. Conclusions

This thesis is based on the draft of the next-generation Bluetooth standard. The standard aims to incorporate direction finding capabilities to Bluetooth LE systems as a supplement to its indoor positioning service. The goal of the project is to develop an algorithm that fits the Bluetooth LE structure to estimate the direction of the LOS component in a multipath environment. We addressed the distinction of using a switched antenna array to normal array processing. Meanwhile, we also aim to investigate the influence of practical considerations such as mutual coupling, RF switch leakage and path imbalance. Techniques for compensating the negative influences have been derived.

First, we created a new data model for the switched antenna array based on normal array processing which samples the antenna array simultaneously. The importance of CFO to the validity of switched antenna array model is addressed and its compensation method is proposed. Array mismodeling factors like MC and the RF switch effect are also incorporated into the data model. Then, we investigated the array calibration and modeling methods. We have characterized mutual coupling and RF switch effects using the S parameter method and VNA measurements respectively. Based on the new data model, a power-based LOS identification algorithm is proposed based on forward/backward spatial smoothing, MUSIC and power signature in space. Besides, a MUSIC-based CLEAN algorithm is proposed to gain better resolution within multipath clusters. This method is proved that has a potential performance advantage over the proposed LOS-Id, but meanwhile, it also has drawbacks such as computationally complex. Moreover, more works still have to be done to solve the coherent residual problem in the data subtraction step. Additionally, a multi-tone technique is proposed to improve the performance of the proposed LOS-Id algorithm.

To evaluate the effectiveness of the proposed algorithms, a BLE simulator is built in Matlab. It includes baseband GMSK modulation, ray tracer based channel models, antenna switching, receiver baseband processing effects, mutual coupling, and antenna switching including potential imperfections. To reduce the computation burden, all processing is done in baseband. Then, we use Monte-Carlo simulations to verify the proposed techniques. We conclude that in an indoor multipath environment, the heavy multipath effect is the dominant factor that limits the direction finding performance. Mutual coupling and antenna switching effects, though, are of little importance. Conclusions are also drawn that with multi-tone technique, the performance improves substantially as the number of aggregated channels increase. The simulations also demonstrate that the MUSIC based CLEAN algorithm indeed haves the potential to further improve the performance.

Finally, to verify the effectiveness of proposed algorithms in a realistic environment, a series of channel measurement campaigns are carried out in an empty meeting room. The measurement results are verified by checking the channel reciprocity, channel stationarity, and the relation between PDP and expected LOS time of arrival. The measured channel models are incorporated into the simulator then similar Monte-Carlo simulations are done. The results agree the conclusions drawn by the simulations with the ray tracer model, which proves the effectiveness in the real-life scenario. With the measured channels, after aggregating 8 channels, in 90% of transmission positions the RMSE is below 10°, and in 50% of transmission positions the RMSE is below 3°, when applying the MUSIC LOS-Id algorithm using an 8-element ULA.

7.2. Future Works

In the future, studies can be done to further improve the CLEAN algorithm. Explorations can be done to investigate the feasibility of coherent residual detection and complexity reduction. It is indeed not very interesting in our low-cost Bluetooth devices, but it could be more interesting for computationally powerful platforms such as the indoor radar.

Moreover, the array setup we built in the project used a stand-alone RF switch which cannot be switched at more than $12.5kHz$, corresponding $80\mu s$ time interval. A more specification-compliant solution can be done by designing or using the off-the-shelf RF switch IC on a PCB. This is, of course, the route that must be passed if we want the direction finding enabled BLE devices to be commercially available.

Besides, we can potentially improve the direction finding accuracy by incorporating peer device tracking. In this thesis, we proposed algorithms that take single shots of data as input, such that the successive direction finding estimations are independent. Instead, we could also take the previous estimations into account as a prior knowledge to help to rule out the outlier estimations.

Finally, works can be done to incorporate ranging and direction finding collaboratively to achieve target localization. More anchors may also be used in the future to localize a target using either direction information only, or using combined ranging and direction finding results. Data fusion algorithms can be developed to make use of multiple anchors to form more reliable location estimation.

Bibliography

[1] A. Goldsmith. *Wireless Communications*. Cambridge Uniersity Press, New York, 2005.

[2] C. Balanis. *Antenna Theory Analysis and Design*. John Wiley & Sons, New Jersey, 3rd edition, 2005.

[3] Bluetooth SIG. Traditional Profile Specifications. URL `https://www.bluetooth.com/specifications/profiles-overview`.

[4] Bluetooth Special Interest Group. *Bluetooth Core Specification Version 5.0*. Number December. 2016. URL `https://www.bluetooth.org/en-us/specification/adopted-specifications`.

[5] Q. Chen and R. Liu. On the explanation of spatial smoothing in music algorithm for coherent sources. In *International Conference on Information Science and Technology*, pages 699–702, 2011.

[6] Direction Finding Working Group. Indoor Positioning Service. 2015.

[7] J. Evans, J. Johnson, and D. Sun. Application of advanced signal processing techniques to angle of arrival estimation in atc navigation and surveillance systems. Technical report, Lincoln Laboratory, 1982.

[8] Z. Farid, R. Nordin, and M. Ismail. Recent advances in wireless indoor localization techniques and system. *Journal of Computer Networks and Communications*, 2013, 2013.

[9] E Fishler and H Messer. Multiple source direction finding with an array of m sensors using two receivers. In *Statistical Signal and Array Processing, 2000. Proceedings of the Tenth IEEE Workshop on*, pages 86–89. IEEE, 2000.

[10] B. Friedlander and A. Weiss. Direction finding in the presence of mutual coupling. *IEEE transactions on antennas and propagation*, 39(3):273–284, 1991.

[11] I. Gupta and A. Ksienski. Effect of mutual coupling on the performance of adaptive arrays. *IEEE Transactions on Antennas and Propagation*, 31(5):785–791, 1983.

[12] S. Henault and Y. Antar. Limitations of online calibration methods in antenna arrays. In *Antennas and Propagation Society International Symposium (APSURSI), 2010 IEEE*, pages 1–4. IEEE, 2010.

[13] S. Henault and Y. Antar. Unifying the theory of mutual coupling compensation in antenna arrays. *IEEE Antennas and Propagation Magazine*, 57(2):104–122, 2015.

[14] J. Högbom. Aperture synthesis with a non-regular distribution of interferometer baselines. *Astronomy and Astrophysics Supplement Series*, 15:417, 1974.

[15] H. Hui. Compensating for the mutual coupling effect in direction finding based on a new calculation method for mutual impedance. *IEEE Antennas and Wireless Propagation Letters*, 2(1):26–29, 2003.

[16] H. Hui. Decoupling methods for the mutual coupling effect in antenna arrays: A review. *Recent Patents on Engineering*, 1(2):187–193, 2007.

[17] H. Hui et al. A new definition of mutual impedance for application in dipole receiving antenna arrays. *IEEE Antennas and Wireless Propagation Letters*, 3(1):364–367, 2004.

[18] H. Zhang T. Hui. H., Low and Y. Lu. Receiving mutual impedance between two normal-mode helical antennas. *IEEE Antenna and Propagation Magazine*, 48(4):92–96, 2006.

[19] D. Kelley and W. Stutzman. Array antenna pattern modeling methods that include mutual coupling effects. *IEEE Transactions on antennas and propagation*, 41(12):1625–1632, 1993.

[20] E. Kornaros, S. Kabiri, and F. De Flaviis. A novel model for direction finding and phase center with practical considerations. *IEEE Transactions on Antennas and Propagation*, 65(10):5475–5491, 2017.

[21] G Kratschmer. Introduction into theory of direction finding. *Radiomonitoring and Radiolocation*, 2011: 2011, 2010.

[22] K. Kurokawa. Power waves and the scattering matrix. *IEEE transactions on microwave theory and techniques*, 13(2):194–202, 1965.

[23] M. Lee, V. Katkovnik, and Y. Kim. System modeling and signal processing for a switch antenna array radar. *IEEE Transactions on Signal Processing*, 52(6):1513–1523, 2004.

[24] P. Moose. A technique for orthogonal frequency division multiplexing frequency offset correction. *IEEE Transactions on communications*, 42(10):2908–2914, 1994.

[25] S. Pillai and B. Kwon. Forward/backward spatial smoothing techniques for coherent signal identification. *IEEE Transactions on Acoustics, Speech, and Signal Processing*, 37(1):8–15, 1989.

[26] PJRC. Teensy USB Development Board. URL `https://www.pjrc.com/teensy/`.

[27] J. Pollard and N. Kontakos. Bluetooth indoor channel simulation. In *Intelligent Data Acquisition and Advanced Computing Systems: Technology and Applications, 2003. Proceedings of the Second IEEE International Workshop on*, pages 39–42. IEEE, 2003.

[28] D. Pozar. The active element pattern. *IEEE Transactions on Antennas and Propagation*, 42(8):1176–1178, 1994.

[29] J. Proakis and D. Manolakis. *Digital Signal Processing*. Prentice-Hall, New Jersey, 3 edition, 2007.

[30] S. Ramo, J. Whinnery, and T. Van Duzer. *Fields and waves in communication electronics*. John Wiley & Sons, 2008.

[31] C. Roller and W. Wasylkiwskyj. Effects of mutual coupling on super-resolution df in linear arrays. In *Acoustics, Speech, and Signal Processing, 1992. ICASSP-92., 1992 IEEE International Conference on*, volume 5, pages 257–260. IEEE, 1992.

[32] A. Saleh and R. Valenzuela. A statistical model for indoor multipath propagation. *IEEE Journal on selected areas in communications*, 5(2):128–137, 1987.

[33] R. Schmidt. Multiple Emitter Location and Signal Parameter Estimation. *IEEE Transactions on Antennas and Propagation*, AP-34(3):276–280, 1986.

[34] R. Schmidt. Multilinear array manifold interpolation. *IEEE transactions on signal processing*, 40(4):857–866, 1992.

[35] T. Shan, M. Wax, and T. Kailath. On spatial smoothing for direction-of-arrival estimation of coherent signals. *IEEE Transactions on Acoustics, Speech, and Signal Processing*, 33(4):806–811, 1985.

[36] J. Sheinvald and M. Wax. Direction finding with fewer receivers via time-varying preprocessing. *IEEE Transactions on Signal Processing*, 47(1):2–9, 1999.

[37] Taoglas Antenna Solutions. *WDMP.2458.A 2.4/5.8GHz Mechanical Patch Antenna*. URL `https://www.taoglas.com/datasheets/WDMP.2458.A.pdf`.

[38] H. Steyskal and J. Herd. Mutual coupling compensation in small array antennas. *IEEE Transactions on Antennas and Propagation*, 38(12):1971–1975, 1990.

[39] J. Tabrikian and A. Faizakov. Optimal preprocessing for source localization by fewer receivers than sensors. *Proc. of the 11th Workshop on Statistical Signal and Array Processing*, pages 313–216, 2001.

[40] H. Trees. *Optimum Array Processing (Detection, Estimation, and Modulation Theory, Part IV)*. John Wiley & Sons, New York, 2002.

[41] T. Tuncer and B. Friedlander. *Classical and modern direction-of-arrival estimation*. Academic Press, 2009.

[42] R. Valenzuela. A ray tracing approach to predicting indoor wireless transmission. In *Vehicular Technology Conference, 1993., 43rd IEEE*, pages 214–218. IEEE, 1993.

[43] M. Vanderveen, C. Papadias, and A. Paulraj. Joint angle and delay estimation(jade) for multipath signals arriving at an antenna array. *IEEE Communications letters*, 1(1):12–14, 1997.

[44] A. Weiss and B. Friedlander. Manifold interpolation for diversely polarised arrays. *IEE Proceedings-Radar, Sonar and Navigation*, 141(1):19–24, 1994.

[45] R. Williams, S. Prasad, A. Mahalanabis, and L. Sibul. An improved spatial smoothing technique for bearing estimation in a multipath environment. *IEEE Transactions on Acoustics, Speech, and Signal Processing*, 36(4):425–432, 1988.

[46] M Woolley. Bluetooth 5 go faster. go further. *Bluetooth SIG*, 1(1):1–25, 2017.

[47] J.G. Worms. RF direction finding with a reduced number of receivers by sequential sampling. *Proceedings 2000 IEEE International Conference on Phased Array Systems and Technology (Cat. No.00TH8510)*, pages 165–168, 2000.

[48] A Yassin, Y Nasser, M Awad, A Al-Dubai, R Liu, C Yuen, R Raulefs, and E Aboutanios. Recent Advances in Indoor Localization: A Survey on Theoretical Approaches and Applications. *IEEE Communications Surveys & Tutorials*, 19(2):1327–1346, 2017.

[49] C. Yeh, M. Leou, and D. Ucci. Bearing estimations with mutual coupling present. *IEEE Transactions on Antennas and Propagation*, 37(10):1332–1335, 1989.

[50] Y. Yu, H. Lui, C. Niow, and H. Hui. Improved doa estimations using the receiving mutual impedances for mutual coupling compensation: An experimental study. *IEEE Transactions on wireless communications*, 10(7):2228–2233, 2011.

A

Antenna Array Assemblies

Figure A.1: 1 × 4 ULA

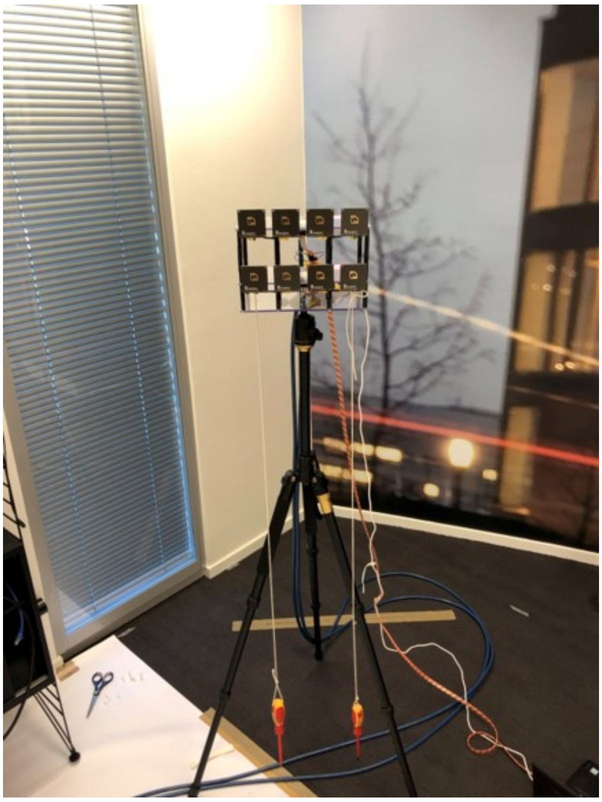

Figure A.2: 2 × 4 ULA

Figure A.3: 1 × 8 ULA

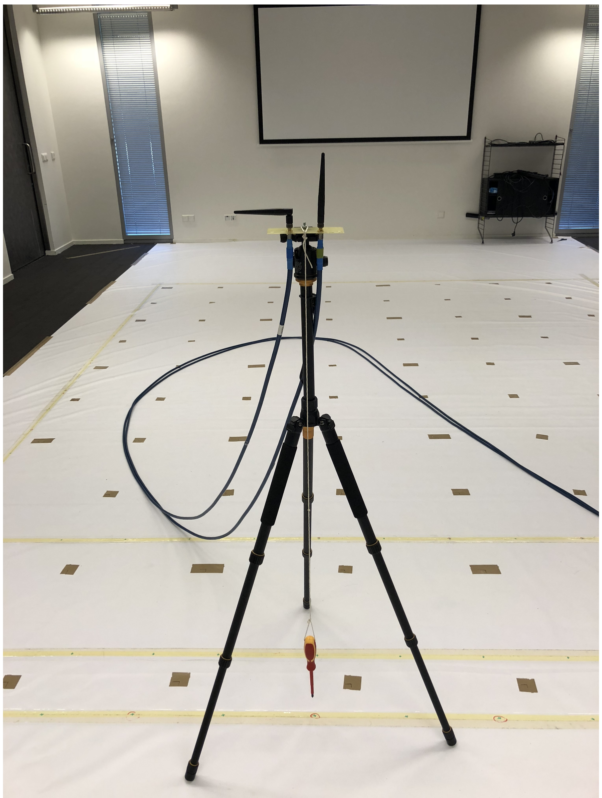

Figure A.4: Transmitting whip antenna pair